Ionic interactions around EUV generating tin plasma

Subam Rai

university of groningen
faculty of science and engineering
zernike institute for advanced materials

ARCNL
ADVANCED RESEARCH CENTER FOR NANOLITHOGRAPHY

NWO

This work originates as part of the research program of the Foundation for Fundamental Research on Matter (FOM) and falls as of April 1, 2017, under the responsibility of the Foundation for Nederlandse Wetenschappelijk Onderzoek Instituten (NWO-I), which is part of the Dutch Research Council (NWO). The work was carried out at the ZERNIKELEIF facility at the Zernike Institute for Advanced Materials of the University of Groningen as part of the research portfolio of the Advanced Research Center for Nanolithography, a public-private partnership between the University of Amsterdam, the Vrije Universiteit Amsterdam, the University of Groningen, the Netherlands Organization for Scientific Research (NWO), and the semiconductor equipment manufacturer ASML. The projects were co-financed by Holland High Tech with PPS allowance for research and development in the topsector HTSM.

Zernike Institute PhD thesis series 2023-02
ISSN: 1570-1530
Frontcover: Time-of-flight spectrum of target fragments for 120 keV Sn^{5+} colliding on H_2.
The zoom of the weak proton peaks is shown in the backcover.

Ionic interactions around EUV generating tin plasma

PhD thesis

to obtain the degree of PhD at the
University of Groningen
on the authority of the
Rector Magnificus Prof. C. Wijmenga
and in accordance with
the decision by the College of Deans.

This thesis will be defended in public on

Tuesday 28 February 2023 at 14.30 hours

by

Subam Rai

born on 29 July 1993
in Darjeeling, West Bengal, India

Supervisor
Prof. dr. ir. R.A. Hoekstra

Co-supervisor
Dr. O.O. Versolato

Assessment Committee
Prof. dr. S. Schippers
Prof. dr. R.G.E. Timmermans
Prof. dr. W.M.G. Ubachs

to aama and baba.

Contents

Chapter 1

Introduction

1.1 General introduction

In 1965, Gordon Moore, the cofounder of Intel Corporation, predicted that the number of transistors per integrated circuit (IC) in an affordable CPU would double every year [1]. A decade later, this statement was revised to doubling every two years [2], and ever since this *mantra* has been driving the semiconductor industry [3]. The ability of the industry to stay on Moore's curve via continuous miniaturization of feature sizes on ICs has been fueled by advancements in the field of photolithography.

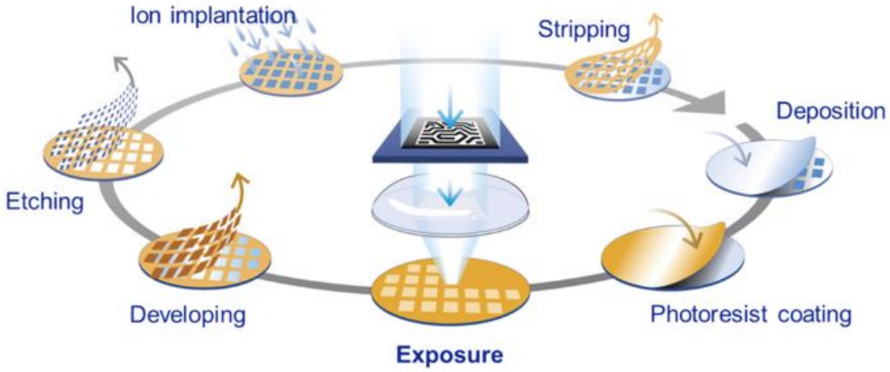

Figure 1.1: *The sequence of processes involved in the production of Integrated Circuits (IC). At the lithography step labeled exposure, the photoresist-coated silicon wafer is exposed to the light source to print the mask patterns on it. Figure reproduced from [4].*

Fig. 1.1 gives a simple illustration of the industrial process of IC production. The silicon wafer coated with photoresist material is exposed to the light source during the photolithography step labeled *exposure* in the manufacturing cycle. This way, the patterns on the mask get imprinted on the wafer. The Critical Dimension (CD) that quantifies the minimum feature size that can be printed on the photoresist in a single exposure is conventionally written as

$$\mathrm{CD} = k_1 \frac{\lambda}{\mathrm{NA}}. \tag{1.1}$$

Here k_1 is a parameter that depends on the characteristics of a specific lithography process, λ is the wavelength of the light source, and NA is the numerical aperture of the exposure tool. From Eq. 1.1, it can be noted that CD decreases with decreasing λ. Fig. 1.2 highlights the development of lithography systems manufactured by the Dutch company ASML over the past decades. Continuous miniaturization ultimately led to the transition from 193 nm light source-based lithography systems to 13.5 nm light source-based EUV lithography systems [5].

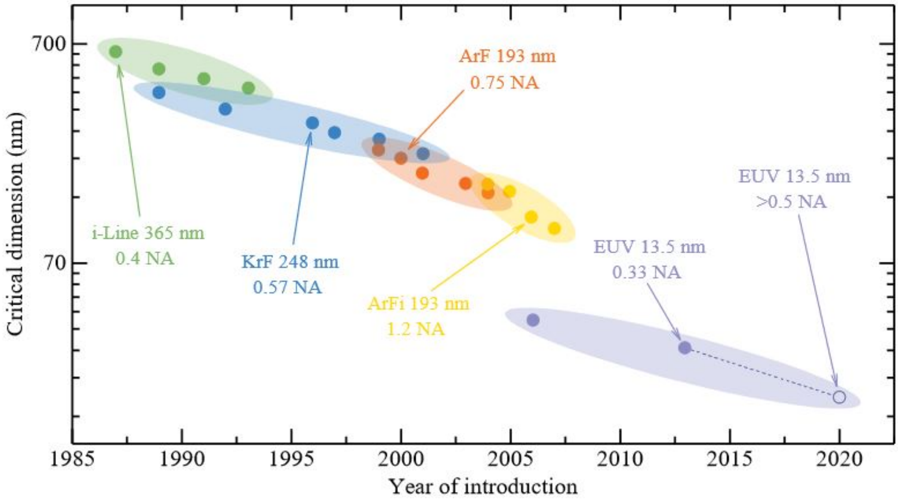

Figure 1.2: *Timeline of the evolution of lithography machines manufactured by ASML. Different generations of light sources are categorized by color, and the labels indicate the light sources used along with their respective exposure wavelengths. NA values are also mentioned for some specific cases [6, 7].*

The paradigm shift to EUV lithography demanded a complete makeover of the lithography infrastructure to meet the challenges posed by the use of EUV light. EUV light is absorbed by almost all materials. Therefore, EUV-based lithography systems need to operate in vacuum. Also, a crucial transition had to be made from lens-based refractive optics to all-reflective optics comprising Bragg reflector-based multilayer mirrors (MLM) [8] to reflect the EUV light as lens-based refractive optics cannot be used to collect and guide EUV light. The Mo/Si MLM consisting of a series of thin alternating Mo and Si layers reflect EUV light within a narrow 'in-band' 2% bandwidth around 13.5 nm with theoretically as high a reflectance as $\approx 70\%$ [9]. This motivated the search for a viable 13.5-nm light source. Highly charged Sn ions quickly emerged as the choice of source above other EUV radiators such as Xe or Li [10, 11] primarily due to the higher conversion efficiency on account of its serendipitously favorable atomic structure [11–13].

After two decades of research and development, EUV lithography has entered high-volume manufacturing [6]. In today's state-of-the-art lithography machines, EUV light is generated by irradiating mass-limited microdroplets of molten Sn with a pulsed high-power 10.6 μm CO_2 laser [14]. The EUV light from the laser-produced plasma (LPP) of Sn is collected by the collector mirror which then focuses the light towards the rest of the machinery. This process is repeated at a frequency typically around 50 kHz.

Mo/Si MLMs are the enablers of EUV lithography, and the environment inside the lithography machine must be controlled to provide optimum conditions for MLM operation such that the EUV-reflectivity of the mirrors is not compromised during operation. However, LPP debris consisting of microparticles (Sn droplet fragments, clusters, etc.) and energetic ions / atoms can damage MLMs by sputtering, implantation, or deposition [15–20], if not mitigated. This is especially true for the EUV collector mirror which is directly exposed to the LPP [21]. The industry has come up with a scheme to mitigate debris by flowing H_2 into the vacuum chamber [22]. H_2 is used as a stopping gas as it stops the debris but barely absorbs EUV light. Furthermore, Sn and H can react to form gaseous SnH_4, which can be pumped out of the system, thus helping Sn management in the machine [6]. The use of magnetic fields to guide the energetic ions away from the collector mirror has also been explored [16, 23, 24] however this approach has practical hindrances due to the requirement of strong magnetic fields.

The introduction of H_2 adds to the plethora of processes that occur inside the lithography machine [6, 25–28]. However, charge exchange and stopping are the two main processes from the point of view of ion mitigation [29, 30].

The charge exchange process between a multi-charged ion, A^{q+} colliding with a neutral atomic or molecular target, B, can be represented by the following general reaction,

$$A^{q+} + B \rightarrow A^{(q-r)+^*} + B^{(r+s)+^*} + se^-. \tag{1.2}$$

Following the collision, $r + s$ electrons are removed from the target, of which r electrons are retained by the ion, whereas s electrons are emitted into the continuum through a process such as autoionization. In cases $s = 0$ i.e. if no electrons are released to the continuum then the process is simply called electron capture. The target and/or the projectile may be left in an excited state after the collision in which case they decay to the ground state by emitting photon(s) in one or more steps.

In general, the complex collision dynamics that govern the charge exchange process (Eq. 1.2) are characterized by the following main parameters: relative ion velocities, charge and electronic structure of the ion and the electronic structure of the target along with the binding energies of the target electrons [31]. Hitherto, the reports on charge exchange studies, both experimental and theoretical, have primarily been dominated by work on low-Z ions that have a limited number of active electrons, and comparatively fewer reports exist on complex and heavier ions. However, the research interest in collisions involving Sn ions has recently grown due to the potential application of Sn for fusion plasma vapor shielding [32–34] and more importantly due to the emergence of Sn-LPP-based EUV lithography.

The Sn ions coming from Sn-LPP in EUV light sources can have energy as high as tens of keV [35–37] but due to the heavy mass, the velocities of these Sn ions ($\approx$ 0.1 a.u. or lower) are still low from an atomic collision perspective. At these lower ion velocities ($v \ll v_o$ where v and v_o represent the ion velocity and the orbital velocity of the target electron, respectively), electron capture is the dominant charge exchange process. Electron capture at lower energies, in general, is a highly resonant process and very state-specific, thus relying on the availability of states. Therefore, the cross sections for the electron capture process are either very large (several times 10^{-15} cm^2) or very small ($\leq 10^{-16}$ cm^2). Due to the large cross sections expected for single electron capture, in the presence of H_2, most of the multiply charged Sn^{q+} ions from LPP ($q \geq 3$) are expected to transit rapidly to lower charge states after undergoing charge exchange collisions with H_2. However, hardly any experimental or theoretical data exists on this significant process. Low-energy collisions between multiply charged heavy ions of Sn and lighter targets such as H_2 are challenging for theory due to the multiple active electrons involved and the two-center basis of H_2. A full quantum mechanical treatment gives the most accurate predictions but is often computationally intensive. Thus, a semi-classical approach is often used in which the motion of the nuclei is treated classically by a straight line or Coulomb trajectories [38].

In addition to charge exchange, collisions of Sn ions with H_2 lead to loss of kinetic energy of the Sn ions. This process is quantified by the so-called stopping power

$$\frac{dE}{dz} = -nS(E) = -n(S_n(E) + S_e(E)), \tag{1.3}$$

where E is the kinetic energy of the projectile Sn ion, dE is the average energy loss over a path length dz, n is the number density of the target, and $S(E)$ is the atomic scale stopping cross section. In Eq. 1.3, the common assumption is followed that the stopping cross section S has two distinct and independent contributions S_n and S_e representing the nuclear and electronic stopping cross sections respectively. Nuclear stopping power is due to the interaction of the target nuclei partly shielded by the target's electrons with the projectile ion. Electronic stopping power results from the inelastic energy loss by the projectile ion due to collisions with the target's electrons. Electronic stopping power is generally stronger at higher ion energies (for Sn ions 1 MeV or higher), while at lower ion energies, including the case of Sn ions from LPP, nuclear stopping is dominant. Detailed experimental reports about the stopping cross sections for Sn^{q+}+H_2 collisions are currently scarce in the available literature. Ion stopping in such collisions is often simulated using a popular Monte Carlo simulation package SRIM (Stopping and Range in Matter) that uses the ZBL shielding function to simulate the shielding of nuclei by electrons [39].

The usage of SRIM is ubiquitous, especially for simulating ion-solid interactions [40–47]. Similar interactions often occur inside the EUV source in nanolithography machines, where the energetic Sn ions from the LPP interact with the MLM materials. However owing to the absence of experimental benchmarks, there is scope for testing the reliability of SRIM in simulating such keV energy heavy ion-target collisions.

1.2 Thesis outline

The work presented in this thesis aims to advance the understanding of collisions of energetic ions with surfaces and gas targets with Sn being the prime ion of interest.

The backscattering of energetic Sn ions from Mo and Ru surfaces is investigated and the results of this study is discussed in chapter 2. Mo is one of the elements making up the repeating layers in Mo/Si MLMs used in EUV lithography and Ru, another transition metal, is often used as protective capping layers to EUV-reflecting MLMs [48]. The experimental findings are compared with the predictions of SRIM. This chapter aims to evaluate the reliability of SRIM simulations in keV-energy heavy-ion-heavy-target collisions.

The ion scattering results from Mo and Ru show discrepancies with the results of SRIM simulations. The remarkable difference observed is the absence of a single scattering peak (SCP) in the experiments, while, as predicted by SRIM, an intense

SCP is expected. To investigate this remarkable observation further, a detour is taken to study the Kr-Cu system because this system has the same projectile-target mass ratio as Sn-Mo/Ru and is therefore expected to have similar collision kinematics.

In the following chapters, the focus is shifted from ion-surface interactions to ion-gas collisions. A crossed-beam experimental setup CHEOPS is built to study collisions of charge, energy and isotope-selected Sn ions with gas targets, primarily H_2. The setup is described in Chapter 4.

A quantitative understanding of charge exchange in collisions of Sn ions with H_2 is not only interesting from a scientific point of view but is also desirable for accurate predictive modeling of ion interactions inside the EUV source environment. In Chapter 5, we report the experimentally measured single electron capture cross sections in collisions of Sn^{3+} ions with H_2 and D_2 in the energy range of 1 to 100 keV. The novel experimental results that exhibit a remarkable isotope effect are then compared with semiclassical calculations.

Finally, in Chapter 6, the charge-state-resolved kinetic energy spectra of Sn ions ejected from the Sn-LPP have been reported at various densities of the H_2 buffer gas surrounding the microdroplet LPP. The production of keV Sn^{+} ions from Sn^{2+} ions, as observed in the LPP experiments, is explained on the basis of electron capture by metastable Sn^{2+*} ions.

Bibliography

[1] G. E. Moore, Electronics **38**, 114 (1965).

[2] G. E. Moore, Proc. IEDM Tech. Dig. **11**, 11 (1975).

[3] C. A. Mack, IEEE Trans. Semicond. Manuf. **24**, 202 (2011).

[4] A. J. den Boef, Surf. Topogr. **4**, 023001 (2016).

[5] J. Benschop, V. Banine, S. Lok, and E. Loopstra, J. Vac. Sci. Technol. B **26**, 2204 (2008).

[6] I. Fomenkov, D. Brandt, A. Ershov, A. Schafgans, Y. Tao, G. Vaschenko, S. Rokitski, M. Kats, M. Vargas, M. Purvis, R. Rafac, B. La Fontaine, S. De Dea, A. LaForge, J. Stewart, S. Chang, M. Graham, D. Riggs, T. Taylor, M. Abraham, and D. Brown, Adv. Opt. Technol. **6**, 173 (2017).

[7] F. Torretti, Ph.D. thesis, Vrije Universiteit, Amsterdam (2019).

[8] Q. Huang, V. Medvedev, R. van de Kruijs, A. Yakshin, E. Louis, and F. Bijkerk, Appl. Phys. Rev. **4**, 011104 (2017).

[9] S. Bajt, J. B. Alameda, T. W. Barbee Jr., W. M. Clift, J. A. Folta, B. Kaufmann, and E. A. Spiller, Opt. Eng. **41**, 1797 (2002).

[10] V. Y. Banine, K. N. Koshelev, and G. H. P. M. Swinkels, J. Phys. D: Appl. Phys. **44**, 253001 (2011).

[11] G. O'Sullivan, B. Li, R. D'Arcy, P. Dunne, P. Hayden, D. Kilbane, T. McCormack, H. Ohashi, F. O'Reilly, P. Sheridan, E. Sokell, C. Suzuki, and T. Higashiguchi, J. Phys. B: At. Mol. Opt. Phys. **48**, 144025 (2015).

[12] J. Colgan, D. Kilcrease, J. Abdallah, M. Sherrill, C. Fontes, P. Hakel, and G. Armstrong, High Energy Density Phys. **23**, 133 (2017).

[13] F. Torretti, J. Sheil, R. Schupp, M. M. Basko, M. Bayraktar, R. A. Meijer, S. Witte, W. Ubachs, R. Hoekstra, O. O. Versolato, A. J. Neukirch, and J. Colgan, Nat. Commun. **11**, 2334 (2020).

[14] O. O. Versolato, Plasma Sources Sci. Technol. **28**, 083001 (2019).

[15] M. M. J. W. van Herpen, D. J. W. Klunder, W. Soer, R. Moors, and V. Banine, Chem. Phys. Lett. **484**, 197 (2010).

[16] D. T. Elg, J. R. Sporre, D. Curreli, I. A. Shchelkanov, D. N. Ruzic, and K. R. Umstadter, J. Micro/ Nanolithogr. MEMS MOEMS **14**, 1 (2015).

[17] R. W. Coons, S. S. Harilal, D. Campos, and A. Hassanein, J. Appl. Phys. **108**, 1 (2010).

[18] H. Tanaka, Y. Hashimoto, K. Tamaru, A. Takahashi, and T. Okada, Appl. Phys. Lett. **89**, 181109 (2006).

[19] T. Higashiguchi, C. Rajyaguru, N. Dojyo, Y. Taniguchi, K. Sakita, S. Kubodera, and W. Sasaki, Rev. Sci. Instrum. **76**, 126102 (2005).

[20] S. Fujioka, H. Nishimura, K. Nishihara, M. Murakami, Y.-G. Kang, Q. Gu, K. Nagai, T. Norimatsu, N. Miyanaga, Y. Izawa, K. Mima, Y. Shimada, A. Sunahara, and H. Furukawa, Appl. Phys. Lett. **87**, 241503 (2005).

[21] S. Srivastava, K. Thompson, E. Antonsen, H. Qiu, J. Spencer, D. Papke, and D. Ruzic, J. Appl. Phys. **102**, 023301 (2007).

[22] V. Bakshi, ed., *EUV Sources for Lithography*, SPIE Press monograph (SPIE Press, 2006).

[23] Y. Ueno, G. Soumagne, A. Sumitani, A. Endo, T. Higashiguchi, and N. Yugami, Appl. Phys. Lett. **92**, 211503 (2008).

[24] S. S. Harilal, B. O'Shay, M. S. Tillack, and M. V. Mathew, J. Appl. Phys. **98**, 013306 (2005).

[25] V. Bakshi, ed., *EUV Lithography*, 2nd Edition ed. (SPIE Press, 2018).

[26] M. van de Kerkhof, A. M. Yakunin, V. Kvon, A. Nikipelov, D. Astakhov, P. Krainov, and V. Banine, Radiat. Eff. Defects Solids **177**, 486 (2022).

[27] J. Beckers, T. van de Ven, R. van der Horst, D. Astakhov, and V. Banine, Appl. Sci. **9**, 2827 (2019).

[28] A. Kuznetsov, R. Kruijs, M. Gleeson, K. Schmid, and F. Bijkerk, J. Surf. Invest. **4**, 563 (2010).

[29] D. Nakamura, K. Tamaru, Y. Hashimoto, T. Okada, H. Tanaka, and A. Takahashi, J. Appl. Phys. **102**, 123310 (2007).

[30] D. Abramenko, M. Spiridonov, P. Krainov, V. Krivtsun, D. Astakhov, V. Medvedev, M. van Kampen, D. Smeets, and K. Koshelev, Appl. Phys. Lett. **112**, 164102 (2018).

[31] R. K. Janev and H. Winter, Phys. Rep. **117**, 265 (1985).

[32] G. G. van Eden, T. W. Morgan, D. U. B. Aussems, M. A. van den Berg, K. Bystrov, and M. C. M. van de Sanden, Phys. Rev. Lett. **116**, 135002 (2016).

[33] R. E. Nygren and F. L. Tabarés, Nucl. Mater. Energy **9**, 6 (2016).

[34] G. G. Eden, V. Kvon, M. C. M. van de Sanden, and T. W. Morgan, Nat. Commun. **8**, 192 (2017).

[35] A. Bayerle, M. J. Deuzeman, S. van der Heijden, D. Kurilovich, T. de Faria Pinto, A. Stodolna, S. Witte, K. S. E. Eikema, W. Ubachs, R. Hoekstra, and O. O. Versolato, Plasma Sources Sci. Technol. **27**, 045001 (2018).

[36] D. J. Hemminga, L. Poirier, M. M. Basko, R. Hoekstra, W. Ubachs, O. O. Versolato, and J. Sheil, Plasma Sources Sci. Technol. **30**, 105006 (2021).

[37] L. Poirier, A. Lassise, Y. Mostafa, L. Behnke, N. Braaksma, L. Assink, R. Hoekstra, and O. O. Versolato, Appl. Phys. B **128**, 1 (2022).

[38] W. Fritsch and C. D. Lin, Phys. Rep. **202**, 1 (1991).

[39] J. F. Ziegler, M. Ziegler, and J. Biersack, Nucl. Instrum. Methods Phys. Res. B **268**, 1818 (2010), 19th International Conference on Ion Beam Analysis.

[40] K. N. Yu, C. W. Y. Yip, D. Nikezic, J. P. Y. Ho, and V. S. Y. Koo, Appl. Radiat. Isot. **59**, 363 (2003).

[41] K. Wittmaack, J. Appl. Phys. **96**, 2632 (2004).

[42] N. V. Novikov, Y. A. Teplova, Y. A. Fainberg, and V. S. Kulikauskas, Nucl. Instrum. Methods Phys. Res. B **235**, 448 (2005).

[43] H. Paul, Nucl. Instrum. Methods Phys. Res. B **247**, 166 (2006).

[44] P. Filliatre, C. Jammes, and B. Geslot, Nucl. Instrum. Methods Phys. Res. A **618**, 294 (2010).

[45] M. P. Seah and T. S. Nunney, J. Phys. D: Appl. Phys. **43**, 253001 (2010).

[46] M. Jurado Vargas and A. Fernández Timón, J. Radioanal. Nucl. Chem. **305**, 479 (2015).

[47] J. P. J. Dubois, K. Achkasov, D. Kogut, A. Ahmad, J. M. Layet, A. Simonin, and G. Cartry, J. Appl. Phys. **119**, 193301 (2016).

[48] H. Over, Y. B. He, A. Farkas, G. Mellau, C. Korte, M. Knapp, M. Chandhok, and M. Fang, J. Vac. Sci. Technol. B **25**, 1123 (2007).

Chapter 2

Scattering of keV tin ions from Mo and Ru surfaces

Abstract

The scattering of Sn ions from Mo and Ru surfaces is studied. The experiments show that the energy distributions of scattered ions are dominated by multiple collision scattering, leading to a broad energy spectrum. We compare the results with the predictions of a widely used simulation package, SRIM. These predictions are broadly in agreement with the experimental data, except for the notable, complete absence in the experimental data of the single-collision peak that is so pronounced in the simulations. The charge state (1+ - 4+) and energy (7 - 28 keV) of the incoming tin ions is changed, two samples (Mo and Ru) are used, and additional time-of-flight spectroscopy measurements are performed to determine the energy of neutral scattered particles. All tests confirm the absence of an appreciable single-collision peak, hinting that the presence of the strong single-collision peak in the simulations has SRIM-related causes, for instance, the neglect of pre-scattering interactions in front of the surface, the use of a fixed distance between consecutive collisions or that the generic potential used is suboptimal for Sn-Mo and Sn-Ru scattering.

2.1 Introduction

In modern nanolithography machines extreme ultraviolet (EUV) light of 13.5 nm is used. The 13.5-nm EUV light is provided by an intense tin plasma source[1, 2]. The hot plasma is produced by stroboscopic irradiation of a stream of liquid Sn microdroplets by energetic laser pulses. Within the plasma source highly charged Sn^{8+} - Sn^{14+} ions are responsible for emitting EUV photons in a narrow band around 13.5 nm [3]. The 13.5-nm EUV light is collected and transported by Mo/Si multilayer mirrors [4]. Thin Ru films of a few nm only are routinely used as protective caps of EUV multilayer mirrors[5–8]. Experiments have shown that RuO_2 layers of a fraction of the thickness of the capping layer are quite stable against further oxidation, except when co-exposed to high fluxes of electrons or EUV photons or when directly exposed to atomic O. This resistance against oxidation makes Ru an excellent material for the protection of the EUV multilayer mirrors against oxidation which on its turn would lead to degradation of the reflectance of the multi mirrors. As a by-product, such LPP-type EUV light sources generate tin ions in charge states up to 8+ and at kinetic energies reaching as high as dozens of keV [1, 9, 10]. If the ions are not mitigated, they will interact with the neighboring walls and the Mo/Si multilayer mirror The interaction between projectile atoms and surfaces can be simulated in order to understand and predict the consequences of this interaction.

Many simulation packages exist [11, 12] to describe and track the trajectories and stopping of energetic particles impinging on and penetrating solid samples. One commonly used code for these kinds of simulations is SRIM [13, 14]. This package allows a wide range of energies and incidence angles for incoming particles and simulates the particle stopping in the target, the trajectories, and range, and the backscattered and sputtered particles emitted from the surface. The target can have single and multiple layers, which can be a mixture of different isotopes. SRIM does not consider charge in its simulations but treats both the projectile and the target as neutral atoms.

Many experimental tests on the output of SRIM have been conducted, but the focus was mainly on sputter yields [15–19] or on stopping powers [20, 21] and the bulk of data is for low-Z projectile ions [22, 23]. Tests of the simulations for scattering from the surface are uncommon but do exist [24, 25], though again mainly for light ions. Qualitatively SRIM produces good agreement with the experimental data in those tests, however at a quantitative level often significant differences in sputter yields are found. Also, deviations in the angular sputter yields are found, and the simulations do not agree with the experiments for ion beams below 1 keV (e.g. see ref. 17). An extensive, systematic test of the SRIM predictions to low-energy keV heavy ions impinging on a heavy surface, such as Sn ions on Mo or Ru, appears to be missing.

Sputter yields and the sputtered particles’ energy distributions are notoriously hard to measure as most of the particles are neutral and of low energy. Here we focus on the first step triggering a potential sputter cascade namely the initial binary collision between incoming ion and target atom to check whether at least these initial interactions are appropriately simulated by SRIM, by investigating the backscattering of tin ions from Mo and Ru samples. Backscattering (LEIS: low-energy ion scattering[26]) probes the topmost atomic layers only and should allow for a rather direct, clean comparison to simulations. In addition, it is the topmost layer that contributes most to sputtering and damage thresholds. We compare our backscattering results with the predictions by SRIM and investigate the limitations and the range where the simulations are applicable for ion-surface collisions of relatively heavy ions. This gives more insight into these collisions and the underlying processes, and the extent to which SRIM can be used to predict accurately the outcome of keV ionic interactions with transient metals such as Ru and Mo.

We record the scattered ion energy distribution for kinetic energies up to 28 keV, for a wide range of incidence and scattering angles. Throughout the paper, 14 keV Sn^{2+} on Mo is used as our reference system. Also included is an investigation into the influence of charge state as a parameter, and a comparison is made with other ion beams and between Mo and Ru samples. We find some distinct deviations in the simulations from the experimental data which can only be explained by the limitations of the software package.

2.2 Tin ion scattering

2.2.1 Experimental procedure

The primary tin ion beam is extracted from a SUPERNANOGAN-type electron cyclotron resonance ion source and charge-over-mass separated by a 110° analyzing magnet. The ion beam is transported towards the collision chamber positioned 15 m downstream of the ion source by means of a series of three magnetic quadrupole triplets after which in front of the setup a 45° dipole magnet for final mass-over-charge clean up of the ion beam is installed. The setup as a whole can be floated on high voltage to lower the ion energy down to a few tens of eV only. The energy at which the ion beam impinges on the transition metal targets is given by the difference between the voltages on the ion source and the set-up and a small additional contribution due to the plasma potential of the source ($\approx 10 \times q$ eV, with q the charge state of the ions[27]).

In the present experiments, the setup [28] was operated at ground potential unless stated otherwise. The experiments are performed with a base pressure in the order of 10^{-8} mbar, as measured with an ion gauge mounted on the collision chamber. The gas composition is checked with a residual gas analyzer, showing that most of the background gas consists of oxygen-containing molecules. To obtain information on the oxidation of the targets, XPS measurements on the Ru target have been performed in our XPS set-up [29] operated, which was also run at a base pressure of 10^{-8} mbar. The transport from collision setup to XPS occurs through the air. Therefore the first XPS show two O lines corresponding to O bound to Ru and looser bound O in e.g. O_2, CO, or OH bonds. Ar ion sputter-cleaning readily removes the loosely bound component (probably stemming from the sample transport through the air). On this partially cleaned sample, using the split $3d_{5/2}$ line of Ru (pure Ru and Ru-O) we determined Ru and O percentages of 53 and 47%, respectively. Ru forms thin RuO_2 surface layers, order of 1 nm (e.g. [5, 6, 8]. The fact that percentages differ from 33 and 67% (RuO_2), results from XPS probing a finite depth slightly reaching beyond the top atomic layers. The higher fraction of Ru is therefore due to XPS probing some of the deeper clean Ru layers. This is in line with oxidation of the surface layer(s) only.

The poly-crystalline Mo and Ru targets are mounted on a high precision manipulator for accurate rotation of the sample around two axes in order to adjust the angle of incidence (ψ) and the azimuthal angle (ϕ), which was kept fixed in the experiments. The targets have been cleaned by cycles of Ar ion sputtering and annealing. These cycles have been repeated in-between the measurements. Different grains are likely to have different sputter rates and therefore over large areas no smooth surface can be assumed. This large-scale roughness can not be remedied by annealing. Annealing leads to local atomic-scale healing. However, a local smooth structure (3 to 5 atoms) suffices for a comparison of our backscattered particle distributions to the ones generated by SRIM simulations.

The incidence angles with respect to the surface ranged from 5° to 30° and the scattering angles (θ) ranged from 10° to 60°. Charged scattered particles are energy selected and detected by a rotatable, high-precision electrostatic analyzer (ESA) with an opening angle of about 0.3°. The main target used in this work is poly-crystalline Mo, prepared by Surface Preparation Lab (SPL, Zaandam, the Netherlands). Mo has seven naturally abundant isotopes, with an average mass of 95.9 u. A tin ion, which is heavier than atomic Mo, has therefore a maximum scattering angle of 53.1° for a hypothetical Mo atom of average mass, and 56.4° for the heaviest Mo isotope (^{100}Mo). For Ru which is slightly heavier, the maximum scattering angles are thus slightly larger. The main Sn ion beam used is a 14 keV isotopically pure $^{120}\mathrm{Sn}^{2+}$ beam. After a final set of 2-mm diaphragms, the $^{120}\mathrm{Sn}^{2+}$ beam impinges on the target with a current typically close to 1 nA. For comparative measurements also beams of $^{120}\mathrm{Sn}^{1+}$, $^{120}\mathrm{Sn}^{4+}$, $^{84}\mathrm{Kr}^{1+}$, and $^{129}\mathrm{Xe}^{2+}$ were used.

All ESA spectra consist of a summed series of kinetic energy scans. The number of individual scans differs between spectra and is determined by statistics, but is at least three. For every single energy point, the beam current on the target is recorded. The number of counts per second is divided by the accumulated beam current to remove the effects of beam fluctuations from the spectra. Finally, as the ESA operates in fixed $E/\Delta E$ mode, each data point is divided by energy, to correct for the changing energy bin width ΔE of the ESA with kinetic energy.

At a scattering angle of 40°, a Time-of-Flight (ToF) spectrometer is mounted to the collision chamber, allowing for the detection of both neutral and ionic particles, given that their kinetic energy is sufficiently high to trigger a signal on the channeltron detector.

2.2.2 Typical tin scattering results

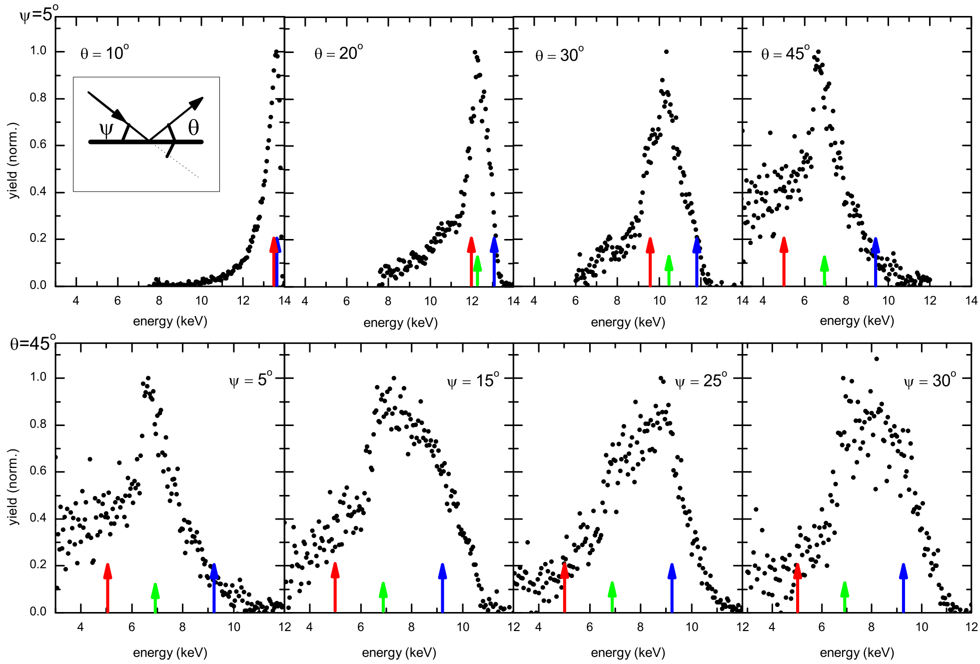

Figure 2.1: *Compilation of typical energy spectra of 14 keV* Sn^{2+} *scattering off Mo. Top row: For a constant incidence angle of* $\psi = 5°$ *and scattering (detection) angles* θ *of 10 to 45°. Bottom row: For a constant scattering (detection) angle of* $\theta = 45°$ *and incidence angle* ψ *of 5° to 30°. The energy positions of single and symmetric double scattering are marked by red and blue arrows, respectively. The green arrows indicate the positions of primary Mo recoils. The inset in the top-left panel shows the definition of the incidence and scattering angles.*

Figure 2.1 shows two series of scattering measurements using an ion beam of 14 keV Sn^{2+}, one for a constant grazing angle of incidence ψ of 5° (top row) and another for a constant scattering angle θ of 45° (bottom row). The constant ψ series shows the spectra for an increasing θ: 10°, 20°, 30°, and 45°. As the scattering angle increases, the ion energy distributions peak at lower energies, and the maximum energy is lower, as larger scattering angles require more energy to be transferred. For our geometry a single, pure two-body collision between a projectile of mass m_p with kinetic energy E_0 and a target atom of mass m_t the final energy of the scattered projectile E_f is given by[26]:

$$\frac{E_f}{E_0} = \left(\frac{\cos(\theta) + \sqrt{(m_t/m_p)^2 - \sin^2(\theta)}}{1 + m_t/m_p} \right)^2 . \tag{2.1}$$

Scattered particles resulting from two, three, or more consecutive collisions contribute largely to the energy spectra. This results in broader spectra. As the pathway through the target becomes longer before the ion leaves the surface more energy (straggling) is lost. On the other hand, two successive collisions each over half of the detection angle lead to scattered particle energy higher than the one of a single collision over the full detection angle. Asymmetric double collisions lead to final energies in between the energies of single collision (SC) and symmetric double collision (SDC) events. In figure 2.1 the energy positions of single and symmetric double scattering are marked by red and blue arrows, respectively. By and large, the spectral intensities fall between those two energies with a straggling tail extending to lower energies. For later discussion, it is already of note that no appreciable SC peak is manifest in the spectra.

From the constant θ series (bottom row Figure 2.1) it is seen that although in all cases the scattering angle is the same the spectral shapes do differ. The spectrum taken at the smallest incidence angle is the sharpest peaked, and its maximum is located at a lower energy ($\sim$ 6.7 keV) than in the other three spectra (8 to 9 keV range). For $\psi = 15°$, $25°$, and $30°$, the broad structures' maxima extend to just below the energy of symmetric double scattering. The narrower and lower energy of the distribution for $\psi = 5°$ hints strongly at pre-scattering effects in front of the surface at this grazing angle of incidence. Gradual pre-scattering on the incoming trajectory implies that the projectiles move over a longer trajectory almost parallel to the surface thereby effectively reducing the SC scattering angle from $45°$ to $40°$. Single scattering over $40°$ corresponds to an energy of 6.7 keV as observed in the measurements. In addition, when pre-scattering bends the incoming trajectories parallel to the surface double collision events are basically not possible. This likely explains the fast drop in intensity at higher energies.

The highest energy at which scattered particles are detected is 11.5 keV at a scattering angle of $\psi = 25°$. For $\psi = 15°$ and $\psi = 30°$ the maximum energy is $\sim$11 keV, and for $\psi = 5°$ the maximum energy is lowest ($\sim$10.5 keV). For near-specular incidence and detection angles ($\theta \approx 2\psi$), more combinations of multiple-collision scattering with smaller individual collision angles are possible, leading on average to higher kinetic energies of the scattered ions.

Energetic target ions sputtered from the surface layers may contribute to the kinetic energy spectra. Mo ions recoiled out off the surface in one direct collision with a Sn projectile, the so-called primary recoils, have well-defined energy given by:

$$\frac{E_{rec}}{E_0} = \frac{4m_t m_p}{(m_t + m_p)^2} \cos^2(\theta). \tag{2.2}$$

Primary Mo particles recoiled over 45° by 14 keV Sn ions obtain kinetic energy of 6.9 keV. In all spectra there are weak traces of enhanced yields at the energy of primary recoils, see e.g. bottom row figure 2.1. In general, the ion scattering distributions are dominated by multiple collision scattering which by and large stem from trajectories diving below the topmost surface layer. Secondary sputtered particles have mainly low energies $\ll 1$ keV and therefore do not contribute at the energy range in which backscattered ions are measured.

2.2.3 SRIM simulations

We will compare the spectra with the output of the simulations of SRIM [13, 14], and investigate the accuracy of this simulation package. For comparison to the experiments, the backscattered particles are required to be in the plane defined by the ion beam and the detector plane within a 3° limit set on angles out of this plane. Concerning the scattering or detection angle, for detection angles, $\leq 40°$ only particles which are within 1° of the detection angle are counted. For larger scattering angles, which have smaller cross sections the angular acceptance is set at 2.5°. A histogram of the final kinetic energies of the particles which pass these angle tests emulates an experimental spectrum and can be compared with the experimental results. The SRIM acceptance angles used are larger than the actual acceptance angle of the ESA (0.3°).

We select the isotopes used in the experiments as an incoming ion in SRIM: for tin, this is ^{120}Sn. As the target surface we use, unless otherwise specified, a mixture of the seven most abundant isotopes of Mo according to their natural abundances. This will lead to the spectral broadening of the energy distributions, in particular of the single scattering peaks, compared to using an average target-atom mass. As the calculation method, we use *monolayer surface collisions*, which is recommended for ion interactions near the edge of the surface[13]. For each spectrum, six million particle trajectories are simulated unless specified otherwise. The same procedure is used for collisions on a Ru sample.

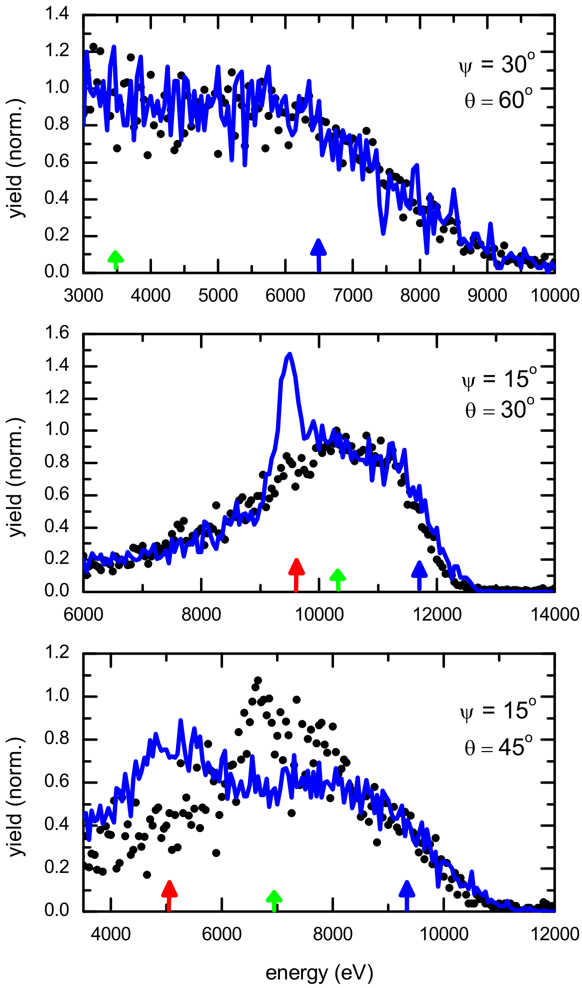

Figure 2.2: *Comparison of experimental (black symbols) and SRIM (blue line) energy spectra for 14 keV Sn^{2+} ions impinging on Mo, for three combinations of incidence ψ and scattering angle θ. The energy positions of single and symmetric double scattering are marked by red and blue arrows, respectively. The green arrows indicate the positions of primary Mo recoils.*

2.3 Results and discussion

In figure 2.2, the scattered-energy distributions of 14 keV Sn^{2+} impact on Mo are presented for three typical (ψ, θ) combinations and compared to the predictions of SRIM simulations. Unless stated otherwise in the comparison of experimental and SRIM spectra, the spectra are scaled to optimize visually the overlap between the two. The experimental energy distribution for (ψ, θ)=(30,60) is in excellent agreement with the simulations. For (ψ, θ)=(15,30) an additional peak on top of the broad distribution is apparent in the simulations, but absent in the experimental data. This peak is located exactly at the energy of single-collision scattering of a Sn projectile from a Mo atom. Analysis of the trajectories of the simulated particles indicates that the particles in this peak are the result of a single collision in the upper layer of the surface. Also for (ψ, θ)=(15,45) in the SRIM results additional intensity is observed near the energy of the SC peak. Due to smaller cross sections for large angle scattering, the peak is less pronounced. For (ψ, θ)=(30,60), single collision scattering over 60° is not possible as the maximum scattering angle is around 53° for Sn - Mo scattering.

The single-collision peak which appears to be absent in all our experimental spectra is prominent in all SRIM simulations for which the scattering angle θ is $\geq 2\psi$ but still less than the maximum scattering angle of ~53°. The fact that for scattering angles between ψ and 2ψ SRIM does not show an SC peak is an artifact of SRIM's algorithm defining the sequence of collisions, which will be discussed in subsection 2.3.5. SRIM predicts a significant primary recoil peak, though for all scattering angles at an energy of approximately 40% of the energy calculated from the binary recoil expression (eq. 3.2). At the energies predicted by SRIM, no peaks were observed in the experimental spectra. The prediction of apparently too low recoil energies hinders a detailed assessment of possible contributions near energies of the expected primary recoil energy. It is to be noted that the primary recoil process is stemming from exactly the same type of binary collisions as the single-collision backscattered particles for which SRIM predicts energies in agreement with eq.3.1.

In the next subsections, we consecutively perform tests on the role of specific parameters and aspects of the experiments and simulations which in principle might contribute to the discrepancy between experiment and SRIM concerning respectively the absence or presence of a single scattering peak:

A Scattered-ion fractions: the charge state and energy of the ion beam is varied to look for any charge state and energy-dependent features in the energy distributions.

B Ion species: the scattered-energy distributions for two other heavy-ion beams, Kr and Xe are presented and compared to SRIM simulations.

C Target species: hypothetically, the absence of the single-collision peak might stem from the characteristics of the target species, therefore comparative results for Sn ion impact on Mo and Ru and the potential role of oxidation are

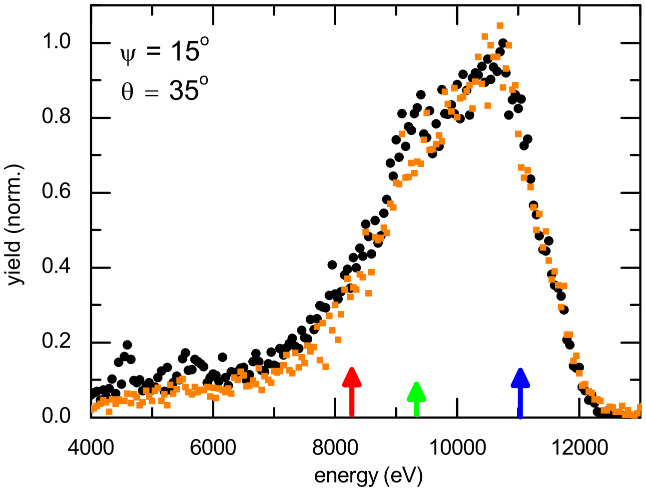

Figure 2.3: *Kinetic energy spectra for 14 keV Sn^{2+} (black) and Sn^{4+} (orange) ions incident on Mo at 15° and scattered over 35°. The energy positions of single and symmetric double scattering are marked by red and blue arrows, respectively. The green arrows indicate the positions of primary Mo recoils.*

discussed.

D Scattered neutrals: with the ESA only charged particles are measured. Most often the by far largest fraction ($\geq$ 95%) of scattered particles is neutral. To assess the energy spectra of those neutrals additional Time-of-flight (ToF) measurements are performed.

E SRIM approaches: possible reasons why approximations underlying the SRIM simulation package might contribute to the deviations from the experimental observations are discussed.

2.3.1 Scattered-ion fractions

In the ESA only Sn^{1+} ions are detected, however typically the fraction of scattered ions is only a small fraction of all scattered particles. This fraction does depend on the incoming charge state, velocity and the electronic structure of the target, e.g. [30, 31]. To assess the effect of the charge state of the incoming ions we performed experiments with 5 keV and 14 keV tin beams. At each energy two charge states were used: 1+ and 2+ for the 5 keV beam, and 2+ and 4+ for the 14 keV one. The 5 keV Sn^{2+} beam is decelerated from a primary beam of 14 keV Sn^{2+} and the 14 keV

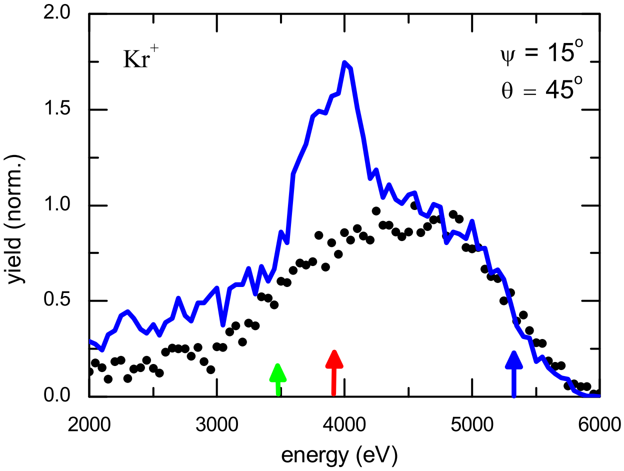

Figure 2.4: *Measured Kr ion scattering spectrum (dots) and the corresponding predictions (line) by SRIM for a 7 keV Kr$^+$ ion beam on Mo with ψ = 15° and θ = 45°.The energy positions of single and symmetric double scattering are marked by red and blue arrows, respectively. The green arrow indicates the positions of primary Mo recoils.*

Sn^{4+} beam from 28 keV Sn^{4+}. In figure 2.3, as an example the comparison is shown of 14 keV Sn^{2+} and Sn^{4+} ions. There are no appreciable differences between both spectra. In none of the backscattered-ion spectra, no matter whether the incident beam is Sn^{1+}, Sn^{2+}, and Sn^{4+}, traces of a single-collision peak are observed.

The absence of the SC peak holds over the full range of energies studied 5 - 28 keV. As over this energy range the interaction time in single Sn - Mo collisions changes by more than a factor of 2, a dip in the ion fractions which is observed over a narrow energy range in a few specific ion - atom systems, e.g. He^{2+} ion scattering on Pb surfaces[32], cannot be inferred as a possible ground for the absence of the SC peak in the experiments. It is therefore concluded that there is no significant charge state or velocity dependency. It is thus unlikely that any deviations between the experimental results and the SRIM predictions are caused by the fact that SRIM does not explicitly consider the charge state of the particles.

2.3.2 Ion species

To exclude the faint possibility that the absence of the SC peak is purely a tin-related feature, we have performed experiments with keV Kr and Xe ion beams. While the ^{120}Sn ions used are heavier than Mo atoms (95.9 u on average), Kr is a bit lighter than Mo, therefore single scattering is possible over all angles. We use a 7 keV ^{84}Kr$^+$

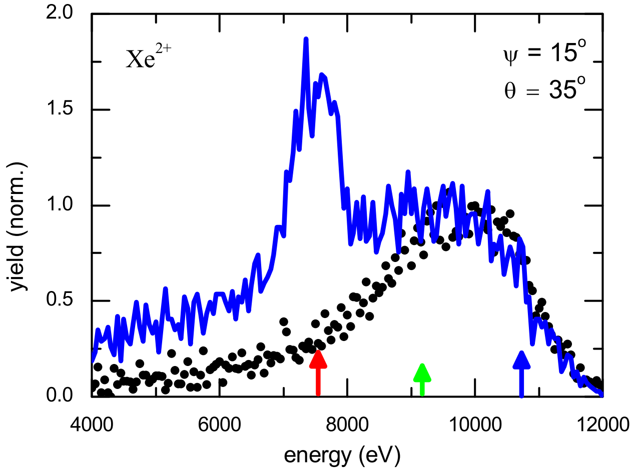

Figure 2.5: *Measured Xe ion scattering spectrum (dots) and the corresponding SRIM predictions for a 14 keV Xe*$^{2+}$ *ion beam on Mo with* ψ = 15° *and* θ = 35°. *The energy positions of single and symmetric double scattering are marked by red and blue arrows, respectively. The green arrow indicates the positions of primary Mo recoils.*

ion beam, which has a similar ion velocity as the 14 keV ^{120}Sn^{2+} ion beam primarily used in our Sn - Mo experiments. In figure 2.4, a typical example of these krypton scattering experiments and the corresponding SRIM predictions is shown for (ψ,θ) is (15,45). At 3.9 keV, the simulations show a typical SC peak which just as in the Sn ion experiments is not observed in the experimental data. Furthermore, the SC peak is absent in all krypton scattering distributions also for large angles, which can not be reached using Sn ions.

Figure 2.5 shows the energy distribution for scattering over 35° of 14 keV ^{132}Xe^{2+} ions, incident at 15° on the Mo target and its corresponding SRIM prediction. Again no SC peak shows up in the experimental data in contrast to the SRIM simulation which exhibits an SC peak at ~7.5 keV.

For both Kr and Xe, the differences to the SRIM simulations are similar as in the Sn experiments. The absence of the SC peak in the energy distributions is not a tin-specific feature but is shared with other ion species.

When changing the ion species not only the mass of the incoming projectile is changed but also its electronic structure. The Ziegler-Biersack-Littmark (ZBL) potential[13, 14], the standard, generic interatomic potential used in SRIM is independent of the mass of a particle but does depend on the nuclear charge, which is 50 and 54 for respectively Sn and Xe. This leads to a small difference between the Sn-Mo potential

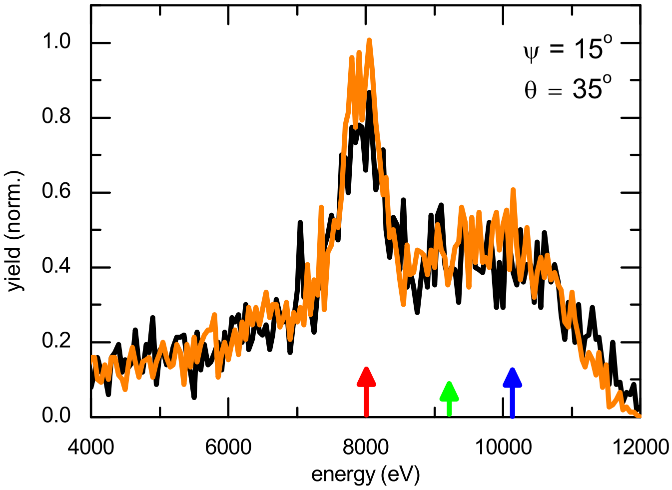

Figure 2.6: *The SRIM predictions for ψ = 15° and θ = 35° for 14 keV Sn (black) and Xe (orange) scattering off Mo. The atomic masses of Sn and Xe are taken equal, i.e., 124 u. The energy positions of single and symmetric double scattering are marked by red and blue arrows, respectively. The green arrow indicates the positions of primary Mo recoils. The spectra have not been scaled with respect to each other.*

and the Xe-Mo potential, where the latter is slightly higher. The Coulomb repulsion part is 8% higher, and the screening length is 1% smaller (0.1820 for Xe-Mo and 0.1836 for Sn-Mo). These small differences in the potentials are not expected to affect the scattering and ion energy distributions appreciably. To verify this assumption, figure 2.6 presents the predictions of SRIM for Sn and Xe ions of the same mass of 124 u, which are naturally (low-) abundant isotopes of each species. There is barely any difference between both spectra. It is therefore unlikely that the electronic structure of the projectile ions, not explicitly included in SRIM, causes the differences between SRIM and experimental energy distributions.

2.3.3 Target species

To test the influence of the transition metal target used the Mo target is replaced by a Ru one. Ru is the second heavier neighbor of Mo, with an average mass of 101 u. Ions scattering from Ru have therefore a slightly higher kinetic energy for the same scattering angle as compared to Mo. The maximum scattering angle for Sn ions impinging on a Ru target is $\theta_{max} = 60.1^\circ$ for the heaviest isotope. The element has 7 stable abundant isotopes, ranging from 96 to 104. The Ru target in our

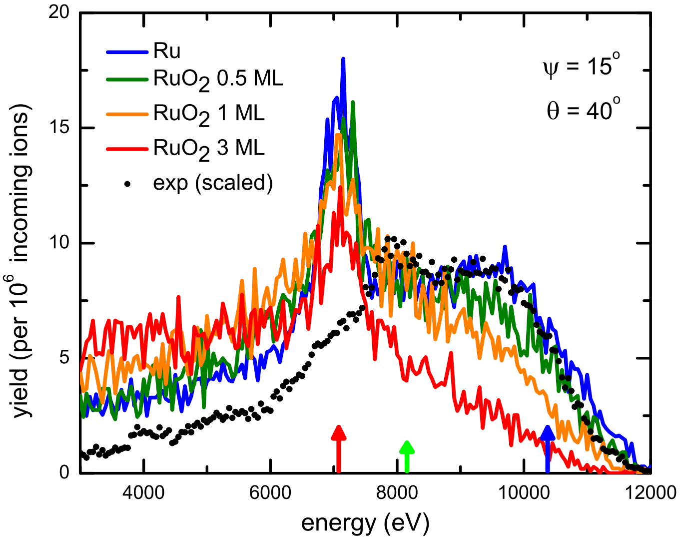

Figure 2.7: *Comparison of experimental and SRIM energy spectra for 14 keV* Sn^{2+} *ions impinging on Ru and* RuO_2*. The simulations have been performed for increasing oxidation of the top atomic layers of the sample, i.e., thicknesses corresponding to 0, 0.5, 1, and 3 monolayers (ML) of* RuO_2*. The energy positions of single and symmetric double scattering on Ru are marked by red and blue arrows, respectively. The green arrow indicates the positions of primary Ru recoils.*

SRIM simulations is, as done for Mo, a mixture of these isotopes with the natural abundance ratio.

The results of a 14 keV Sn^{2+} ion beam scattering off Ru for $(\psi,\theta) = (15{,}40)$ are depicted in figure 2.7 as representative of all angular measurements. The predictions by SRIM are in agreement with the experimental results but, as before for scattering from Mo, SRIM predicts a significant single-collision peak. And as for Mo, the SC peak is absent in the experimental ion energy distribution. For all angular combinations studied on Ru, the results and their comparison to the SRIM simulations are very similar to the case of Mo. Therefore the absence of the SC peak is not a specific feature of Mo as for Ru the SC peak is absent too.

At vacuum pressures of 10^{-8} mbar, the surfaces can not be kept clean. From the ion scattering perspective, replacing Ru by RuO_2 reduces the number of Ru atoms in the topmost surface layer(s) and consequently, the probability to single-scatter off a Ru atom is lower. Single-scattering on an O atom does lead to different final energy of the scattered Sn particle. Moreover, the maximum scattering angle for

Sn colliding on O is only just over 7°, therefore at the scattering angles used here no direct contributions from O are to be expected. Figure 2.7 includes SRIM simulations for different thicknesses of layers of RuO_2 to illustrate how increased oxide layers may affect the scattering spectra. For 3 ML of RuO_2, there is still a clear SC signature. Beyond 3 ML the spectrum does not change significantly anymore as most of the energetic backscattered particles stem from interactions from the topmost atomic layers.

As the oxide layer thickness increases the contributions from double- and multiple collisions disappear such that above 8 keV the shape of the spectrum does not resemble the experimental one at all. As multiple-collision probabilities scale with power n, with n the number of collisions, the high-energy part of the spectrum beyond the SC peak scales much stronger with the reduction of Ru atoms in the surface layers than the SC peak intensity. Thus Ru oxide layers or other small amounts of surface contamination cannot explain the absence of the SC peak in the experimental data.

2.3.4 Scattered neutrals

The ESA spectra discussed so far are based solely on the measurement of charged particles. As mentioned before the by far largest fraction (typically $\geq 90\%$) of scattered particles is neutral. On basis of the fact that the spectra did not change when changing the charge state and energy of the Sn ions (cf. 2.3.1) it seems very unlikely that single-collision events only produce neutrals. Nevertheless, we have installed at a scattering angle of $\theta = 40°$ a Time-of-flight (ToF) system to the scattering chamber to measure the energy spectra of scattered neutrals. In principle, the ToF detector records both ions and neutral particles. The inner tube of the ToF system can be floated on a high voltage to accelerate or decelerate ions while the atoms are not affected. By doing so no differences in the ToF spectra were observed indicating that the ion contribution to the ToF spectra is negligibly small.

In figure 2.8, the ToF spectrum of a 14 keV Sn^{2+} beam on a Ru target is shown, for an incidence angle of 15° and a detection angle of 40°. Two peaks are visible: a sharp peak around 3.5 μs and a broad peak between 5 and 10 μs. The flight times of the particles making up the sharp peaks are too short to belong to backscattered Sn. The ToF instead corresponds to the primary recoil energy of an O particle sputtered over 40° (3.4 keV, see eq. 3.2). A small shoulder is visible on the short-ToF wing of the O peak, which corresponds to the energy of primary C recoils (2.7 keV). The sharp peak is therefore the result of low-Z contamination at the surface. This O (and C) peak is not present in the ion-energy distributions measured with the ESA, which suggests that the ionization degree of primary contamination recoils is significantly lower than the ionization degree of the scattered Sn particles. The strength of the

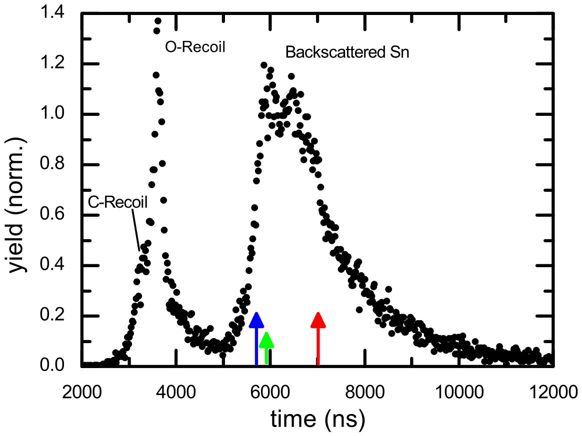

Figure 2.8: *Full ToF spectrum of 14 keV Sn^{2+} ions on a Ru target for ψ is 15° and θ is 40°. The spectrum is not corrected for detection efficiency implying that the low-Z recoils appear over-represented.*

contamination contribution is also a sign of background gas sticking to the target after cleaning and annealing of the target.

The broad peak in the ToF spectrum corresponds to energies of backscattered Sn, that are the same as determined in our ESA measurements and SRIM simulations. It has a sharp rise for the shorter flight times (corresponding to higher kinetic energies), a broad maximum, and a long-ToF tail. The maximum seems to be double-peaked, with peaks at roughly 6 and 6.5 μs. For discussion of the spectral features figure 2.9 shows only the part of the ToF spectrum containing scattered Sn particles, together with the corresponding SRIM simulations. The shape of the measured ToF spectrum is in good agreement with SRIM except for the SC peak near 7 μs. Furthermore, the double peak structure near 6 and 6.5 μs is not reproduced by SRIM red which does not predict an increased intensity at 6.5 μs. The ToF measurements have a higher yield for flight times around 5 μs, which is a remnant of the long-ToF tail of the O-recoil peak (cf. figure 2.8). For flight times longer than 7 μs the ToF yield is in good agreement with the SRIM simulations, while for the pure ion distribution measured with the ESA (see figure 2.7) a significantly lower yield was measured for lower energies. This appears indicative of the fact that at lower energies backscattered tin particles are less likely to be (re-)ionized on the way out of the target.

The 6.5-μs peak corresponds to energy for Sn of roughly 8 keV in the energy domain. At this time and energy, both the ToF and the ESA measurements show a small peak, slightly higher than the yield in the SRIM predictions. Incidentally, the energy of

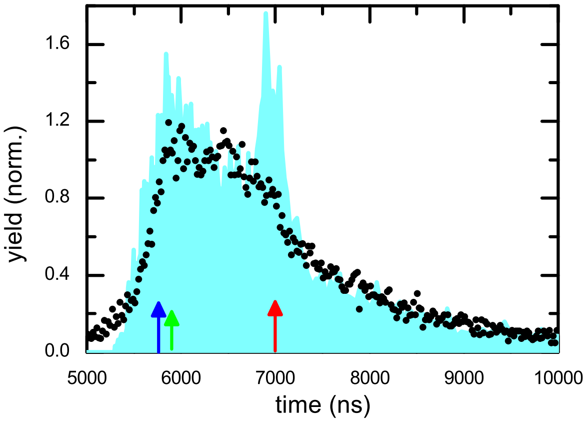

Figure 2.9: *Comparison of the part of the measured ToF spectrum (black symbols) containing Sn particles and the corresponding SRIM predictions (blue area) for 14 keV Sn^{2+} ions on a Ru target at a scattering geometry of (ψ,θ) = (15,40).*

primary ruthenium recoils at 40° is also 8 keV. However, the ToF of Ru recoils is $\sim$ 6 μs and thus Ru recoils are blended in the double/ multiple peak. This complicates a detailed assessment of the contribution of Ru recoils to the spectrum, but it indicates that the 6.5-μs peak and thus the small 8-keV peak in the ion spectrum is due to Sn ions.

In conclusion, ToF spectra of neutral scattered tin particles do not show a single-collision peak just as the ion spectra. Therefore the absence of the single scattering peak is not due to exceptional ratios of scattered ions and neutrals.

2.3.5 SRIM approaches

The SRIM package allows one to select one out of three different calculation methods most relevant to our scattering geometries: *monolayer collision steps/surface sputtering*, *detailed calculation*, and *quick calculation*. We used the *monolayer collision steps/surface sputtering* option, which is recommended for near-surface interactions. In figure 2.10, the predictions for a (ψ,θ) = (15,30) scattering geometry for 14 keV Sn ions incident on Mo are shown for the three methods of calculation. The results are basically the same. The single scattering peak is present for all three methods and has approximately the same height though it appears to be slightly broader for the quick calculation. Thus the single-scattering peak persists independent of the calculation method.

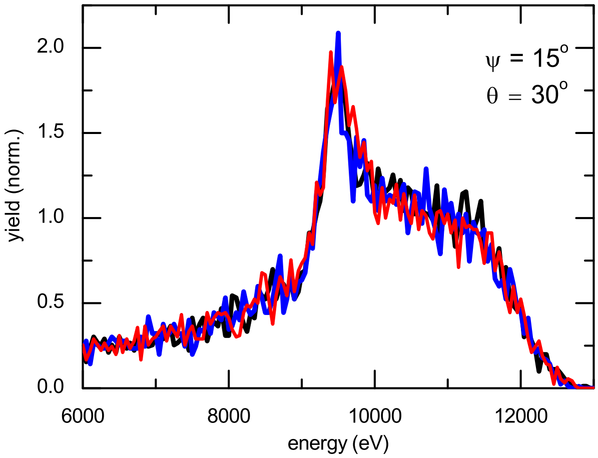

Figure 2.10: *Direct comparison of the SRIM predictions for a 14 keV Sn beam on molybdenum for (ψ,θ) is (15,30) for three different calculation methods: monolayer sputtering (black), detailed calculation (blue), and quick calculation (red).*

In SRIM the location of subsequent collisions is determined by a mean free path length d of the incoming projectile and d is taken to be equal to the inverse cubic root of the atom density $N : d = N^{-1/3}$. For example, for Ru d is thus fixed at 0.24 nm. The projectile's trajectory calculation starts at the surface. This implies that (pre-)scattering above the surface layer and along the initial part of its trajectory into the surface up to the point of the first binary encounter is neglected. The first collision takes place at a distance d away from the point where the particle entered the surface. The particle is declared backscattered if it is scattered in such a way that it is moving towards the edge of the surface and the next point of collision, at a distance d, would be placed somewhere above the surface. For single scattering, this is only possible if the outgoing angle of the projectile, with respect to the target surface, is larger than the incoming angle. Otherwise, the particle is forced to have another collision, thereby inhibiting the occurrence of a single-collision peak at scattering angles θ between ψ and 2ψ. Thus, for scattering angles $\theta < 2\psi$, the absence of the SC peak in the SRIM results is purely stemming from the calculation algorithm and should not be taken as SRIM being in agreement with the experiments.

Can the neglect of pre-scattering and taking the first binary interaction to occur inside the surface explain why a SC peak shows up in the simulations but not in the experiments? A priori there is no obvious reason why single collisions should not happen. The absence of a clear single-collision peak in the experiments must therefore rest on a significant broadening and shift of the SC peak such that it can not be resolved separately anymore, i.e., only a negligibly small fraction of the incoming ions is truly in one single collision scattered over the chosen scattering angle. On its way towards the surface, the ion may undergo small angle deflection(s), pre-scattering, which is always scattering towards the detector. Thus a smaller scattering angle suffices to obtain the same total scattering angle as for a single scattering process, leading to higher energies for the scattered ions. Post-scattering on the trajectory out off and away from the surface will also broaden the energy distribution. As there are many pathways with many potential final energies, the energy distribution may become very broad for these quasi-single scattered ions. For example, for a 14 keV Sn ion and a set scattering angle of 45°, a 1° smaller or larger scattering angle already results in an energy broadening of ±0.35 keV. Releasing the fixed distance of consecutive collisions and the first collision with respect to the surface will also lead to an energy broadening. Different trajectory lengths do experience different electronic energy losses.

Previous research [25] focusing on grazing incidence studies found large effects of pre-scattering leading to the conclusion that for small, grazing incidence angles SRIM would benefit from inclusive treatment of the above surface interactions. Our work at larger incidence angles hints at a similar shortcoming. In addition, for the present low-energy heavy particle scattering on a transition metal, a dedicated inspection of the appropriateness of the generic ZBL potential might be in order since such collision systems were barely available for inclusion in the determination of the ZBL potential.

2.4 Conclusions

In modern EUV sources, based on laser-produced tin plasma, tin ions coming from the LPP plasma can interact with the surrounding walls and optical elements. The interaction between the tin ions and a surface can be investigated by the use of SRIM, a widely-used simulation package. A thorough systematic investigation of the accuracy of the simulation package, when applied to the impact of slow heavy ions on transition metals, is however lacking. We present the results of keV tin ion backscattering on a Mo target and compared the energy distributions with the predictions of SRIM.

The experimental energy distributions are in agreement with the simulations, except for a significant peak in SRIM which is associated with a single collision in the upper layer of the target. This peak is not visible in the experiments. By performing a series of experiments in which the energy and charge state of the tin ions is changed, different species and targets are used, the possibility of this being a charge state-specific or energy effect, or only appearing for a specific projectile ion and/or target surface is excluded. Additional ToF measurements, which measures mainly scattered atoms instead of ions, lead to the same conclusion. The reason that the single scattering peak remains to show up in SRIM is probably due to ignoring any interaction above the surface and the fixed distance between consecutive collisions. The inclusion of surface interactions and variable distance between subsequent collisions might broaden the energy distributions so much that the single-collisions peak gets washed out. Moreover, the appropriateness of the generic ZBL potential to low-energy heavy particle scattering on a transition metal should be tested by extending the range of collision energies and including the assessment of sputter yields and target recoils. The agreement of the multiple collision part of the energy distribution with the simulations shows that the ion-target interactions well inside the surface are properly simulated by SRIM. For low kinetic energies, i.e., the bulk of ions coming from the laser-produced plasma, the ions penetrate into the topmost atomic layer(s) only and thus surface interactions are most relevant. It is just these interactions that are not that well-simulated by SRIM. Simulation packages with improved models are necessary to predict the complex interactions of low-energy ($\leq$ 1 keV/u) heavy particles colliding on surfaces.

2.5 Acknowledgment

This work was carried out at the ZERNIKELEIF facility at the Zernike Institute for Advanced Materials of the University of Groningen as part of the research portfolio of the Advanced Research Center for Nanolithography, a public-private partnership between the University of Amsterdam, the Vrije Universiteit Amsterdam, the Netherlands Organization for Scientific Research (NWO), and the semiconductor equipment manufacturer ASML

Bibliography

[1] V.Y. Banine, K.N. Koshelev, G.H.P.M. Swinkels, J. Phys. D: Appl. Phys., **44**, 253001 (2011).

[2] O.O. Versolato, Plasma Sources Sci. Technol. **28**, 083001 (2019).

[3] F. Torretti, J. Sheil, R. Schupp, M. Basko, M. Bayraktar, R. Meijer, S. Witte, W. Ubachs, R. Hoekstra, O.O. Versolato, A. Neukirch, and J. Colgan, Nat. Comm. in press (2020).

[4] N.R. Böwering, A.I. Ershov, W.F. Marx, O.V. Khodykin, B.A.M. Hansson, E. Vargas L, J.A. Chavez, I.V. Fomenkov, D.W. Myers, D.C. Brandt, Proc. of SPIE, **6151**, 61513R (2006).

[5] S. Bajt, J.B. Alameda, T.W. Barbee, W.M. Clift, J.A. Folta, B.B. Kaufmann, E.A. Spiller, Opt. Eng., **41**, 1797 (2002).

[6] H.N. Chapman, N. Nguyen, J. Alameda, J.C. Robinson, M. Malinowski, E. Gullikson, A. Aquila, C. Tarrio, and S. Grantham, Appl. Opt., **42**, 5750 (2003).

[7] Q. Huang, V. Medvedev, R. van de Kuijs, A. Yakshin, E. Louis, F. Bijkerk, Appl. Phys. Rev., **4**, 011104 (2017).

[8] A. Dolgov, C.J. Lee, F. Bijkerk, A. Abrikosov, V.M. Krivtsun, D. Lopaev, O. Yakushev, and M. van Kampen, J. Appl. Phys., **123**, 153301 (2018).

[9] A. Bayerle, M.J.Deuzeman, S. van der Heijden, D. Kurilovich, T. de Faria Pinto, A. Stodolna, S. Witte, K.S.E. Eikema, W. Ubachs, R. Hoekstra, O.O. Versolato, Plasma Sources Sci. Technol., **27**, 045001 (2018).

[10] M. J. Deuzeman, A. S. Stodolna, E. E. B. Leerssen, A. Antoncecchi, N. Spook, T. Kleijntjens, J. Versluis, S. Witte, K. S. E. Eikema, W. Ubachs, R. Hoekstra, O. O. Versolato, J. Appl. Phys., **121**, 103301 (2017).

[11] W. Möller, W. Eckstein, Nucl. Instrum. Methods Phys. Res. B, **2**, 814 (1984).

[12] A. Mutzke, R. Schneider, W. Eckstein, R. Dohmen, IPP-Report **12/8** (2011).

[13] J.F. Ziegler, J.P. Biersack, U. Littmark, *The Stopping and Range of Ions in Solids*, Pergamon Press, New York, 1985.

[14] J.F. Ziegler, M.D. Ziegler, J.P. Biersack, Nucl. Instrum. Methods Phys. Res. B, **268**, 1818 (2010).

[15] M. P. Seah and T. S. Nunney, J. Phys. D: Appl. Phys., **43** 253001 (2010).

[16] H. Hofsäss, K. Zhang, Nucl. Instrum. Methods Phys. Res. B, **267**, 2731 (2009).

[17] K. Wittmaack, J. Appl. Phys., **96**, 2632 (2004).

[18] V.I. Shulga, Appl. Surf. Sci., **439**, 456 (2018).

[19] P.S. Szabo, R. Chiba, H. Biber, R. Stadlmayr, B.M. Berger, D. Mayer, A. Mutzke, M. Doppler, M. Sauer, J. Appenroth, J. Fleig, A. Foelske-Schmitz, H. Hutter, K. Mezger, H. Lammer, A. Galli, P. Wurz, F. Aumayr, Icarus **314**, 98 (2018).

[20] H. Paul, Nucl. Instrum. Methods Phys. Res. B, **247**, 166 (2006).

[21] P. Filliatre, C. Jammes, B. Geslot, Nucl. Instrum. Methods Phys. Res. A, **618**, 294 (2010).

[22] K.N. Yu, C.W.Y. Yip, D. Nikezic, J.P.Y. Ho, V.S.Y. Koo, Appl. Radiat. Isot., **59**, 363 (2003).

[23] J.P.J. Dubois, K. Achkasov, D. Kogut, A. Ahmad, J.M. Layet, A. Simonin, G. Cartry, J. Appl. Phys., **119**, 93301 (2016).

[24] M. Jurado Vargas, A. Fernández Timón, J. Radioanal. Nucl. Chem., **305**, 479 (2015).

[25] N.V. Novikov, Y.A. Teplova, Y.A. Fainberg, V.S. Kulikauskas, Nucl. Instrum. Methods Phys. Res. B, **235**, 48 (2005).

[26] L.C. Feldman, J.W. Mayer, *Fundamentals of surface and thin film analysis*, Elsevier Science Publishing Co, New York, 1986;

[27] G. Lubinski, Z. Juhàsz, R. Morgenstern, R. Hoekstra, J. Phys. B: At. Mol. Opt. Phys. **33**, 5275 (2000).

[28] E. Bodewits, H.M. Dang, A.J. de Nijs, D.F.A. Winters, R. Hoekstra, Nucl. Instrum. Methods Phys. Res. B, **267**, 594 (2009).

[29] M.V. Tiba, W.J.M. de Jong, B. Koopmans, and H.T. Jonkman, J. Appl. Phys., **100**, 093707 (2006).

[30] Q. Yan, D.M. Zehner, F.W. Meyer, S. Schippers, Phys. Rev. A, **54**, 0641 (1996).

[31] H. Winter, Phys. Rep., **367**, 387 (2001)

[32] S. Schippers, L. Folkerts, Surf. Sci. **257**, 289 (1991).

[33] H. Hofsäss, K. Zhang, A. Mutzke, Appl. Surf. Sci., **310**, 134 (2014).

[34] K. Wittmaack, Nucl. Instrum. Methods Phys. Res. B, **380**, 57 (2016).

Chapter 3

Single-collision scattering of keV-energy Kr ions off a polycrystalline Cu surface

Abstract

In the keV-energy regime, the scattering of krypton ions off a copper sample has been studied. In addition to the broad energy spectrum arising from multiple-collision scattering, the energy distributions of the backscattered ions exhibit prominent peaks at energies where single-collision (SC) scattering peaks are expected. Such SC peaks were shown to be absent in Sn - Mo/Ru scattering, systems of similar mass ratio, and thus similar kinetics. The present Kr on Cu results allows for a comparison to a simulation package as SRIM. An important difference found between the present experiment and the predictions of SRIM is that the SC contribution is observed to decrease with scattering angle, whereas SRIM predicts this contribution to be constant. The intensity of the experimental SC peaks, though much weaker than in the SRIM simulations, may be used as markers to improve SRIM in its description of low-energy heavy particle scattering off surfaces.

3.1 Introduction

In a recent systematic study, [1] of the scattering of keV-energy tin ions from Mo and Ru, materials commonly used in extreme ultraviolet (EUV) optics [2, 3], a remarkable observation made was the absence of a single-collision (SC) peak in the energy spectra of the scattered ions. Unlike the experiments, the most widely used package to simulate ion-matter interactions SRIM [4–6] consistently predicted a prominent SC peak on top of the broad distribution of multiple-scattering events. The width and the high-energy shoulder of the multiple-collision feature were found in agreement

---

Chapter published: S. Rai, K.I. Bijlsma, S. Koeleman, O.G. Tjepkema, A.W. Noordam, H.T. Jonkman, O.O. Versolato and R. Hoekstra, *Single-collision scattering of keV-energy Kr ions off a polycrystalline Cu surface*, Nucl. Instrum. Methods Phys. Res. B **482**, 58 (2020).

with the experiments. A series of tests in which the charge state and energy of the incoming Sn ions were changed and the Sn ions replaced by Xe ions, were conducted to investigate this discrepancy. The results led to the conclusion that most likely the SC peak prominently showing up in the SRIM predictions in contrast to the experiments is due to SRIM-related causes such as ignoring any interaction above the surface and using a fixed distance between consecutive collisions. And, perhaps the binary collision approximation underlying SRIM might not be valid anymore for low-energy heavy particle scattering on heavy targets. In any kind of binary-collision approximation, one expects a SC signature to show up in the energy spectra of scattered particles. A complicating factor in a direct comparison between experiment and SRIM is that SRIM treats all particles as neutral, while experimentally it is most convenient to use ionic beams and to detect scattered charged particles and their energies by means of electrostatic analyzers. Ideally one would like to know the ion and neutral fractions, which are however ill-known and depend on energy and surface characteristics. Therefore, Time of Flight (ToF) measurements were performed in which both ions and neutrals are detected [1]. The ToF measurements at a fixed angle supported the finding in the ion spectra that no clear SC peak is detected in the energy spectra of the scattered Sn particles.

Here, we present our follow-up research on the scattering of keV Kr^+ ions from a polycrystalline Cu sample. We based our choice for the Kr on Cu system on the following arguments. First of all, we looked for a collision system with similar single-collision kinetics i.e., similar relative final energy distributions as a function of scattering angle. Within a binary collision approximation, the kinetics is governed by the ratio of the target and projectile masses. For Mo or Ru as target and Sn as a projectile, the mass ratio is ≈ 0.8. Knowing that for light ion scattering SRIM appears to describe the scattering well, an intermediate-mass collision system seemed appropriate. From the experimental perspective of ion beam production, a noble gas is preferred. Therefore the choice was made to use Kr as a projectile and with Cu as a target, a similar mass ratio of ≈ 0.8 is achieved. As will be shown in this paper, in contrast to the case of Sn ion scattering on Mo or Ru, SC peaks do show up in the energy spectra of Kr ions scattered off Cu. This allows us to compare experimental binary collision strengths with ones predicted by the SRIM code as a function of scattering angle. This is not possible for the Sn interactions on Mo and Ru as the single-collision peak is absent in the experimental data. The present experimental data on Kr on Cu scattering may assist in improving the SRIM code and evaluating its accuracy in simulating low-energy ion-surface interactions. An improved version of the code will be useful in accurately simulating and predicting the outcome of collisions of Sn ions on Ru-capped multilayer Mo/Si collector mirrors used to collect EUV light used in state-of-the-art nanolithography tools [7, 8]. The EUV light is generated by a tin plasma produced by laser irradiation of a stream of molten Sn microdroplets. Unavoidable by-products of such a plasma are fast Sn ions, e.g. [9], which may impact the EUV collector mirrors and reduce collector-mirror lifetime in EUV light sources.

3.2 Experimental methods

The Kr ion beam is extracted from a SUPERNANOGAN-type electron cyclotron resonance ion source. By means of a 110° analyzing magnet a beam of isotopically pure $^{84}\mathrm{Kr}^{+}$ ions is selected and transported to the collision chamber via a series of three magnetic quadrupole triplets and a 45° dipole magnet in front of the setup for final mass-over-charge clean-up of the beam [1]. Since details of the setup can be found elsewhere e.g., [10–12] only the parts of direct relevance to the present scattering experiments will be recalled briefly. The polycrystalline Cu target is mounted on a high precision manipulator allowing for the adjustment of the angle of incidence (ψ), measured with respect to the surface. In all the experiments a fixed incidence angle of 15° is used.

The kinetic-energy spectra of Kr ions are recorded at scattering angles (θ) ranging from 20° to 40° by means of a rotatable, high-precision electrostatic analyzer (ESA) with an opening angle of about 0.3°. The target used in this work is polycrystalline Cu, prepared by Surface Preparation Lab (SPL). ESA spectra as for example shown in figure 3.1 are built up out of a series of kinetic energy scans. For each energy point, the beam current on the target is recorded. The typical beam current was 50 nA. Beam fluctuations affect the spectra hence the number of counts per second is divided by the accumulated beam current. Furthermore, because the ESA is operated in fixed $\Delta E/E$ mode the data is corrected for the changing energy-bin width ΔE, by dividing the yield by ΔE. Thereafter, as the final correction step, the data is corrected for the energy-dependent detection efficiency of the micro-channel plate [13] used to detect the scattered Kr ions.

For comparison to and interpretation of the experimental data, SRIM simulations have been performed. As a calculation method, we used the *Monolayer Collision Steps / Surface Sputtering* option of SRIM, which is recommended for ion interactions near the surface [4], although as shown by Deuzeman [1] the differences between the different calculation methods offered by SRIM are very small. For comparison to the experiments, the backscattered particles are required to be in the plane defined by the ion beam and the detector plane within an angular width of 3°. Concerning the in-plane angular acceptance, only particles that are within 1° of a chosen scattering angle are counted. These acceptance angles are larger than the actual ones of the

ESA (0.3°). The code was run with the same ^{84}Kr isotope as used in the experiments. For the target sample, a mixture of ^{63}Cu and ^{65}Cu isotopes is used in accordance with their natural abundances of 31 and 69%. To obtain sufficient statistics 46.5×10^6 trajectories were calculated in eight batches, each of which used a different random number seed.

Following the binary collision approximation, it is derived that a single collision between a projectile of mass m_p with kinetic energy E_0 and a target atom of mass m_t leading to scattering over an angle θ results in final energy of the scattered projectile E_f given by [14]

$$\frac{E_f}{E_0} = \left(\frac{\cos(\theta) + \sqrt{(m_t/m_p)^2 - \sin^2(\theta)}}{1 + m_t/m_p} \right)^2 . \tag{3.1}$$

Apart from the scattered projectiles recoiled target ions may also end up in the spectra upon a single collision, at an energy of

$$\frac{E_{rec}}{E_0} = \frac{4 m_t m_p}{(m_t + m_p)^2} \cos^2(\theta). \tag{3.2}$$

In the energy spectra of scattered ions, we indicate the positions of these SC scattering and recoil energies with red and green arrows, respectively. Instead of via a single collision, an ion can also scatter over a certain angle θ via two consecutive collisions. A special case is a symmetric double collision (SDC), i.e. two consecutive collisions over a scattering angle of $\theta/2$. The final energy of such a particle is also denoted in the spectra, with a blue arrow. The energy of the SDC marks the maximum energy which can be attained in a double-collision, all other (asymmetric) double collisions lead to energies in between the SC and SDC energies.

3.3 Results and discussion

Figure 3.1 shows a typical set of energy distributions of 7 keV Kr$^+$ scattering off a Cu target. As mentioned in the introduction, in the scattered ion spectra of keV-energy Sn ions impinging on Mo and Ru, the SC peaks were absent. However now for Kr$^+$ on Cu, as figure 3.1 shows, a clear presence of prominent SC peaks is observed. It can also be seen that the energy of SDC is a fair indication of the maximum energy of scattered projectiles.

In the energy spectra (cf. figure 3.1) a small shift between the calculated SC peak positions and the measured energies is noted that hints at an offset of 1.1° in the angular position of the ESA. Image charge attraction on the incoming and outgoing trajectories of the ions can at most explain approximately 0.2°, therefore the shift is most likely due to a small 1° offset in the zero-degree calibration of the ESA. In the following, scattering angles are corrected for this 1° offset.

Contributions of Cu recoils to the spectra appear to show up in spectra. However, these contributions appear weak and as such do not contribute significantly to the total yield of measured ions. Therefore, they will not be considered separately in the further discussion on the contribution of single-collision scattering to the total yield of backscattered ions.

Similar to figure 3.1, figure 3.2 shows energy spectra of backscattered particles resulting from an SRIM simulation of 46.5 million 7 keV Kr particles impinging on Cu under an incidence angle ψ of 15°. It shows clearly that for scattering angles equal to or exceeding twice the incidence angle a prominent SC peak is present in the synthetic energy spectra. In comparison to the experimental data depicted in

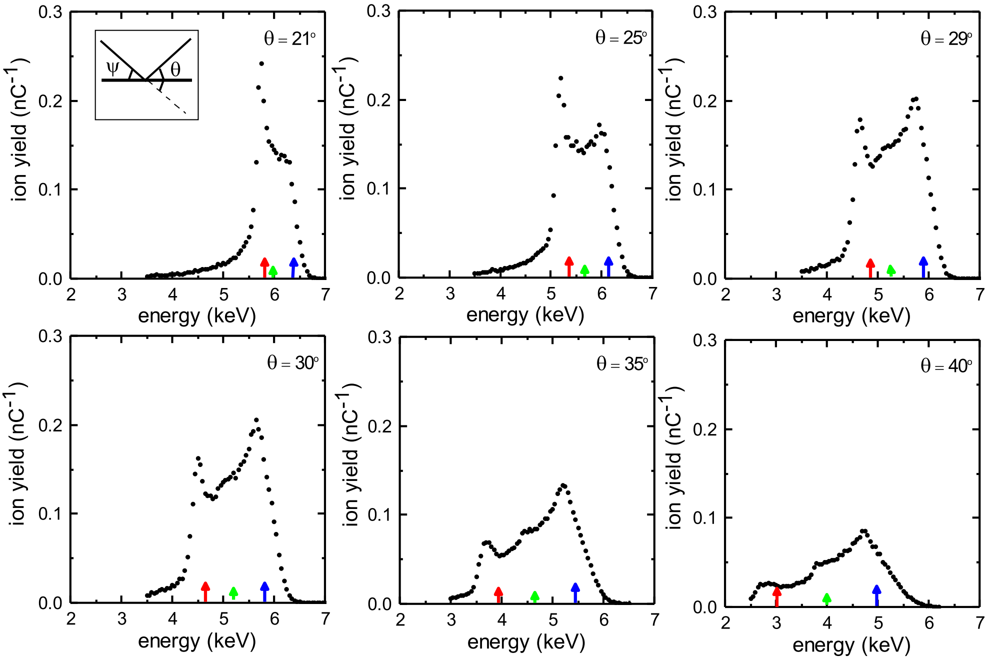

Figure 3.1: *Compilation of energy spectra of scattered 7 keV Kr$^+$ ions incident on a Cu target at an incidence angle ψ of 15°; the different plots show the spectrum for different scattering angles θ. The energy positions of single and symmetric double scattering are marked by red and blue arrows, respectively. The green arrows indicate the energy of primary Cu recoils.*

figure 3.1 the calculated SC features are much stronger. The SC peak is absent in the SRIM spectra for scattering angles smaller than 30°. This is a known flaw of SRIM stemming from taking a fixed distance between consecutive collisions [1, 15]. As is illustrated in the inset of the top-left panel, the first collision in SRIM takes place at a distance d (the mean free path) away from the point where the particle entered the surface. The particle is marked backscattered if it is scattered towards the surface and the subsequent point of collision, at a distance d, would be above the surface. For single-collision scattering, this is only possible if the outgoing angle of the projectile, with respect to the target surface, is larger than the incoming angle. Otherwise, the particle is forced to undergo a second collision, thereby inhibiting the occurrence of a SC peak at scattering angles below 2ψ. Therefore, a comparison of experimental and SRIM results regarding SC peak intensities is limited to scattering angles $\theta > 30°$.

Figure 3.3 shows the yield of single-collision scattering as a function of scattering

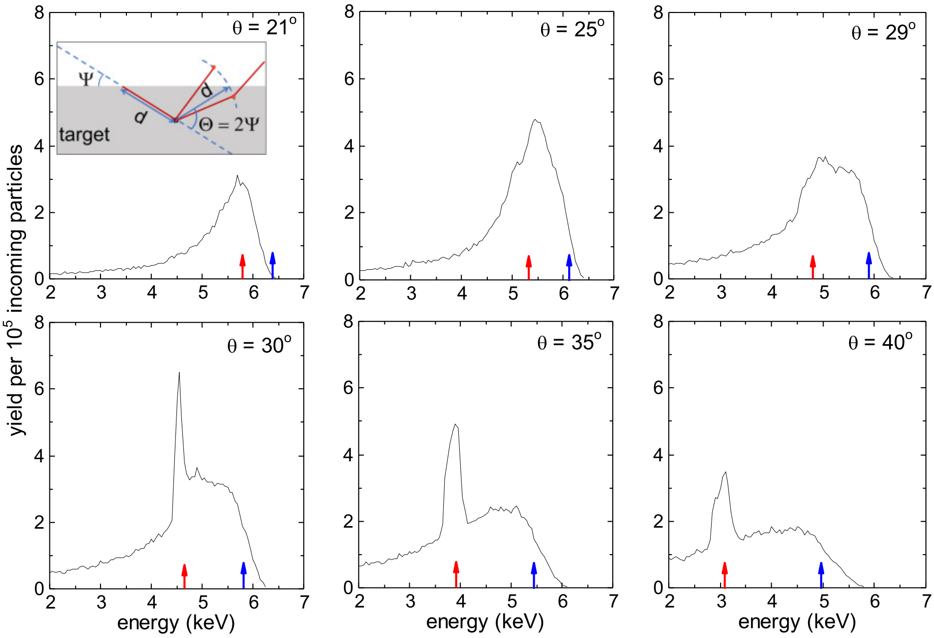

Figure 3.2: *Compilation of scattered energy distributions as simulated by SRIM for 7 keV Kr impinging on Cu at an incidence angle ψ of 15°; the different plots show the spectrum for different scattering angles θ. The energy positions of single and symmetric double scattering are marked by red and blue arrows, respectively. The inset shows a schematic explaining why single-collision scattering cannot occur in SRIM for scattering angles $\theta < 2\psi$.*

angle, obtained from the experimental data as well as from the SRIM simulations. These SC ion yields are determined by assuming a linear background of multiple scattering events underlying the SC peak, as shown in the inset. The uncertainties in the experimental SC yields are assessed by taking realistic upper and lower linear backgrounds. The data from the SRIM simulation are scaled to the data point at 31° because SRIM does not consider the charge state of the particles and thus the SRIM spectra can not be separated into individual ion and neutral contributions. The angular dependency predicted by SRIM is in good agreement with the experimental data. As can be seen, the SC ion yield is bell-shaped with its maximum at 30°.

Independent of the exact form of the interaction potential, for a two-body single collision, one expects the SC yield to increase towards smaller scattering angles, because of the increasing cross sections for smaller scattering angles [14, 17]. However, in the experimental SC yield, we see an opposite trend for angles smaller than 30°, the SC intensity decreases. It is to be realized that we solely measure the *ionic* SC yield. The lower SC yields at smaller scattering angles might be driven by a lower fraction of scattered ions. For smaller scattering angles, on the outgoing trajectory, the ions' velocity normal to the surface is lower and thus the time an ion needs to travel through the surface's selvedge becomes longer. This reduces the probability to escape from the surface as an ion, therefore ion fractions become smaller at lower scattering angles [16]. In addition, contributions to the SC peak from single-

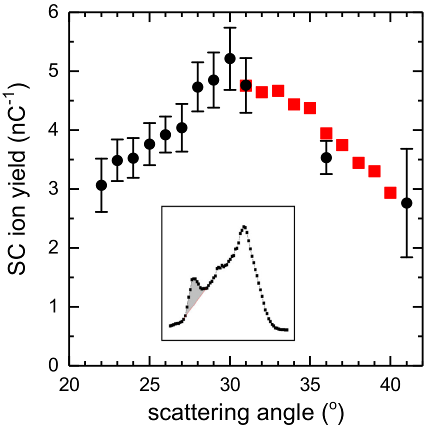

Figure 3.3: *Scattering-angle dependence of the single-collision ion yield (black symbols) for 7 keV Kr$^+$ ions on Cu at an incidence angle ψ of 15°. The closed red squares indicate yields obtained from SRIM (scaled at 31°). The inset shows how the SC yield is determined: by integrating the shaded area under the SC peak in the energy spectrum.*

scattering off the second (and third, ...) topmost layers will get less at smaller scattering angles as the probability for the particle to escape from the target without undergoing a second collision becomes smaller. The latter process is included in the SRIM simulations. Therefore in a comparison between SRIM and experimental results the particle-escape probability is included while the electronic processes are not. Unfortunately, such a comparison for the SC yields is hampered by the fact that SRIM does not predict a SC peak at angles below 30°. Given that pure SC events mainly arise from the topmost layer, it is expected that changes in the ion fraction are more important than the changes in the particle-escape probabilities.

That expectation of significantly lower ion fractions at smaller scattering angles finds support in the trends observed in the total experimental ion yields depicted in figure 3.4. For scattering angles down from 30°, where the SC yield decreases by some 40% (see figure 3.3) the total scattered ion yield drops by a factor of 4. Therefore, the contribution of the SC peak to the ion spectrum increases rapidly toward smaller scattering angles.

To get some information on to what extent the drop in the total ion yield is due to changing ion fraction and not an overall reduction of the number of backscattered particles at scattering angles below 30°, a comparison is made to the total yields

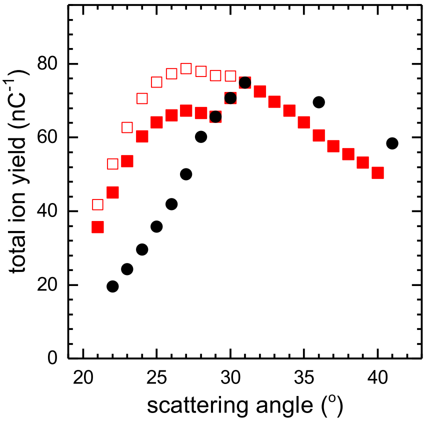

Figure 3.4: *Scattering-angle dependence of measured total ion yields (black symbols) for 7 keV Kr$^+$ ions on Cu at an incidence angle ψ of 15°. The closed red squares indicate total scattering yields obtained from SRIM (scaled at 31°), which at angles below 30° lack contributions from SC events. The open red squares show the SRIM data after correction for the missing SC events at angles below 30°. The correction is based on assuming a constant SC fraction (see Figure 3.5).*

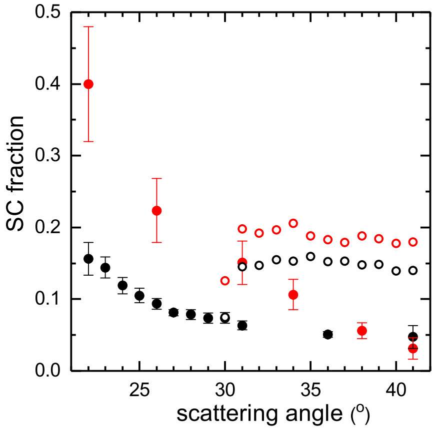

Figure 3.5: *Single-collision fractions of 7 (black) and 5 (red) keV Kr$^+$ impinging on Cu at an incidence angle ψ of 15°. The closed and open symbols represent the data from the experiment and SRIM, respectively.*

predicted by SRIM. As can be seen from figure 3.4 the total yields obtained from the SRIM simulations show a significant reduction in their yields only for scattering angles below 24°. Based on small changes in the SRIM yields of tens of percent one may conclude that the reduction in the measured, total ion yields of a factor of 4 is by and large due to decreasing ion fractions.

A remarkable and noteworthy feature in the angular dependence of SRIM's total yield is an abrupt kink at 30°. This kink is likely due to the absence of a SC peak below 30° in the SRIM results. The SRIM yields in this angular range can be corrected for a missing SC contribution by extrapolating the SC fraction at angles larger than 30°. The SC fractions, which are calculated by dividing SC yields by total ion yields, are depicted in Figure 3.5. The figure demonstrates that for angles larger than 30° SRIM predicts for 7 keV Kr an almost constant SC fraction (SCF) of approximately 0.15. Assuming that below 30° SRIM only misses out on the SC events, we have corrected the SRIM data in figure 3.4 for a missing SCF of 0.15 by multiplying the SRIM data by the factor 1/(1 - SCF). The SRIM data point at 30° is corrected for missing a SCF of 0.075 since we binned the SRIM data in angular bins of ±1°. This implies that half of the bin size is above 30° while the other half falls below 30°, so only for the latter half the correction is needed. Correcting the SRIM data in this manner fully removes the kink in the SRIM yields near 30° and nicely smoothens the SRIM data as a function of scattering angle.

The fact that SRIM predicts a constant SC fraction is a priori not expected since the largest part of the total yield is due to a variety of multiple-collision events of which many occur along longer trajectories through the target exposing them to additional energy loss by straggling. It seems thus unlikely that this wide ensemble of scattering events would have the same angular dependence as the single-collision events leading to the SC peak. For 7 keV Kr^+ ions the experimental data (see figure 3.5) do not exclude the SC fraction to be almost constant at scattering angles above 30°, though the experimental values are a factor of three smaller than the SRIM ones.

Next to the 7 keV experiments, we have performed some experiments at a lower energy of 5 keV Kr^+ ions which are shown in the same figure 3.5. The larger uncertainty associated with this 5-keV data is due to a much lower count rate, which is in line with a lower ionization fraction at lower velocities. Notwithstanding the larger uncertainties, the 5-keV data clearly shows a SC fraction that is not constant with angle, in contradiction with what SRIM predicts. At the smaller scattering angles, the SC fraction at 5 keV is about a factor of 2 larger than for 7 keV. In the SRIM simulations, the difference between 5 and 7 keV Kr ions is much smaller than in the experimental data, namely only 30%.

To verify whether SC scattering might be more prominent in the neutrals, a Time of Flight (ToF) measurement, which detects neutrals and ions alike, was performed at a scattering angle of 40° for 5 keV Kr^+ ions. The measured ToF spectrum is depicted in figure 3.6. The figure shows no clear sign of a SC peak (red arrow position). Therefore, the SC fraction is very small, which is in line with the small SC fraction of $\sim$3% observed in the ionic measurements (cf. figure 3.5). Therefore the ToF data confirm the conclusion drawn from the ion data that there is a considerable difference (factor of ~ 3) between the experiment and SRIM in the strength of the SC peak. Therefore, concerning the SC peak, there is no appreciable difference between the energy spectra of ions and neutrals and thus the ion data can be considered to be representative of the scattering of Kr ions from Cu.

Along with the ToF spectrum, the prediction of SRIM is also plotted in figure 3.6. The overall shape of the ToF spectrum simulated by SRIM is in good agreement with our experimental data except for the strong SC peak around 10.3 μs which is absent in the measurements. In addition, it is noted that at shorter flight times around 7 to 8 μs, the ToF measurements show a gradual increase in intensity while SRIM predicts a steep rise from 7.6 μs on. The intensity below 8 μs stems from the contribution of primary Cu recoils to the ToF spectrum and not from fast Kr particles. As the ESA measurements of the kinetic energies of the ions are not sensitive to the mass of the ions, the Cu recoils will end up in between the SC and SDC energies in the ESA spectrum (see e.g. figure 3.1). Conversion of the ESA spectrum to ToF, assuming all ions to be Kr ions, should not exhibit any intensity at the shortest flight times. Therefore

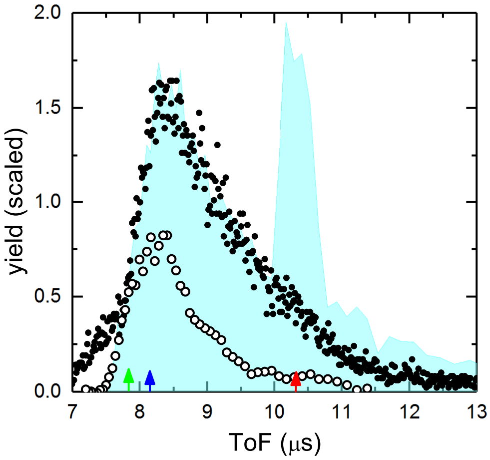

Figure 3.6: *Comparison of the experimental ToF spectrum (closed black symbols) of backscattered particles (ions and neutrals) and the SRIM predictions (cyan) for 5 keV Kr$^+$ ions on a Cu target at a scattering geometry of (ψ, θ) = (15°, 40°). The open black symbols represent the measured ion energy spectrum converted to time scale. The ToF positions of single and symmetric double scattering are marked by red and blue arrows, respectively. The green arrow indicates the position of primary Cu recoils in the ToF spectrum.*

to verify the assignment of primary Cu recoils in the ToF spectrum in figure 3.6 we have added the results of an ESA measurement after converting the data from energy to time scale. The ESA spectrum is visually scaled to overlap SRIM and ToF spectrum at shorter flight times. It shows the same steep increase at shorter flight times as in the SRIM simulations, thereby it underlines the assignment of the ToF spectrum at the flight times below 8 μs to primary Cu recoils.

A further comparison of the shapes of the direct and converted ToF spectra indicates that beyond 8.5 μs the yields from the converted ESA spectrum drop faster than in the direct ToF measurements. This is another indication that at lower kinetic energies the ion fractions get lower. Therefore, a quantitative comparison of ion spectra to SRIM simulations requires accurate knowledge on ion fractions. However, as shown here by the comparison of the ESA (ions only) and ToF (neutrals and ions) spectra, not knowing the exact ion fraction does not inhibit one to draw conclusions on the presence or absence of the single-collision peak in the spectra.

3.4 Conclusions

The scattering of Kr ions off a Cu sample has been studied by means of ion scattering spectroscopy at incoming energies of 7 and 5 keV. The mass ratio of Cu and Kr (≈ 0.8) is similar to that of Mo (or Ru) to Sn. Therefore, within a binary collision approximation, the kinetics of single scattering is the same for Kr-Cu as it is for Sn-Mo. While for Sn ion scattering on Mo no single-collision (SC) peaks show up in the energy distribution of scattered ions, in the present study we find that they do for the lighter system of Kr ions on Cu. The presence of SC peaks and their angular dependence hints at the binary collision approximation being a viable approximation. The measured SC peaks decrease in intensity with increasing scattering angle. SRIM does not predict a SC contribution to the spectra at scattering angles smaller than twice the incoming angle, which is an imperfection of the code's algorithm for calculating subsequent binary collisions. For larger scattering angles SRIM predicts that the contribution of the SC peak to the spectra is constant at about 15%. However, at those larger scattering angles, the measured SC peaks continue to decrease and are weaker than predicted by SRIM by a factor of three. The measured angular dependence of the single-collision peaks, which is a signature of the scattering potential, could serve as a guide with which one can adjust SRIM to improve its description of low-energy heavy particle scattering off surfaces. For example, the generic ZBL-potential used by SRIM [4, 5], which is based on the full range of energies and masses, might not be most suitable for such systems. An optimized potential could also be of benefit to the modeling of Sn ion collisions on Ru capping layers of EUV collecting mirrors in modern nanolithography tools.

3.5 Acknowledgment

This work was carried out at the ZERNIKELEIF facility at the Zernike Institute for Advanced Materials of the University of Groningen as part of the research portfolio of the Advanced Research Center for Nanolithography, a public-private partnership between the University of Amsterdam, the Vrije Universiteit Amsterdam, the Netherlands Organization for Scientific Research (NWO), and the semiconductor equipment manufacturer ASML.

Bibliography

[1] M.J. Deuzeman, *PhD thesis*, University of Groningen (2019).

[2] S. Bajt, J.B. Alameda, T.W. Barbee, W.M. Clift, J.A. Folta, B.B. Kaufmann, E.A. Spiller, Opt. Eng., **41**, 1797 (2002).

[3] Q. Huang, V. Medvedev, R. van de Kuijs, A. Yakshin, E. Louis, F. Bijkerk, Appl. Phys. Rev., **4**, 011104 (2017).

[4] J.F. Ziegler, J.P. Biersack, U. Littmark, *The Stopping and Range of Ions in Solids*, Pergamon Press, New York, 1985.

[5] J. Ziegler, J. Biersack and M. Ziegler, *SRIM - the stopping and range of ions in matter*, Chester, Maryland: SRIM Co, 2008.

[6] J.F. Ziegler, M.D. Ziegler, J.P. Biersack, Nucl. Instrum. Methods Phys. Res. B, **268**, 1818 (2010).

[7] V.Y. Banine, K.N. Koshelev, G.H.P.M. Swinkels, J. Phys. D: Appl. Phys., **44**, 253001 (2011).

[8] O.O. Versolato, Plasma Sources Sci. Technol. **28**, 083001 (2019).

[9] A. Bayerle, M.J. Deuzeman, S. van der Heijden, D. Kurilovich, T. de Faria Pinto, A. Stodolna, S. Witte, K.S.E. Eikema, W. Ubachs, R. Hoekstra, O.O. Versolato, Plasma Sources Sci. Technol., **27**, 045001 (2018).

[10] E. Bodewits, H.M. Dang, A.J. de Nijs, D.F.A. Winters, R. Hoekstra, Nucl. Instrum. Methods Phys. Res. B, **267**, 594 (2009).

[11] N. Stolterfoht, R. Hellhammer, D. Fink, B. Sulik, Z. Juhász, E. Bodewits, H.M. Dang, R. Hoekstra, Phys. Rev. A., **79**, 022901 (2009)

[12] S.T. de Zwart, A.G. Drentje, A.L. Boers, R. Morgenstern, Surf. Sci. **217**, 298 (1989).

[13] M. Krems, J. Zirbel, M. Thomason, R.D. DuBois, Rev. Sci. Instrum. **76**, 093305 (2005).

[14] L.C. Feldman, J.W. Mayer, *Fundamentals of Surface and thin film analysis*, Elsevier Science Publishing Co, New York, 1986.

[15] V.I. Shulga, Appl. Surf. Sci., **439**, 456 (2018).

[16] H. Niehus,W. Heiland, E. Taglauer, Surf. Sci. Rep., **17**, 213 (1993).

[17] W.K. Chu, J.W. Mayer, M.A. Nicolet, *Backscattering spectrometry*, Academic Press, New York, 1978.

Chapter 4

The crossed beam experiment

Abstract

This chapter describes the general features of the gas target setup, CHEOPS (CHarge Exchange Observed by Particle Spectroscopy). In this setup, crossed-beam type experiments are to be performed with the aim of measuring charge exchange cross sections. The beam current at different gas pressures is measured using a movable Faraday Cup (FC). A time-of-flight (ToF) spectrometer is used to measure the yield of charged target fragments.

4.1 Ion generation and transport

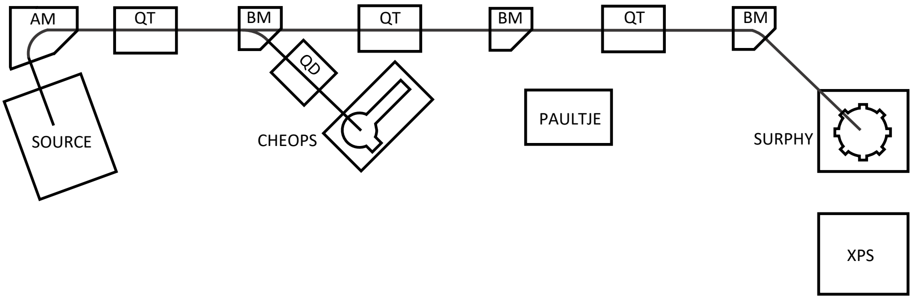

Figure 4.1: *Layout of the ion beam facility ZERNIKELEIF. AM: Analyzing magnet, QT: Quadrupole triplet, BM: Bending Magnet, QD: Quadrupole doublet. The facility houses four experimental setup: CHEOPS, PAULTJE, SURPHY and XPS.*

The layout of the Low Energy Ion-beam Facility (ZERNIKELEIF) is shown in figure 4.1. In the facility, ions are generated using an Electron Cyclotron Resonance (ECR) ion source [1]. The supernanogan-type ion source (see Fig. 4.2), manufactured by Pantechnik, consists of a copper vacuum chamber inside a permanent magnet for

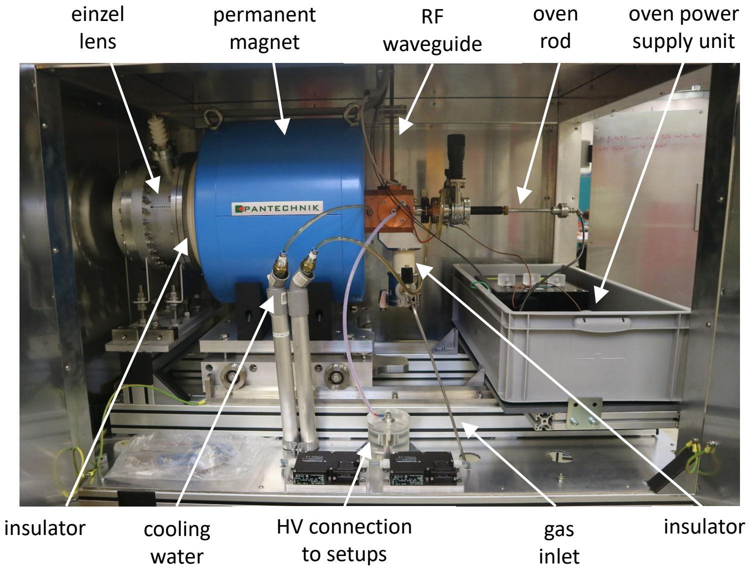

Figure 4.2: *Photograph of the ion source.*

magnetic plasma confinement. Gas(es) can be introduced into the chamber and the flow can be regulated by a motorized needle valve. For making ions of a material that is solid at room temperature, for e.g. Sn, the vapor is generated and introduced in the chamber by resistive heating of the sample in a crucible oven (see Fig. 4.3). Electrons in the plasma are heated using the principle of ECR by an external 14 GHz radio frequency (RF) source, manufactured by Sairem.

The source is set at a potential V_{ECR}, allowing for the extraction of the multiply charged ions, created at the source, into the beamline which is at ground potential. A so-called puller lens that can be set to a negative voltage is used to improve beam output and emittance, especially for the extraction of lower charge states at lower source potentials. The extracted ions can be focused further using an einzel lens. The energy of the ions upon extraction is given by

$$E = q(V_{ECR} + V_p), \tag{4.1}$$

where q is the charge state of the ion, V_{ECR} is the extraction voltage at the source and V_p is the plasma potential. V_{ECR} can be set in the range 3 kV - 25 kV and the small additional plasma potential is typically in the range of 7 to 20 V [2, 3]. For tens of keV of primary beam energy, the contribution from the plasma potential can be ignored for all practical purposes.

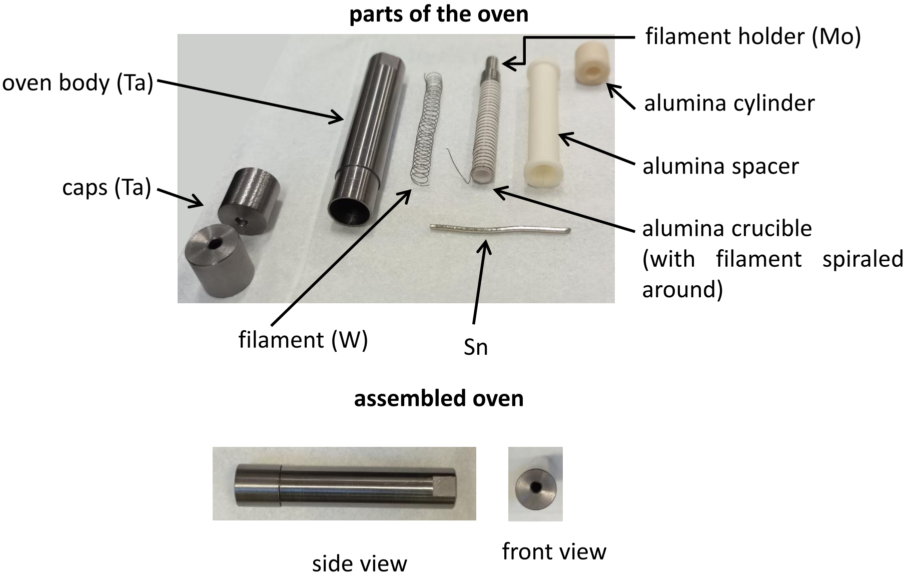

Figure 4.3: *Top panel: photographs of the oven parts. Solid Sn is placed inside the alumina container/crucible. Resistive heating of the filament that is spiraled around the crucible melts the Sn creating vapors that escape into the source chamber. Bottom panel: photographs of the assembled oven. Note in the front view, the off-centered ϕ 2 mm hole in the cap through which vapors diffuse out into the source chamber.*

The extracted ions are then filtered by a 110° analyzing magnet (AM, see figure 4.1). The AM is set at a certain magnetic field B_{AM} so that ions with only a specific mass-to-charge ratio A/q have the right trajectory to bend into the beamline and travel further. Here A denotes the mass of the ions (in units of u). Ions with other charge-to-mass ratios get intercepted and do not travel further. The relation between B_{AM} (in gauss), V_{ECR} (in kV), ion mass A (in u) and charge-state of the ion q is as follows:

$$B_{\mathrm{AM}} = 113.6\sqrt{V_{ECR}\frac{A}{q}} \tag{4.2}$$

With a resolution of ≈ 0.5 %, the AM can resolve different isotopes of Sn. Fig. 4.4 shows the result of a typical scan of the AM, with the source set at a potential of 4 kV. The beam current at FC placed immediately after the AM is measured over a range of A/q by scanning B_{AM} accordingly. In the figure, we see two different charge states of Sn: Sn^{2+} and Sn^{3+}. In the case of Sn^{2+}, we observe the isotope distribution of Sn as per the natural abundance. However, in the case of Sn^{3+}, the current of the most abundant isotope i.e. ^{120}Sn is higher than expected. This is due to the traces of Ar present in the background gas in the source which leads to the generation of $^{40}Ar^{+}$ ions that have the same mass-over-charge-state ratio of 40 as $^{120}Sn^{3+}$.

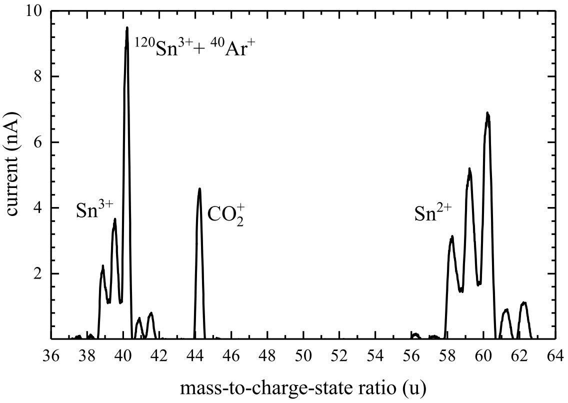

Figure 4.4: *Result of a typical scan of the 110 ° analyzing magnet over the range covering* Sn^{3+} *and* Sn^{2+} *ions.*

The analyzed beam enters the beamline after passing through a ϕ 10 mm diaphragm. The beam current is monitored by a movable Faraday Cup (FC) placed directly behind the diaphragm; while measuring the beam current, the FC is moved down into the beam and for transporting the beam further down the beamline the FC is moved up out of the beam. Currents can range from a few nA to hundreds of μA depending on the element, charge state, and energy selected. The 15 m long beamline consists of focusing elements - quadrupole triplet (QT) magnets and 45° bending magnets (BM). High vacuum is maintained in the beamline using ion-getter pumps. Typical pressure in the beamline is 5×10^{-8} mbar. For steering the beam off the beamline into the experimental setups, 45° BMs are used.

The beamline is connected to two permanent setups: gas target setup CHEOPS and solid target setup SURPHY. Additionally, the facility also hosts two independent setups not connected to the beamline - the XPS setup used for target analysis and the ion trap setup PAULTJE. In the following sections, the gas target setup CHEOPS is described.

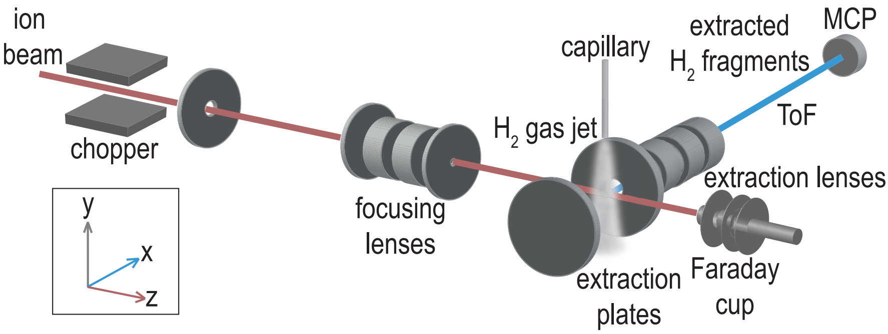

Figure 4.5: *Schematic of the CHEOPS setup.*

4.2 The experimental setup - CHEOPS

4.2.1 General overview

The schematic of CHEOPS is depicted in Fig. 4.5. In this setup, the collision of ions with the gas target is studied with diagnostic tools such as advanced FCs and a time-of-flight (ToF) mass spectrometer with H_2 as the chief target of interest.

The primary ion beam is steered off the central beamline into the setup using a 45° BM and focused using a quadrupole doublet (QD). Beam collimation is achieved by using a set of diaphragms whose dimensions are given in figure 4.6. The diaphragm closest to the collision chamber D_1 has a diameter of 1 mm. The setup allows for

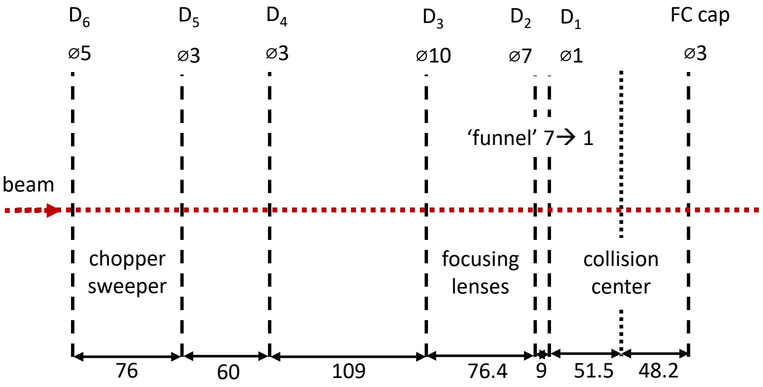

Figure 4.6: *Diameter of diaphragms in the CHEOPS (in mm) and distances between neighboring diaphragms.*

pulsing of the continuous ion beam transported from the source. This is achieved by means of a chopper. The generation of a pulsed beam using the chopper is discussed in section 4.2.2. The beam, continuous or pulsed, is collected in the end by a Faraday Cup (FC) that is connected to a current meter (Keithley 6485 picoammeter) to record the ion beam current. The details of the FC assembly and the measurements of ion beam current using the FC is discussed in section 4.2.4.

The collision chamber is differentially pumped using turbo molecular pumps. Pressures are measured at the collision chamber and at the drift tube of the ToF spectrometer using ion gauges. The base pressure in the collision chamber is $\approx 2 \times 10^{-8}$ mbar. The gas flows out of a 0.5 mm diameter, 75.6 mm long grounded capillary the orifice of which is located 14 mm above the beam plane. The flowrate of the gas is regulated by a high-precision mass flow controller (Bronkhorst FG-200CV). Fig. 4.7 shows the flow rate-pressure relation. The black dots represent chamber pressure and the red dots represent pressure at the ToF drift tube. The pressures increase linearly with flow rate, as is evidenced by the linear fits in Fig. 4.7, and the pressure at the ToF is always lower (a factor of ≈ 30) than the pressure in the collision chamber. Experiments were conducted in this linear flow-pressure regime.

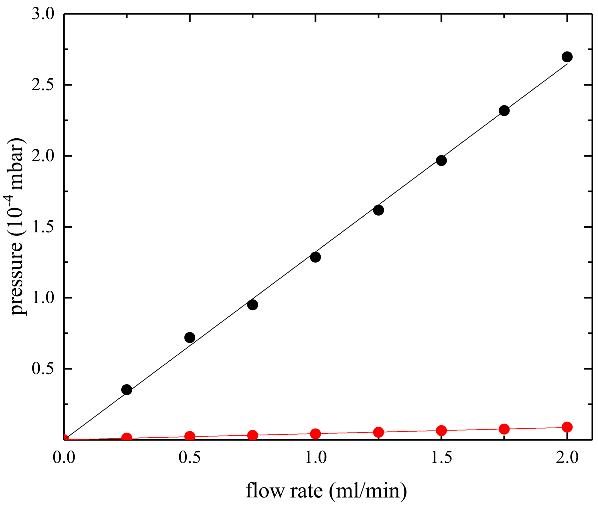

Figure 4.7: *Variation of pressures at the collision chamber (black dots) and the ToF drift tube (red dots) with flowrate set at the mass flow controller which regulates the gas jet density. The lines represent the linear fit to the data.*

4.2.2 Beam pulsing using chopper

The setup allows for pulsing of the continuous ion beam from the source. This is achieved by means of a chopper. The chopper consists of two parallel plates (30 mm × 30 mm with a thickness of 3 mm) separated by a distance of 6.5 mm.

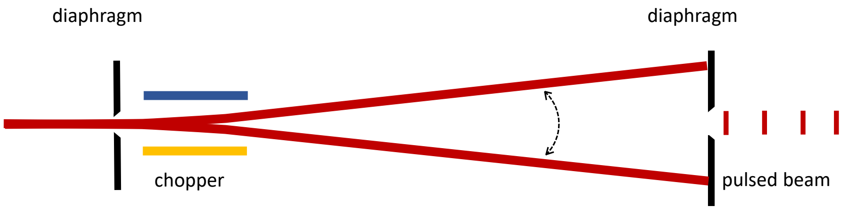

Figure 4.8: *Cartoon illustrating the pulsing of the beam using the chopper. The field direction between the plates of the chopper is toggled by alternating the polarities of the potentials on the plates (indicated by blue and yellow). This leads to the oscillation of the beam up and down as indicated by the arrows. During such motion, the beam sweeps over the exit diaphragm and a pulsed beam is generated.*

Chopping scheme

Fig. 4.8 illustrates the beam-pulsing scheme. When the chopper plates are set at equal but opposite voltages, $\pm V_{chop}$, the beam bends as it experiences a force due to the electrostatic field in the region between the plates. Consequently, it gets intercepted and does not pass through the exit diaphragm. If the polarity of the potentials on the plates is switched, the field flips direction and the beam bends but this time in the opposite direction. When this happens, the beam momentarily sweeps the exit diaphragm thus generating a pulse. By repeating this process at a certain chopping frequency, the continuous beam is converted into a pulsed beam. The chopper voltages are set using standard power supplies (Delta Elektronika ES0300). In order to alternate the voltages on the plates, two low-noise high voltage switches (Stahl-electronic HS-500) are used having a typical rise time of ≈ 35 ns. A standard TTL signal, generated by a pulse generator (BNC Model 555), is used as an external trigger for both the switches. The output of the switches are inverted with respect to each other i.e., if the output of switch 1 is $+V_{chop}$, then the output of switch 2 is -V_{chop} and vice versa. The two switches are connected to the chopper plates. Typical chopping frequency and chopping voltages are 8 kHz and ±60 V respectively.

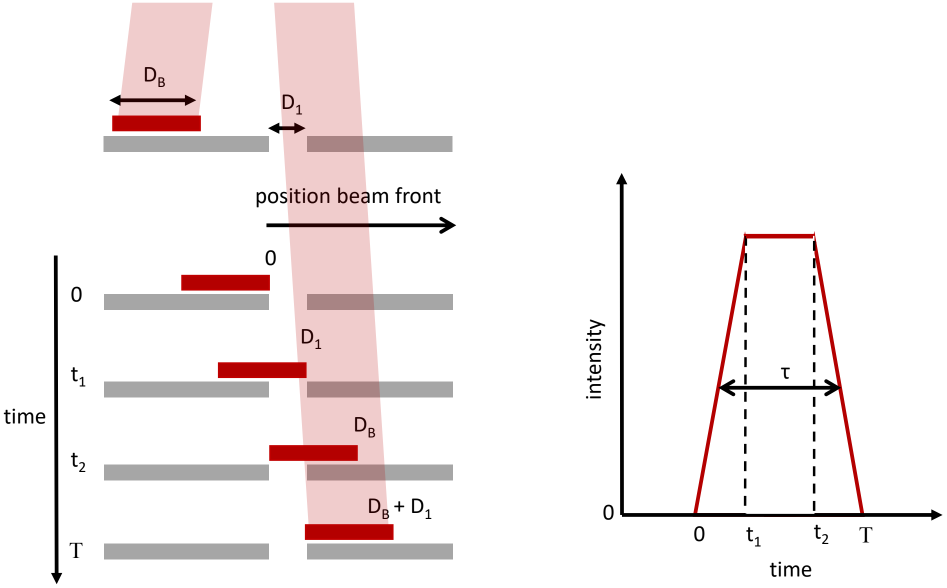

Figure 4.9: *Left: Stroboscopic cartoons of the beam (red block) with effective beam width* D_B *being chopped by being swept from left to right over the diaphragm* D_1 *(*$D_B > D_1$*). Right: The intensity profile of the pulsed beam. The pulse duration T gives the time interval between the arrival of the first and the last ions during one chopping instance. The pulse width* τ *is defined as the FWHM of the intensity profile.*

Estimation of pulse duration of beam pulses

Most of the ions experience a constant field during their transition through the chopper as the flight time of the ions across the chopper (hundreds of ns for Sn ions) is much shorter than the chopping period (typically 125 μs). These ions get bent off the beamline and thus do not pass through the exit diaphragm. Only the ions experiencing the polarity switch during their transition through the plates may end up passing through the exit diaphragm to generate a pulsed beam. Fig. 4.9 shows the beam during a sweep over the diaphragm D_1 from left to right. A blocked-shaped intensity distribution for the primary beam is assumed. Say at time 0, the right side of the beam just starts to pass through the exit diaphragm. The intensity of the signal will start to increase and after a certain time T the beam just gets fully blocked by the diaphragm again. The T gives the time duration between the passage of the first and the last ion during a sweep and is hereon referred to as the pulse duration. A simple expression for the pulse duration will now be derived assuming instantaneous switching of the potentials on the chopper plates. The acceleration of the ion

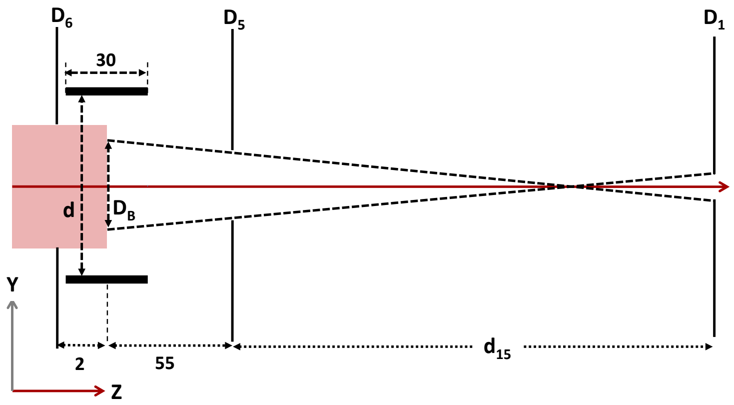

Figure 4.10: *Schematic showing the relevant dimensions for deriving an expression for pulse duration (not to scale - for illustration purpose only). D_1, D_5, and D_6 are the diaphragms along the beamline having diameters 1 mm, 3 mm, and 5 mm respectively. The beam (the red band drawn till halfway through the chopper) is first collimated by D_6. A portion of the beam is blocked by D_5 and the effective width of the beam that is swept across D_1 is given by D_B ≈ 3.6 mm. The dashed lines indicate the acceptance angle determined by diaphragms D_1 and D_6; distance between the chopper plates (d) = 6.5 mm; distance between diaphragms D_1 and D_5 (d_{15}) = 254.4 mm; other distances mentioned in the figure are also in units of mm.*

in the y direction, due to the field between the chopper plates, can be expressed as $a_y = 2qV_{chop}/md$ where d is the distance between the chopper plates (6.5 mm for the chopper used). The total y displacement of the ion on reaching the exit diaphragm depends on the vertical deviation from its original horizontal path at the end of the plates, and on the exit angle of the ion as it leaves the plates. We assume the former contribution to the displacement, i.e., the vertical deviation to be zero. The exit angle of the ion is analyzed by determining the z and y components of the ion velocity (see Fig. 4.10 for axes definition). If an ion experiences the field switch exactly halfway across the plates, the y-acceleration in the first and second part cancels out, thus the net y acceleration at the end of the plates is zero. However when the field-switch is experienced somewhere else then the net $v_y \neq 0$ and can be expressed as $v_y = a_y|t_1 - t_2|$, where t_1 is the time the ion experiences a force in the $+y$ direction and t_2 is the time the ion experiences a force in the $-y$ direction. Substituting for a_y we can express v_y as follows

$$v_y = \frac{2qV_{chop}|t_1 - t_2|}{md}. \tag{4.3}$$

The following condition for the passage of ions through the diaphragm D_1 can then be constructed.

$$\frac{v_y}{v_z} \leq \frac{\frac{1}{2}(D_1 + D_5)}{d_{15}}, \tag{4.4}$$

where v_z is the ion velocity that can be determined from its energy from the source, D_1 is the diameter of the diaphragm over which the beam is swept and chopped, D_5 is the diaphragm determining the effective beam size D_{B} and d_{15} is the distance from D_5 to D_1 (see Fig. 4.10).

Using Eq. (4.3), Eq. (4.4) and the relation $V_{ECR} \approx mv_z^2/2q$, we can arrive at the following relation

$$|t_1 - t_2| \leq \frac{d(D_1 + D_5)}{2d_{15}}.\frac{1}{v_z}.\frac{V_{ECR}}{V_{chop}} \tag{4.5}$$

Ions that satisfy the above condition pass through the exit diaphragm. The upper bound for $|t_1 - t_2|$ then gives the pulse duration T, which is the time interval between the passage of the first and the last ion in one sweep i.e.,

$$T = \frac{d(D_1 + D_5)}{2d_{15}}.\frac{1}{v_z}.\frac{V_{ECR}}{V_{chop}} \approx 5.11 \times 10^{-5}.\frac{1}{v_z}.\frac{V_{ECR}}{V_{chop}}, \tag{4.6}$$

where T is in units of s, v_z is the velocity of the ions in ms^{-1}.

4.2.3 ToF spectrometer

As described in the preceding section, the continuous ion beam from the source can be pulsed using the chopper. The pulsed beam then travels to the collision chamber and collides with the gas flowing off the capillary. Charged target fragments produced in a collision can be extracted towards a ToF spectrometer which allows for measuring the yields of the charged collision fragments.

Figure 4.11 shows the 2D visualization of the ToF spectrometer implemented in the software package, SIMION [5], which was used to simulate the target ion trajectories. The projectile ion beam travels along the z axis (pointing out of the plane in the figure) and the charged fragments of the target are extracted orthogonally along the x axis. The extraction plates labeled -1 and 1 in Fig. 4.11 are separated by a distance D_{ext} of 10 mm. Voltages of equal magnitude but opposite polarities are applied on the two plates to obtain an extraction voltage $V_{ext} = V_+ - V_- = 2V_+$. The extraction field thus created between the plates extracts the charged collision fragments. The entrance diaphragm to the spectrometer, D_{ToF} is 5 mm wide in diameter. Charged fragments that pass through this diaphragm are focused into the drift tube using an electrostatic lens system consisting of four elements labeled 2 - 5. The drift tube is

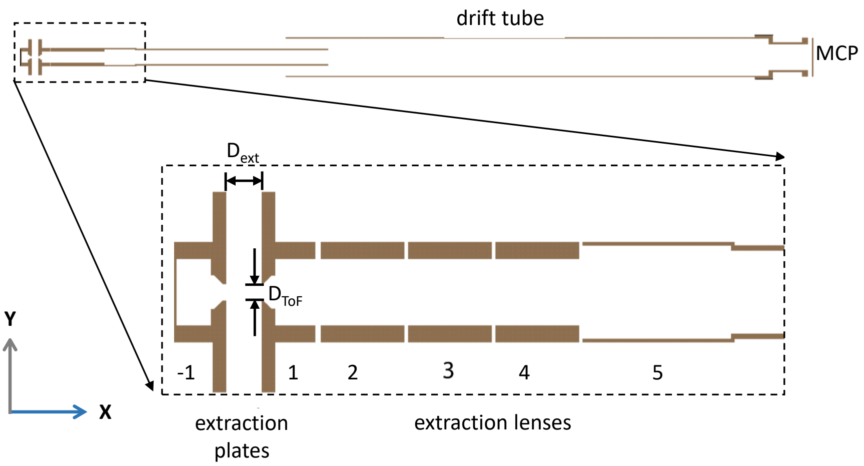

Figure 4.11: *2D visualization of the time-of-flight spectrometer in SIMION. The whole system has cylindrical symmetry.*

operated typically at -1700 V and a high transmission grid (88%) is mounted at the end of the drift tube. After the grid, there is a spacing of 7 mm before the front of the 43 mm multichannel plate (MCP, Elmul) detector. The front of the MCP is set at -2100 V. The spectrometer was simulated in SIMION to obtain optimal voltages for transporting charged fragments to the detector. The chamber and the drift tube are both differentially pumped using turbo molecular pumps. The flight distance measured from the center of the collision chamber to the front of the MCP is 1.16 m.

Data acquisition and analysis

A typical data acquisition scheme is depicted by the timing diagram in figure 4.12. The 5 V block pulses (red line in figure 4.12) trigger the HV switches connected to the chopper. At every edge of this signal (both rising and falling), the beam is pulsed. The pulsed beam travels to the collision chamber, collides with the target, and generates charged fragments. The extraction system then extracts the target fragments towards the MCP detector. The signal from the MCP, via a pickoff amplifier and Constant-Fraction-Discriminator (CFD), is fed as a STOP signal to a time digitizer (TDC, Fast ComTec P7888). The TDC is operated in stop-after-sweep mode. Its inputs are registered on their falling edge. At the falling edges of the START input signal, i.e, the 2.5 V block pulses indicated by the blue line in Fig. 4.12 , the sweep is triggered and the time count starts. Now the arrival times of the STOP input signal relative to the start are acquired. When the selected measurement time range elapses (≈ 50 μs if not stated otherwise), the sweep and thus the data acquisition ends. After

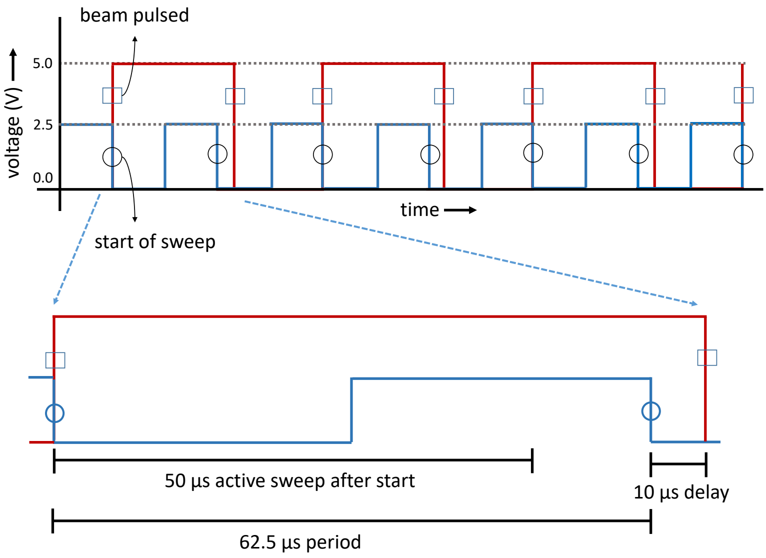

Figure 4.12: *Typical timing diagram for beam pulsing and ToF data acquisition. The red block pulses represent the external trigger signal for the HV switches that the chopper is connected to. At every edge of this signal, the ion beam is pulsed. The blue block pulses represent the trigger fed as START input signal to the TDC. At every falling edge of this signal, data acquisition (i.e., sweep) commences.*

a short ($\leq$ 200 ns) end-of-sweep deadtime, the TDC will begin a new sweep as soon as the next START signal arrives.

Salient features of the ToF spectra

The data from the TDC can be analyzed to plot the ToF spectrum of the first detected ion product i.e., the first-stop ToF spectrum. The flow of the gas is set such that the count rate at the detector is below 10% of the chopping frequency to ensure operation in the single collision regime. The spectrum on the left of Fig. 4.13 shows the ToF spectrum for 50 keV N^{5+} colliding with H_2 while that on the right is for 17 keV OH^+ colliding with H_2. The most intense peak at 3.62 μs for both the cases corresponds to the H_2^+ ions generated after single electron capture from H_2.

The inset in both the figures shows the much weaker signals from protons. We also note that the peak structure is different for the two cases of N^{5+} and OH^+. The

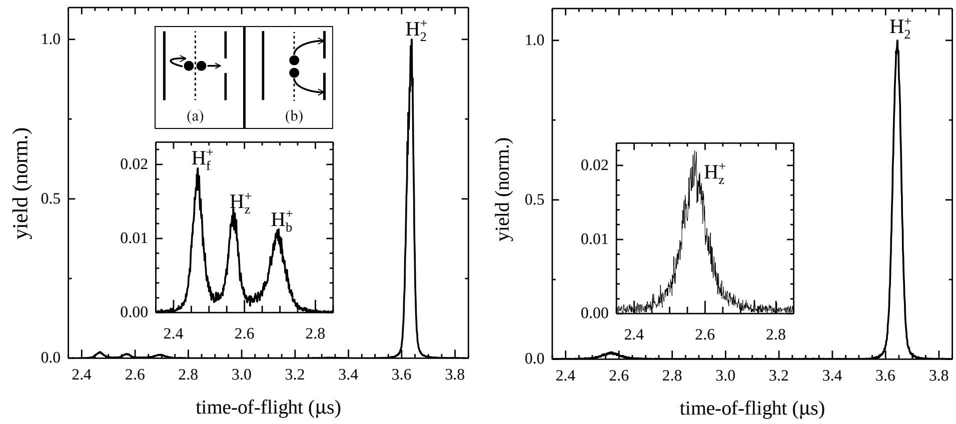

Figure 4.13: *ToF flight spectra for 50 keV N^{5+}(left) and 17 keV OH^+ colliding with H_2. The relatively weaker proton signals are shown in the zoom-in both the figures.*

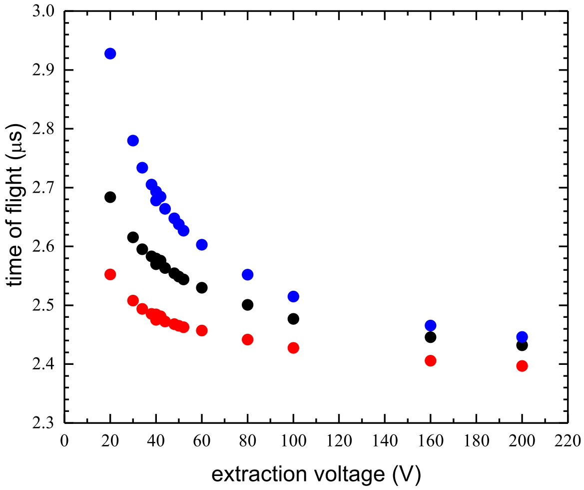

Figure 4.14: *Locations of H_f^+ (red), H_z^+ (black) and H_b^+ (blue) peaks at different extraction voltage for 84 keV Kr^{5+} colliding with H_2.*

central peak labeled H_z^+, corresponding to 0-eV protons stemming from the gentle dissociation of the H_2^+ ions [6], is present in both spectra. However, in the case of N^{5+}, there are two additional peaks on either side of the H_z^+. These peaks labeled forward-emitted-proton (H_f^+) peak and back-emitted-proton peak (H_b^+) correspond to the 9.7 eV protons generated after double electron capture from H_2. Following double electron capture, the H_2 dissociates into two H^+ ions which fly apart in opposite directions conserving momentum. Due to the finite size of the ToF entrance diaphragm, many proton pairs thus generated get intercepted as shown in inset (b) in Fig.4.13. Only those fragments that are emitted close to the detection axis end up getting detected as depicted in inset (a) of Fig. 4.13. The time difference between the H_f^+ and H_b^+ scales with the square-root of the kinetic energy release (U_{KER}) of the dissociation process and for singly charged fragments it is given by [7]:

$$\Delta T = \frac{\sqrt{8\,\mu\,U_{KER}}}{E}, \qquad (4.7)$$

where $E = V_{ext}/D_{ext}$ is the extraction field between the extraction plates, μ is the reduced mass which for H_2 is 0.5, and U_{KER} is the kinetic energy release following the dissociation. U_{KER} for Coulomb explosion of $[H_2]^{2+}$ is 19.4 eV. H_f^+ and H_b^+ with a ToF separation ΔT corresponding to 19.4 eV, are signatures to collision systems for which double capture is a likely capture channel. Since double capture is not an option for the OH^++H_2 system, H_f^+ and H_b^+ are not present in its ToF spectrum which shows only one single proton peak (right figure in Fig. 4.13).

Fig. 4.14 shows a typical variation in proton peak positions with changing extraction voltage V_{ext}. This particular set of experiments was performed with 84 keV Kr^{5+}. The H_f^+ (red dots), H_z^+ (black dots), and the H_b^+ (blue dots) come closer together as the extraction is increased. Thus in order to resolve the peaks, a lower extraction voltage is desirable. However, at lower extraction voltage, the count rate is reduced thus longer data acquisition times are required. For the subsequent experiments, an extraction voltage of 40 V was chosen as at this setting the peaks could be well resolved without compromising on the count rate.

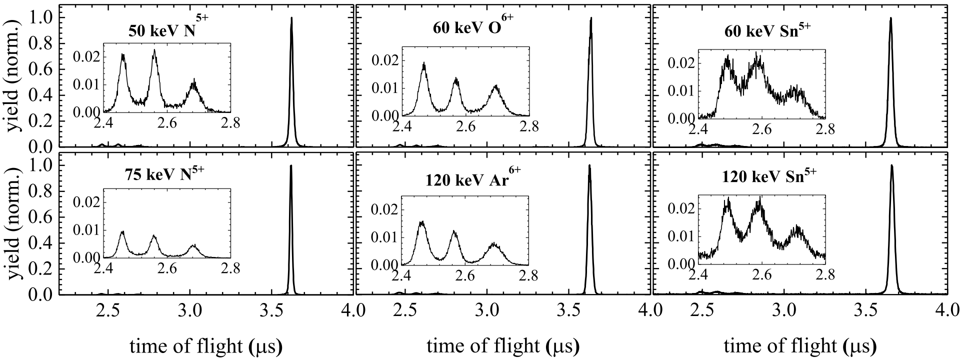

Figure 4.15: *Compilation of some ToF spectra for collisions of multiply charged ions with H_2.*

The comparison of the predictions of Eq. 4.7 with the experiments is difficult as this

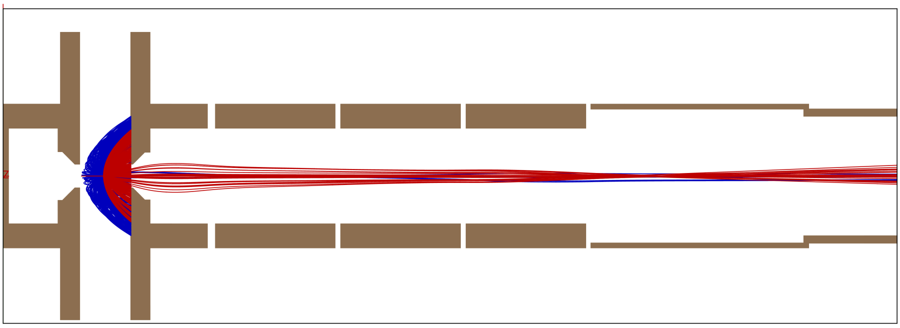

Figure 4.16: *SIMION visualization showing the trajectories of 9.7 eV protons emitted in the forward (H_f^+, red) and backward (H_b^+, blue) directions. The backward-emitted protons spread out more in comparison to the forward-emitted protons before reaching the entrance diaphragm plane leading to a difference in their yields measured by the detector.*

requires the identification of the exact time stamps of the forward- and backward-emitted protons emitted in perfect alignment to the detection axis. Therefore, we take the peak maxima to be representative of the separation between H_f^+ and H_b^+. We check the validity of this approach by analyzing the ToF spectra of several multiply charged ions for which double electron capture is a likely capture process (a small compilation of such spectra is shown in Fig. 4.15). In all the spectra, similar peak separations were observed i.e. $220(\pm 5)$ ns for an extraction voltage of 40 V (i.e extraction plates at ±20 V).

The other feature we see in the proton peaks is the difference in yield between H_f^+ and H_b^+. The backward emitted protons have to make a U-turn before moving towards the spectrometer again. Therefore, compared to the forward-emitted protons, the backward emitted protons spend more time in the field which results in reduced transmission through the entrance diaphragm. This point is illustrated by the visualization of the SIMION simulations in figure 4.16. In the simulation, a point ion source is placed at the center of extraction plates -1 and 1, emitting 9.7-eV protons in all directions. The protons emitted forward (towards plate 1) are shown in red whereas the protons initially emitted backward (towards plate -1) are shown in blue. The extraction plates are set at ± 20 V. We see that the backward emitted protons in blue, having spent more time in the extraction field region, spreads out more than the forward emitted ions leading to a difference in their transmission which subsequently gets reflected in their yield in the ToF spectrum.

In Fig. 4.13, the 0-eV H_2^+ peaks have a finite width. The following factors contribute towards the broadening of the H_2^+ peak: the finite pulse length τ of the beam

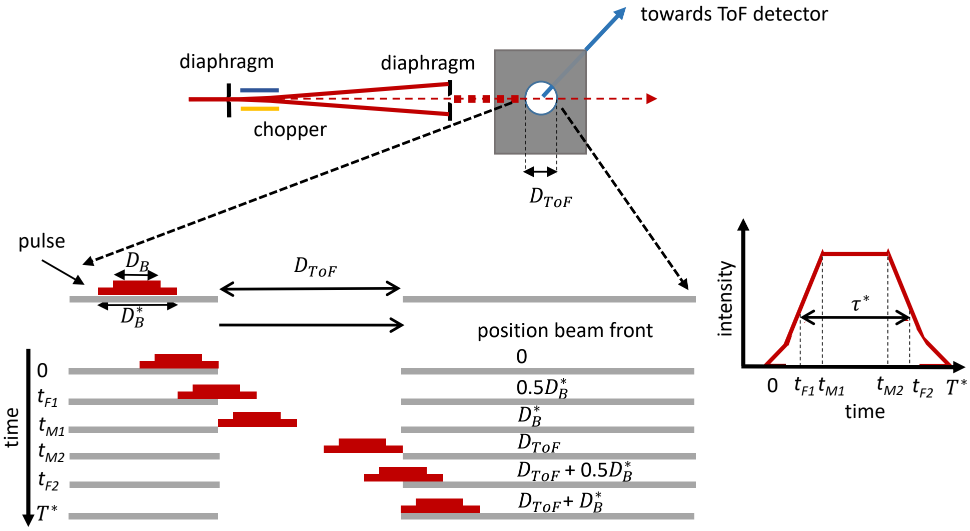

Figure 4.17: *Illustration of the broadening effect due to passage time. The pulsed beam (red block) travels from left to right, crossing the entrance diaphragm of the ToF spectrometer.*

bunches, the passage time of a beam pulse to cross the ToF entrance diaphragm with diameter D_{ToF}, the lateral depth of the gas target, the recoil energy, and the electronics. Within the energy range of the experiments, the broadening due to recoil from the projectile ion is expected to be negligibly small in the first approximation [8]. The broadening due to the lateral depth of the target and the electronics is expected to remain unchanged if the same voltages are used for the extraction and the lens system during the experiments. Thus the only two factors that may change appreciably between experiments are the pulse length of the chopped ion beam and the passage time of the ions across the ToF-entrance diaphragm. As shown earlier, the pulse duration T can be estimated using Eq. 4.6. When the effect of the finite passage time is included, the expression for effective pulse duration T^* becomes

$$T^* = T + \frac{D_{ToF}}{v_z}, \tag{4.8}$$

where T is the pulse duration of the chopped beam derived in section 4.2.2., D_{ToF} is the entrance diaphragm of the ToF spectrometer and v_z is the velocity of the ion.

The effective pulse length τ^*, which includes the effect of the passage time of the

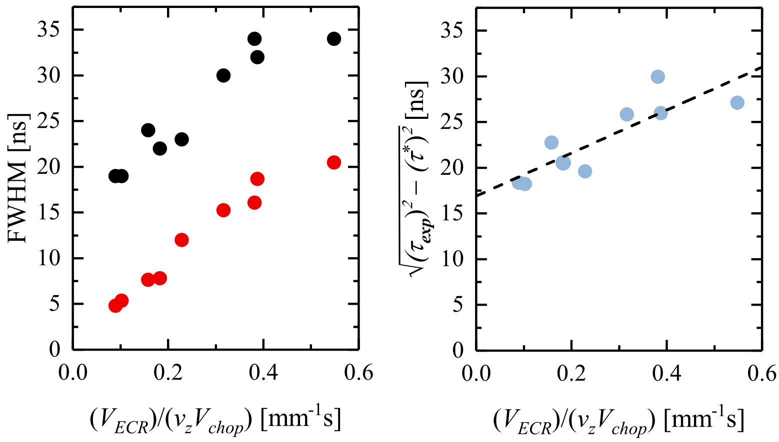

Figure 4.18: *Left: Comparison of the experimentally obtained FWHM τ_{exp} (black dots) of the H_2^+ peak with the corresponding τ^* (red dots), i.e. the FWHM calculated using Eqs. 4.9. Right: Quadratic difference between the experimentally obtained τ_{exp} and the corresponding τ^*.*

pulsed beam across the entrance diaphragm of the ToF, can now be expressed as

$$\tau^* = \frac{D_{ToF}}{D_B^* + D_{ToF}} T^* \approx 0.52\, T^*, \tag{4.9}$$

where the entrance diaphragm of the ToF spectrometer , D_{ToF} = 5 mm and D_B^* denotes the sum of the effective beam size D_B (see Fig. 4.10) and the diameter of the diaphragm, D_1 where the beam is chopped i.e. D_B^* = D_B + D_1 = (3.6 + 1) mm = 4.6 mm, . The derivation of Eq. 4.9 is illustrated in Fig. 4.17.

The analysis of the H_2^+ peak allows for the comparison of the estimated τ^* with the experimental observations and thus allows for an estimation of the common broadening factors not included explicitly in the calculations. For this, a Gaussian peak is fitted to the experimental H_2^+ peak and the FWHM labeled τ_{exp} thus obtained is compared to τ^* (see Fig. 4.18, left figure). In the figure, the black dots represent τ_{exp} and the red dots represent the corresponding $\tau*$ calculated using Eq. 4.9. It is evident that the τ_{exp} are wider than $\tau*$. This is expected as the calculations do not account for other broadening terms such as the recoil from the projectile ion, the electronics, and the lateral target size. The right figure in Fig. 4.18 shows the quadratic difference between τ_{exp} and the calculated $\tau*$, i.e, $\sqrt{\tau_{exp}^2 - \tau^{*2}}$. It is evident that the difference is not constant but increases slightly with $1/v_z$ which is what we may expect from the $1/v_z$ dependence of the recoil momentum [8]. A linear fit to the quadratic differences yields an intercept of 17±2 ns, which gives an estimate of the broadening terms such as electronics and lateral target depth.

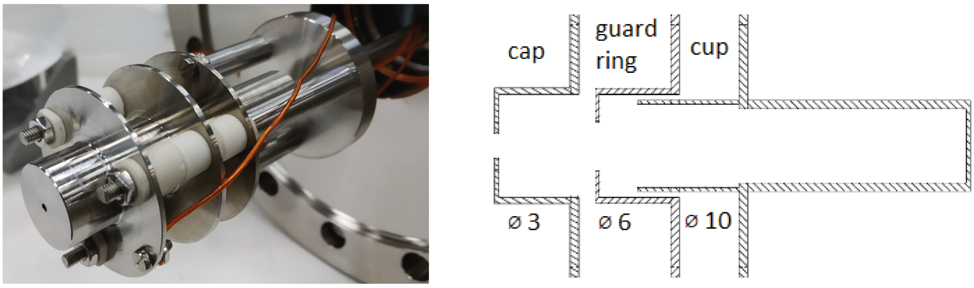

Figure 4.19: *Left: Photograph of the FC assembly. Right: Schematic of the FC assembly with an opening diameter of the different components labeled.*

4.2.4 Faraday cup and beam current measurement

As mentioned above, the ion beam, chopped or continuous, is collected at the end by a Faraday cup (see Fig. 5.1). This allows for the monitoring of the ion beam at various H_2 pressures and thus the effect of collisions on the ion beam can be probed.

Fig. 4.19 shows the Faraday cup installed in the setup. It is an assembly of three components: i) the entrance cap with a ϕ 3 mm aperture, ii) a ϕ 6 mm guard ring, and iii) the FC. The guard ring is typically biased at -38 V in order to suppress the escape of secondary electrons from the FC. The cap shields the collision chamber from the field of the guard ring. The entire FC assembly is mounted on an XY translation stage. By scanning it in the horizontal and vertical planes and recording the current in the cap and FC, a typical beam width of $\approx$1.5 mm at the FC is determined.

The current measured on the FC ranges from tens of pA to hundreds of nA, depending on the ion beam. Fig. 4.20 shows a typical FC time trace while measuring the continuous beam but at different H_2 pressures. Such measurements are done to calculate charge exchange cross sections (discussed in the following chapters). In the figure, the middle and the bottom panel show the current at the FC and the cap respectively. We see that when there is H_2 in the chamber, the FC current decreases. This is due to the fact that upon introduction of H_2 into the chamber, the ions collide with H_2 molecules and undergo charge exchange. Thus many ions are converted to lower charge states. Unlike the FC current, in the presence of H_2, the very small current at the cap increases. This may be attributed to the scattering of the ions from the H_2 molecules that leads to an increase in beam divergence and thus an increase in the beam size at the FC. A small fraction of the beam that was fully collected by

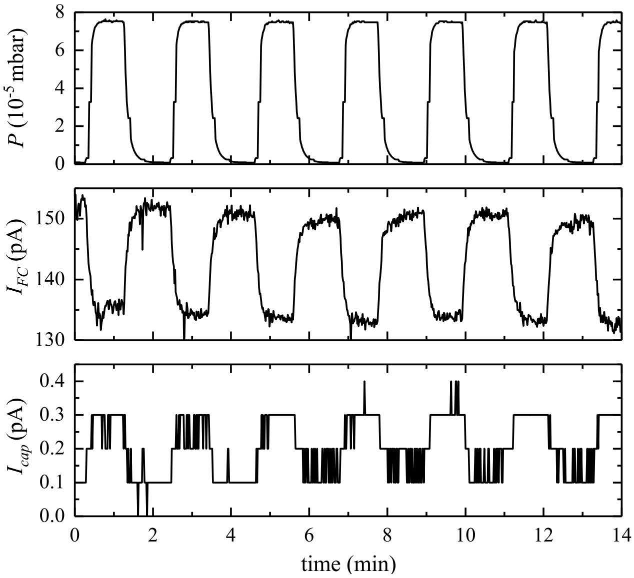

Figure 4.20: *Typical time trace: Variation of ion beam current measured at the Faraday cup (middle panel) and the cap (lower panel) with toggling H_2 flowrate between 0 and 0.5 ml/min. The top panel shows the associated time trace of the pressure in the collision chamber.*

the FC in the absence of H_2, now ends up hitting the cap. It may be noted, however, that the cap current is significantly lower in magnitude than the Faraday cup current, typically more than a factor of 100.

Bibliography

[1] R. Geller, Electron cyclotron resonance sources: Historical review and future prospects (invited), Rev. Sci. Instrum. **69**, 1302 (1998)

[2] S. T. de Zwart, *PhD thesis*, University of Groningen (1987).

[3] G. Lubinski, G Lubinski, Z. Juhász, R. Morgenstern and R. Hoekstra, J. Phys. B: At. Mol. Opt. Phys. 33 5275 (2000).

[4] E. S. Brinkhuis *Bachelor thesis*, University of Groningen (2020).

[5] SIMION 8.0 software package, https://simion.com/.

[6] S, Martínez, G. Bernardi, P. Focke, A. D. González and S. Suárez, J. Phys. B: At. Mol. Opt. Phys. 36, 4813 (2003).

[7] H. O. Folkerts, F. W. Bliek, M. C. de Jong, R. Hoekstra, and R. Morgenstern, J. Phys. B: At. Mol. Opt. Phys. **30**, 5833 (1997).

[8] S. Knoop, *PhD thesis*, University of Groningen (2006).

Chapter 5

Charge exchange in collisions of 1 - 100 keV Sn^{3+} ions with H_2 and D_2

Abstract

Absolute cross sections for single electron capture by Sn^{3+} *colliding with* H_2 *and* D_2 *have been measured and calculated in the energy range of 1 - 100 keV. The cross sections are determined by measuring the change in ion beam current with varying target density and by measuring the yields of charged target fragments by means of a time-of-flight spectrometer. The results for* D_2 *show good agreement with our seven-state semi-classical calculations, while for* H_2 *the experimental results increase more strongly than the calculations towards lower energies. This discrepancy is attributed to vibrational effects, not included in the calculations, that lead to the breakdown of the Franck-Condon approximation.*

5.1 Introduction

Charge exchange in collisions of keV-energy multiply-charged ions with neutral species remains an active research topic ever since the advent of highly charged ion sources (e.g. [1–3]). Experiments have continually challenged, in ever-increasing detail, the theoretical approaches, which were initially classical and subsequently semi-classical in their description of the electron dynamics during the interactions (e.g. [4]). The bulk of the research has dealt with low-Z ions, because the number of active electrons and quantum states to be included in the calculations is limited and because intense ion beams can most easily be produced from low-Z, gaseous species. More complex and heavier ions, in particular intermediately charged Fe ions, have been studied (e.g. [5–7]) because of their astrophysical and fusion plasma relevance.

Chapter published: S. Rai, K.I Bijlsma, I. Rabadán, L. Méndez, P.A.J Wolff, M. Salverda, O.O. Versolato, and R. Hoekstra, *Charge exchange in collisions of 1 - 100 keV* Sn^{3+} *ions with* H_2 *and* D_2, Phys. Rev. A **106**, 012804 (2022).

Over the last years, Sn ions have moved into the focus of highly charged ion physics [8–14] as Sn alloys are considered for fusion plasma vapor shielding [15–17] and foremost because laser-produced Sn plasma is the source of 13.5-nm extreme ultraviolet (EUV) light driving state-of-the-art EUV nanolithography machines [18–22]. In such machines, multilayer mirror optics collect and guide the EUV light [23, 24]. To prevent damage to the optics by the energetic Sn ions [25–27], the plasma is embedded in H_2 gas. Fundamental data on charge exchange and stopping in $Sn^{q+} + H_2$ collisions is missing though it is crucial for accurate and predictive modeling.

In this joint experimental and theoretical study, absolute cross sections for single electron capture (SC) from H_2 (and its heavier isotopologue D_2) by Sn^{3+}, i.e. for the reaction

$$\mathrm{Sn}^{3+} + \mathrm{H}_2 \to \mathrm{Sn}^{2+} + \mathrm{H}_2^+ \tag{5.1}$$

are determined. The choice for starting out with Sn^{3+} ions is based on its alkali-like electronic configuration: [Kr]$5d^{10}5s$. For alkali-like ion beams, metastable fractions are negligible [28] making the collision systems tractable to experiment and theory. In the experiments, Sn^{3+} ions in the energy range of 9 to 51 keV are used as projectiles. Due to the high mass of the Sn ions, this corresponds to low velocities of 0.05 to 0.13 a.u. The cross section measurements are based on the measurement of the changes in ion beam current with changing target density. Therefore, in the determination of the SC cross sections, one needs to consider possible contributions of two-electron processes: bound double capture (BDC, Eq. 5.2a) and autoionizing double capture (ADC, Eq. 5.2b).

$$\mathrm{Sn}^{3+} + \mathrm{H}_2 \to \mathrm{Sn}^{+} + 2\mathrm{H}^+ \tag{5.2a}$$

$$\mathrm{Sn}^{3+} + \mathrm{H}_2 \to \mathrm{Sn}^{2+} + 2\mathrm{H}^+ + e. \tag{5.2b}$$

BDC is expected to have a small cross section because the two-electron capture channel closest to resonance is the one leading to capture into the [Kr] $5d^{10}\,5s^2\,5p$ ground electronic configuration of Sn^+ which is endothermic by approximately 6 eV. All other $5s^2\,nl$ configurations are more endothermic and thus not likely to be populated at all. ADC requires the population of doubly excited levels of even much higher endothermicity. Therefore it is safe to exclude ADC from our analysis. The BDC contribution is extracted from Time-of-Flight (ToF) spectrometry on the target fragments. In BDC, the two protons resulting from the Coulomb explosion of $[H_2]^{2+}$ get kinetic energies of 9.7 eV each, while in SC reactions the few protons created next to the by far dominant H_2^+ production channel have energy close to 0 eV. The yield of 9.7-eV protons is used to correct the data for any BDC contribution. At the same time, this allows for an assessment of the BDC cross sections.

The calculations of SC total cross sections for ion-molecule collisions are carried out by applying methods based on those developed for ion-atom collisions; for instance, at the energies of the present work, expansions in terms of electronic functions of the quasi-molecule formed during the collision, within either semi-classical or quantal frameworks. Besides the obvious difference of treating a many-center system, there are two important characteristics of ion-molecule collisions that must be taken into account. First, in the semi-classical treatment, where the projectile follows a classical trajectory, the probabilities of a given process depend on the orientation of the molecule with respect to the ion trajectory. It is necessary to average the calculated cross sections over a set of collisions with different molecular orientations. The methodology employed in this work ([29] and references therein) employs molecular data (electronic energies and dynamical couplings) calculated along the trajectory. The second important difference between ion-molecule collisions with respect to ion-atom collisions is the presence of molecular nuclear motion. The use of vibronic bases to simultaneously describe the electronic and vibrational motions leads to cumbersome calculations that however allowed us to reproduce the maximum of the electron capture cross section found in detailed experiments for H^+–H_2 collisions, and explain this maximum as a consequence of the interplay between electronic and nuclear motions [30].

In the following section 5.2, part 5.2.1 describes the experimental setup, while subsections 5.2.2 - 5.2.5 present the actual measurement procedure and all the calibration and data analysis steps. Section 5.3 describes the theoretical approaches used to calculate single-electron capture in collisions of Sn^{3+} on either H_2 or D_2. Thereafter the experimental and theoretical data are compared and discussed in section 5.4.

5.2 Experimental methods

The data presented in this work have been obtained by colliding a beam of mono-energetic Sn^{3+} ions with a neutral gas target (H_2 or D_2) in a series of crossed-beam type experiments. The ions are extracted from an Electron Cyclotron Resonance Ion Source (ECRIS) stationed at the ZERNIKE Low Energy Ion-Beam Facility (ZERNIKELEIF) at the University of Groningen. Ions with energies in the range of $3q$ to $25q$ keV can be generated, where q is the charge state of the ion. The ions extracted from the ion source are selected for a given mass-over-charge ratio (m/q) using a 110° analyzing magnet with a resolution of about 0.5%. ^{120}Sn is the most abundant isotope of Sn but for a charge state of 3, the corresponding m/q is 40 which is the same as that of Ar^+. Hence to prevent possible contamination of the Sn^{3+} beam by Ar^+ impurities, $^{118}Sn^{3+}$ is used. Sn atoms are introduced into the source chamber by heating a crucible oven filled with solid tin. The analyzed ion beam is transported through the

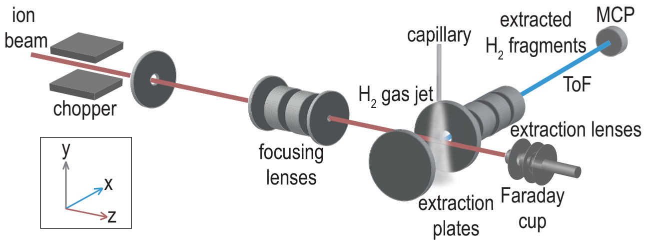

Figure 5.1: *Schematic of the crossed-beam setup, CHEOPS, used to measure charge exchange cross section for keV* Sn^{3+} *ions colliding on* H_2 *(and* D_2*).*

central beamline and steered into the gas target setup by a 45° bending magnet.

5.2.1 The crossed-beam setup

The relevant features of the gas target setup, CHEOPS (CHarge Exchange Observed by Particle Spectroscopy) are depicted in Fig. 5.1. The ion beam is collimated by a set of four apertures, the smallest one of 1 mm diameter, positioned at the entrance of the collision chamber. In the chamber, the base pressure is $\approx 2 \times 10^{-8}$ mbar. A ϕ0.5 mm grounded capillary is located 14 mm above the center of the ion beam. The gas flowing into the chamber, via the capillary, is regulated by a high precision mass flow controller (Bronkhorst FG-200CV) thus creating a localized jet of the H_2 target gas, which is crossed by the beam. A flowrate of 1 ml/min was used throughout the experiments unless stated otherwise and the corresponding chamber pressure for that flow is $\approx 1.5\times10^{-4}$ mbar. The ions are collected at the end of the setup by a Faraday Cup (FC) and the beam current is measured using a Keithley 6485 Picoammeter. The FC assembly consists of three components: i) the entrance cap with a ϕ3 mm aperture, ii) a ϕ6 mm guard ring, and iii) the FC. The guard ring is biased at -38 V to suppress the escape of secondary electrons from the FC. The cap shields the collision chamber from the field of the guard ring. The whole FC assembly is mounted on an XY translation stage. By scanning the assembly in the horizontal and vertical plane and recording the current at the cap and FC a typical beam width of $\approx$ 1.5 mm at the FC is determined.

Charged collision fragments produced in the central crossed-beam region can be extracted towards a Time-of-Flight (ToF) spectrometer, which allows for measuring the yields of atomic H^+ and molecular H_2^+ ions. The ToF measurements (see Sect. 5.2.4) require the continuous ion beam to be chopped in short pulses to have a start pulse for the spectrometer. At a rate of up to 8 kHz short $\approx$ 20 ns ion beam pulses are generated by sweeping the ion beam over the entrance aperture by means of alternating the opposite voltages on two electrodes (chopper plates, see Fig. 5.1).

Fragments under the influence of the field across the collision center pass through a ϕ 5 mm aperture into the ToF spectrometer. An electrostatic lens system consisting of four elements is then used to accelerate and focus the fragments into the ToF tube floating at -1700 V. Towards the end of the tube, the fragments get detected by a microchannel plate (MCP) detector whose front plate is set to -2100 V. The total flight length from the collision center to the detector is 1.13 m. The MCP detector is connected to a pick-off amplifier followed by a constant-fraction-discriminator (CFD) to amplify and filter the signals. The output of the discriminator is fed to a multi-hit time-to-digital converter (TDC, FAST P7888) in order to record the ToF spectrum.

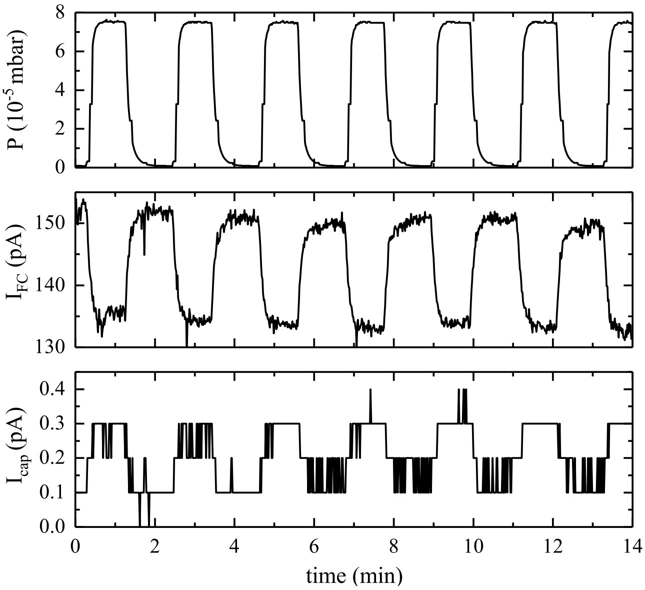

Figure 5.2: *Typical time trace: Variation of ion beam current measured at the Faraday cup (middle panel) and the cap (lower panel) with toggling H_2 flow rate between 0 and 0.5 ml/min. The top panel shows the associated time trace of the pressure in the collision chamber.*

5.2.2 Procedure of measuring charge exchange cross sections

Fig. 5.2 shows the time trace of a typical measurement run. The flow controller is programmed to sequentially start/stop the flow of gas into the chamber. The top panel in the figure shows the variation of chamber pressure with acquisition time. When the gas flows from the capillary into the chamber, the ion beam crossing the gas may undergo charge exchange collisions. This leads to a decrease in the beam current measured by the FC as shown in the middle panel of the figure. The collision of the ions with the gas also results in angular scattering of the ion beam. If the scattered ions hit the cap, a current is generated and recorded as depicted in the bottom panel of the figure. The effect is however small; the change in cap current is typically around 1% of the change in FC current.

The full set of differential equations describing the evolution of the charge state of the ions along their trajectory (z) through the collision chamber is as follows:

$$\frac{dN^{3+}}{dz} = -(\sigma_{32} + \sigma_{31}) n N^{3+} \tag{5.3a}$$
$$\frac{dN^{2+}}{dz} = \sigma_{32} n N^{3+} - (\sigma_{21} + \sigma_{20}) n N^{2+} \tag{5.3b}$$
$$\frac{dN^{1+}}{dz} = \sigma_{31} n N^{3+} + \sigma_{21} n N^{2+} - \sigma_{10} n N^{1+} \tag{5.3c}$$
$$\frac{dN^{0+}}{dz} = \sigma_{20} n N^{2+} + \sigma_{10} n N^{1+}. \tag{5.3d}$$

In the low-density, single-collision regime the set of equations is reduced to:

$$\frac{dN^{3+}}{dz} = -(\sigma_{32} + \sigma_{31}) n N^{3+}. \tag{5.4}$$

Here, σ_{ij} denotes the cross section for electron capture by an ion in an initial charge state i leading to a final charge state j, n is the number density of the target and N^{q+} denotes the number of Sn ions with charge state q. The numbers of ions are related to the ion current I measured in the FC via $I = qN^{q+} + (q-1)N^{(q-1)+} + (q-2)N^{(q-2)+}$. The differential equation for single-collision conditions, Eq. 5.4, can be solved analytically, yielding the following general relation between ion beam current and the single-capture cross section σ_{SC} (or $\sigma_{q,q-1}$)

$$\sigma_{SC} = \frac{-\ln\left(a\frac{I}{I_o} - b\right)}{(1+f)\int_0^L n(z)dz}, \tag{5.5}$$

where I_0 is the initial ion current, f the ratio between two- and one-electron capture ($f = \frac{\sigma_{BDC}}{\sigma_{SC}}$), $a = \frac{(1+f)q}{1+2f}$, $b = \frac{(1+f)q-(1+2f)}{1+2f}$, and L the path length the ions travel through the collision chamber. Here for Sn^{3+}, $q = 3$. As will be discussed in detail in Sec. 5.2.4, the bound double capture fraction f is estimated experimentally from ToF measurements on target fragments (H^+ and H_2^+). However, first in Sec. 5.2.3 the determination of the integral target density $\int_0^L n(x)dx$ is presented.

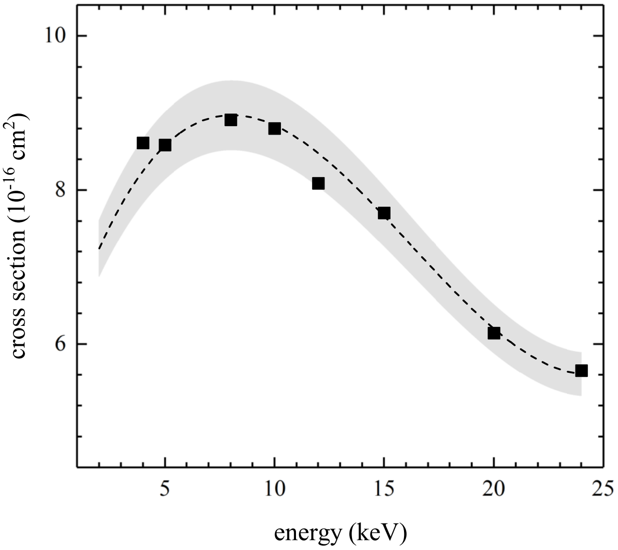

Figure 5.3: *Single electron capture cross section for protons on* H_2 *(solid squares). Dashed curve: trendline through reference data [31]. The grey band depicts the* $\pm5\%$ *systematic uncertainty associated with the McClure data.*

5.2.3 Calibration of the integral target density

Accurate, absolute target density measurements over the ion trajectory are difficult. Therefore we determine the integral target density using a reference collision system for which the charge exchange cross sections are very well known: H^+ + H_2, see e.g. the data review by Nakai *et al.*[32].From the review paper we see that for protons only single electron capture (σ_{10}) needs to be considered; in the energy range of 5 to 20 keV, double electron capture is approximately two orders of magnitude smaller than one-electron capture [32]. This implies that Eq. (5.5) for protons on H_2 simplifies significantly (with $f = 0$ and $q = 1$) and can be rewritten to:

$$\int_0^L n(z)dz = -\frac{\ln \frac{I}{I_o}}{\sigma_{10}} = \beta P \tag{5.6}$$

to extract the integral target density from a measurement of the change of proton current. Here β is introduced as the proportionality factor between the integral target density and the pressure P in the collision chamber. From the many studies reported in Nakai's review paper [32], we used the cross sections σ_{10} reported by McClure [31] for calibration. McClure's set of cross sections covers our range of interest and at energies of 5 keV and lower, there is excellent agreement with the results of an elaborate joint experimental and theoretical study by Urbain *et al.* [30].

Fig. 5.3 shows σ_{10} cross sections for H^+ + H_2. The dashed curve shows a trend line through the reference data of McClure [31] and the associated grey band depicts the systematic $\pm 5\%$-uncertainty on the McClure data. The solid squares represent our measurements, which were fitted to the reference line with a single common factor. In this way for the scaling factor β a value of 1.03 ($\pm\, 0.07$)$\times$ 10^{18} cm^{-2} mbar^{-1} is determined.

The integral target density changes with the choice of gas. Therefore we also measure β for D_2, the other target gas used in the experiments, and find a value of 1.15 ($\pm\, 0.08$) $\times$ 10^{18} cm^{-2} mbar^{-1}. Here it is assumed that the cross sections for H_2 and D_2 are the same as their ionization potentials are equal and the proton velocities are rather high (0.4 - 1 a.u.) [33, 34].

5.2.4 Determination of two-electron capture contributions to the CX measurements

From Eq. 5.5 it is seen that one needs to know f, the ratio between BDC and SC, to obtain the SC cross sections. The distribution of target fragments allows for the assessment of the ratio between BDC and SC. SC [Eq. (5.1)] generates molecular ions H_2^+ of $\approx$ 0 eV. The capture of two electrons (Eqs. (5.2b), (5.2a)) leads to the dissociation of the H_2 molecule into two energetic protons of 9.7 eV. Fig. 5.4 shows two typical ToF spectra, one for Sn^{3+} and one for N^{5+} colliding on H_2. In both cases, the strongest peak is the H_2^+ peak associated with SC [cf. Eq. (5.1)]. The contribution of protons to the ToF spectrum is weak.

As can be seen in the zoom in Fig. 5.4, the proton "peak" consists of three peaks of which the central one is located at the expected ToF of H^+ fragments and represents protons of $\approx$ 0 eV stemming from gentle dissociation of H_2^+ molecular ions excited just above the dissociation limit (see e.g. [35]). The two peaks on either side of the 0-eV proton peak correspond to 9.7-eV protons from BDC where the peak at slightly shorter ToFs belongs to 9.7-eV protons emitted in the forward direction to the ToF spectrometer (H_f^+) and the one at longer ToFs is due to protons emitted backward, away from the ToF spectrometer (H_b^+). Backward emitted protons get reflected by the extraction field (see inset (a) in Fig. 5.4) into the direction of the ToF spectrometer explaining the time difference between the forward and backward emitted 9.7-eV protons. The difference in ToF (ΔT) scales with the square root of the kinetic energy release (U_{KER}) of the dissociation process (e.g. [36]) and for singly charged fragments it is given by:

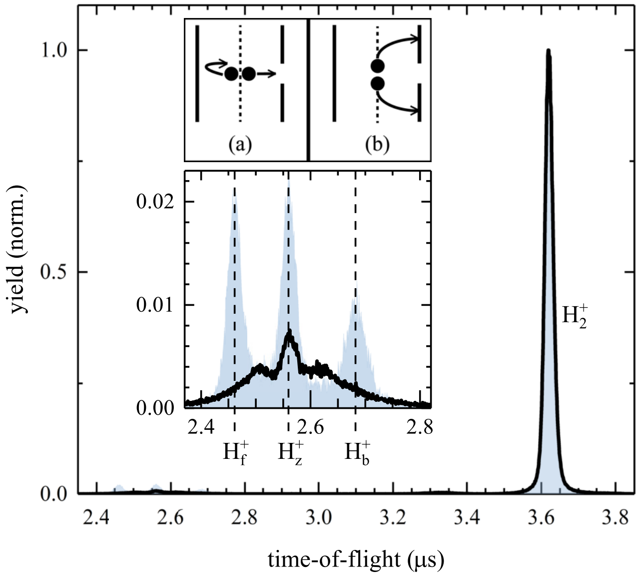

Figure 5.4: *Time-of-flight (ToF) spectra of target fragments for 48 keV Sn^{3+} (line) and 50 keV N^{5+} (fill) colliding on H$_2$. For direct comparison, the spectra are normalized to the H_2^+ peak height. The zoom shows the very weak proton peaks. Expected peak positions for 9.7-eV protons from BDC are marked by dashed lines. H_f^+ and H_b^+ refer to forward and backward emitted protons respectively. The position of 0-eV protons, H_z^+, of course lying between H_f^+ and H_b^+, is also marked by a dashed line for reference.*

$$\Delta T = \frac{\sqrt{8\,\mu\,U_{\text{KER}}}}{E}, \tag{5.7}$$

with E the extraction field (in the present experiment 40 V/cm) with the reduced mass, μ, being 0.5 and 1 for H$_2$ and D$_2$ respectively.

The 9.7-eV protons emitted along the beam axis are intercepted by the entrance diaphragm of the ToF spectrometer, see Fig. 5.4b. Therefore, in general, only 9.7-eV protons emitted in small cones towards or away from the ToF spectrometer are detected leading to the two proton peaks labeled H_f^+ and H_b^+ in Fig. 5.4, respectively. Using 50 keV N^{5+} and 60 keV O^{6+} ions colliding with H$_2$ as reference systems for which cross sections for single-electron capture and for bound and autoionizing double-electron capture have been measured [37–43], the percentage of the 9.7-eV protons that are detected in our experimental setup, α, is determined to be $(5 \pm 1)\%$.

Fig. 5.4 compares the ToF spectra, normalized to their H_2^+ peak heights, of 48 keV Sn^{3+} and 50 keV N^{5+} colliding with H_2^+. While the 9.7-eV H_f^+ and H_b^+ are very prominent for N^{5+} they are barely present for Sn^{3+}. This hints at a significantly lower double capture contribution in the case of Sn^{3+} ions than for N^{5+} for which single and double capture are of similar magnitude. Over the energy range of 10 - 50 keV, the ratio f of double-over-single capture for Sn^{3+} is determined to be $(11 \pm 4)\%$. The uncertainty in f is quite considerable due to the low intensities of the 9.7-eV H_f^+ and H_b^+ peaks. Peak areas for H_f^+ and H_b^+ are assessed by fitting Gaussian peaks to the spectrum while applying the following constraints: i) the positions and separation (223 ns) between the 9.7-eV H_f^+ and H_b^+ peaks are fixed; ii) the ratio of the 9.7-eV H_f^+ and H_b^+ peak areas is set to 1.3; and iii) the width of the H_f^+ peak is fixed at 1.5 times the width of the H_b^+ peak. The fitting constraints for the 9.7-eV H_f^+ and H_b^+ peaks, which were determined on basis of the N^{5+} and O^{6+} spectra, were also observed in numerous ToF measurements with other ions e.g. Xe^{4+}, Sn^{5+}, and Ar^{6+}.

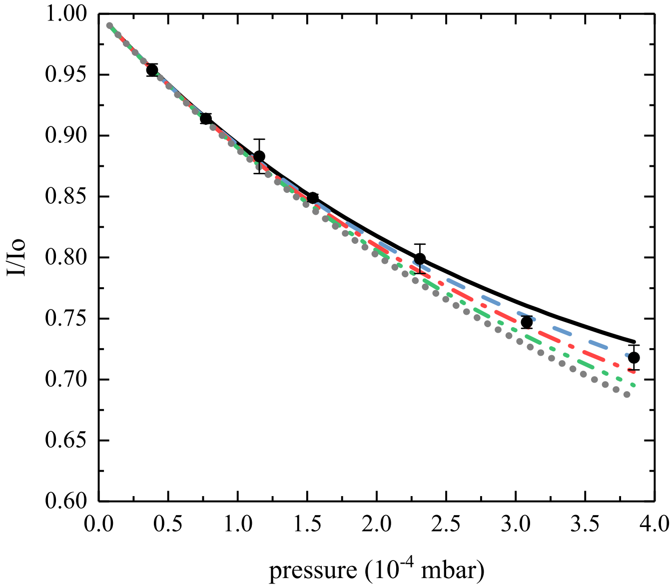

Figure 5.5: *Comparison of the measured beam current of 39 keV Sn^{3+} ions (black symbols) as a function of the H_2 target pressure with simulated results (solid curves) taking different values for the σ_{21} cross section ($Sn^{2+} \rightarrow Sn^{1+}$). For σ_{21} the following cross sections are used (in units of 10^{-16} cm^2) for the lines of different color/styles: black line = 0, blue dashed = 2.5, red dashed-dotted line = 5, green dashed-dotted-dotted line = 7.5 and grey dotted line = 10.*

5.2.5 Contributions of double collisions

Finally, it is checked that the experiments are performed in the single-collision regime by varying the target pressure over one order of magnitude. Fig. 5.5 shows as an example the dependence of the measured beam current of Sn^{3+} as a function of target pressure. In the figure, the solid curves are generated by solving Eqs. (5.3) taking only the significant cross sections namely σ_{32}, σ_{31}, and σ_{21}. The measured σ_{32} and f are used as inputs in the calculations; the multiple curves correspond to calculations taking different input values of σ_{21}. From the figure, it is seen that deviations from the single-collision approximation might start to show up at pressures of 1.5×10^{-4} mbar depending on the magnitude of the cross section for single-electron capture (σ_{21}) by Sn^{2+}. The data in Fig. 5.5 suggest a σ_{21} cross section of about 5×10^{-16} cm^2. As the data used for the final determination of the single-electron cross sections σ_{32} have been taken at 1.5×10^{-4} mbar the influence of double collisions is very small and might have been neglected. Nevertheless, we have chosen to correct the data for double collisions assuming a common σ_{21} cross section of $(5 \pm\ 5) \times 10^{-16}$ cm^2. Such inclusion of double collisions reduces the uncorrected σ_{32} cross sections by $\approx 3\%$ on average.

5.3 Theory

We have calculated the SC cross sections using a semi-classical method with nuclear straight-line trajectories. The calculation assumes that the H–H inter-nuclear distance, ρ is fixed during the collision (Franck-Condon approximation). The electronic wavefunction has been expanded in terms of seven molecular functions of the SnH_2^{3+} quasi-molecule. The molecular wavefunctions are approximate eigenfunctions of the Born-Oppenheimer electronic hamiltonian, obtained by means of a multi-reference configuration interaction method. In practice, the calculation explicitly considers the three valence electrons, which move in the field created by the H nuclei and the *ab initio* pseudopotential STUTTGART RLC ECP [44] that describes the electrons' interaction with the Sn^{4+} core. We have carried out the calculation of electronic wavefunctions by employing a three-center basis set of Gaussian-type-orbitals (GTO) that includes the $(8s, 4p) \rightarrow [3s, 2p]$ basis [45] centered on the H nuclei and a $[4s, 4p, 3d, 2f]$ basis [46] on the Sn nucleus. In a first step, we have obtained a set of molecular orbitals (MOs) in a restricted Hartree-Fock calculation in this basis for the SnH_2^{3+} system, and we have created the configuration space by allowing single and double excitations from a set of eight reference configurations. The configuration space is restricted by allowing between one and three electrons in five MOs, the first four orbitals of A′ symmetry and the first A″ MO. Up to two electrons can occupy the remaining orbitals. We have calculated the non-adiabatic couplings nu-

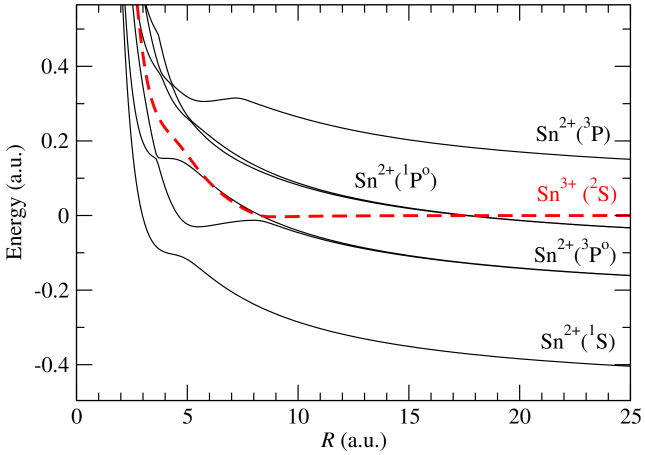

Figure 5.6: *Potential energy curves of the* $(Sn+H_2)^{3+}$ $^2A'$ *electronic states as functions of the distance from the Sn nucleus to the midpoint of the* H_2 *axis. The spectroscopic terms of the* Sn^{2+} *or* Sn^{3+} *ions in the separate atom limit are indicated in the figure.*

merically as explained in [47, 48] with a differentiation step of 10^{-4} a.u. The molecular expansion includes a common translation factor based on the switching function of Ref. [49].

The asymptotic energy differences between the entrance channel $Sn^{3+}(5s^1\ ^2S) + H_2(X\ ^1\Sigma_g^+)$ and the exit channels $Sn^{2+}(5s^2\ ^1S,\ 5s5p\ ^3P^o,\ 5s5p\ ^1P^o,\ 5p^2\ ^3P)$ have been compared with NIST data [50], after subtracting the calculated ionization potential of H_2 at the equilibrium distance ($\rho = 1.4$ a.u.). The differences with the average energies of each multiplet are smaller than 0.03 a.u.. In Fig. 5.6, we show the energies of the 7 lowest molecular states for a nuclear geometry with the angle between the vectors $\vec{R}$ ($\vec{R}$ is the position vector of the Sn nucleus with respect to the midpoint of the H-H inter-nuclear axis) and $\vec{\rho}$ equal to 60°, which has been found in previous calculations [51] to be a representative geometry that leads to cross sections in good agreement with the orientation-averaged (OA) ones. In the non-relativistic approach, only transitions to doublet states are allowed. Also, transitions to A'' are forbidden, and we have plotted only the energies of the molecular states $^2A'$. The energy of the entrance channel exhibits avoided crossings with those of the states dissociating into $Sn^{2+}(5s5p\ ^1P^o)+H_2^+(X\ ^2\Sigma_g^+)$ and $Sn^{2+}(5s5p\ ^3P^o)+H_2^+(X\ ^2\Sigma_g^+)$. The first one takes place at a very large distance, $R \approx 17.5$ a.u., and is very narrow. In practice, it is traversed diabatically, as plotted in Fig. 5.6. At not too high collision energies, the transitions in the neighborhood of the second avoided crossing, $R \approx 8.5$ a.u., furnish the main mechanism of the electron capture process. As the

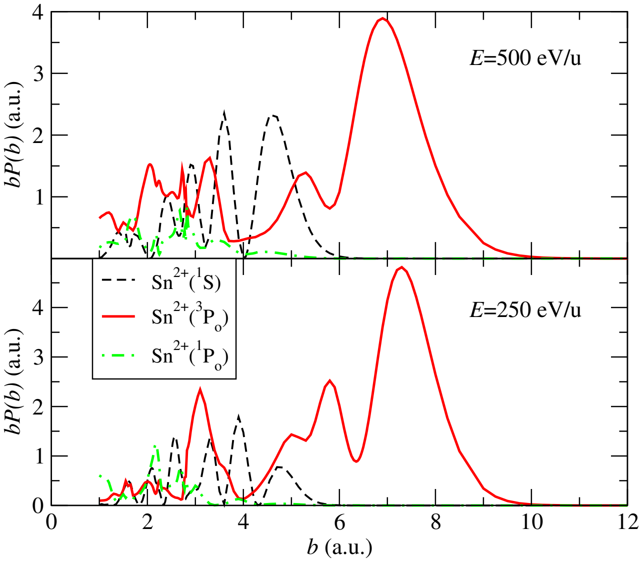

Figure 5.7: *Opacity functions for the main three CX channels at* $E = 250$ *eV/u (bottom) and* $E = 500$ *eV/u (top).*

collision energy increases, the transitions in the wide avoided crossing between the energies of the ground and the first excited state at $R \approx 5$ a.u., become more important, and are responsible for the population of the channel Sn^{2+}($5s^2\ ^1$S)+H$_2^+$($X\ ^2\Sigma_g^+$).

The numerical solution of the eikonal equation leads to the probabilities for transitions to the different capture channels, $P_k(b)$ and the corresponding integral cross sections,

$$\sigma_k = 2\pi \int_0^\infty bP_k(b)\mathrm{d}b, \tag{5.8}$$

where b is the impact parameter.

In Fig. 5.7 we plot the opacity functions, bP_k, for the electron capture into Sn^{2+}(^1S) + H$_2^+$($X^2\Sigma_g^+$), Sn^{2+}($^3P^o$) + H$_2^+$($X^2\Sigma_g^+$)and Sn^{2+}($^1P^o$) + H$_2^+$($X^2\Sigma_g^+$) for the collision energies of 250 eV/u and 500 eV/u. One can note that the charge transfer channel, Sn^{2+}($^3P^o$)+H$_2^+$($X^2\Sigma_g^+$), is populated for relatively large impact parameters, which are coherent with the predicted transitions in the avoided crossing at $R \approx 8.5\ a.u.$. At these energies, the transitions near the avoided crossing between the two first energy curves give rise to the observed transitions at $b \lesssim 5.5\ a.u.$ to the electronic state dissociating in Sn^{2+}(^1S)+H$_2^+$($X^2\Sigma_g^+$), which are more important as E decreases. On the contrary, the probabilities for capture to Sn^{2+}($^3P^o$)+H$_2^+$($X^2\Sigma_g^+$) are less important as E increases, which corresponds to a more diabatic crossing of the avoided crossing near $R \approx 8.5\ a.u.$.

More elaborate treatment of the orientation average is provided by the trajectory average where the energies and couplings are calculated along the projectile trajectory (see [29]). In the present case we have carried out cross section calculations with three trajectory orientations as explained in Ref. [52].

5.4 Results and discussion

The experimental results for Sn^{3+} colliding with H$_2$ are presented in Fig. 5.8 (solid black dots). The measured cross sections range between (25 – 50) $\times$ 10^{-16} cm^2 and increase in magnitude with decreasing ion energy. For instance, on moving down from 0.43 keV/u to 0.08 keV/u in ion energy, the cross sections increase by a factor of $\approx$ 2. The cross sections are compared to our semi-classical calculations shown by the full black curve labeled OA in Fig. 5.8. The experiments and the theory agree fairly well at higher energies but as one move towards lower impact energies, a discrepancy emerges. In the case of the calculated cross sections, the increase towards lower energy is much weaker with the cross-section increasing by only a factor of $\approx$ 1.2 on going down from 0.43 keV/u to 0.08 keV/u in impact energy. In search of the prospective cause of this discrepancy, experiments with the heavier isotopologue D$_2$ have been conducted, the results of which are given by the red solid squares in Fig. 5.8. A remarkable isotope effect is observed in the experiments. Also, the calculations, which are independent of the molecular mass, evidently show better agreement (even at lower energies) with the experiments performed with D$_2$.

At relatively high impact energies, the main difficulty of the semiclassical calculation comes from the need to perform calculations for different orientations of the molecule with respect to the projectile trajectory or, equivalently, for different trajectory orientations with respect to a fixed molecule. We show in Fig. 5.8 the cross sections calculated for three trajectory orientations (T1, T2, and T3), where T1 is a trajectory with $\boldsymbol{v} \parallel \boldsymbol{\rho}$ and $\boldsymbol{b} \perp \boldsymbol{\rho}$, T2 with $\boldsymbol{v} \perp \boldsymbol{\rho}$ and $\boldsymbol{b} \parallel \boldsymbol{\rho}$, and T3 with $\boldsymbol{v} \perp \boldsymbol{\rho}$ and $\boldsymbol{b} \perp \boldsymbol{\rho}$, with [52]

$$\sigma_{OA} = \frac{1}{3}\left[\sigma(\mathrm{T1}) + \sigma(\mathrm{T2}) + \sigma(\mathrm{T3})\right]. \tag{5.9}$$

In this system, the orientation effects are expected to be small because the main transitions take place at large inter-nuclear separations. This is confirmed by the small differences between the three orientation-dependent results, and also between the OA cross section and that obtained using the energies and couplings calculated for $\theta = 60°$ ($\approx$ 6%). It can be noted in this figure that the oscillatory behavior of the cross section is similar in all calculations. The origin of these oscillations can be traced back to the interferences between transitions in the avoided crossing at $R \approx 8.5$ a.u. and

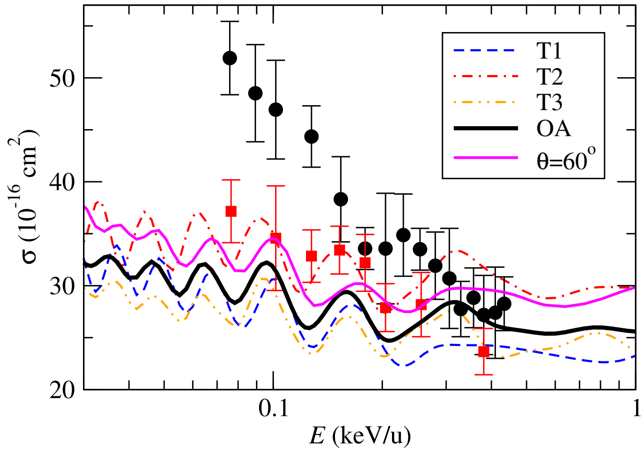

Figure 5.8: *Comparison of experimental data with different semiclassical calculations of single electron capture cross sections in* Sn^{3+} *collision with* H_2 *(black circles) and* D_2 *(red squares) as functions of the ion energy. The semiclassical results for the seven molecular states are obtained along three trajectory orientations (T1, T2, and T3) and their average (OA). The result of an isotropic calculation with the energies and couplings calculated for a fixed angle,* $60°$*, between* $\boldsymbol{v}$ *and* $\boldsymbol{\rho}$ *is also included.*

those at $R \approx 3.6$ a.u. (see Fig. 5.6), which also appear in the calculations along the trajectories T1-T3. Since the transitions take place at relatively large values of R, the oscillations are similar and they do not disappear in the OA cross section.

The seven-state molecular calculation has been carried out within the framework of the semi-classical method, which may limit the validity of the calculation at relatively low collision energies. To estimate the limitation of this approximation, we have carried out exploratory full quantal calculations with a basis set of two molecular states, those involved in the avoided crossing at $R \approx 8.5$ a.u.: $Sn^{3+}(^1S)+H_2$ and $Sn^{2+}(^3P^o)+H_2^+(^2\Sigma_g^+)$. The semi-classical and the quantal two-state calculations show good agreement in the energy region 20 eV/u $< E <$ 100 eV/u (Fig. 5.9), which indicates that the differences found with the experimental values are not due to the use of the semi-classical formalism. In this respect, one must note that in the semi-classical method, the two molecular states are coupled by the two components of the nuclear gradient in the collision plane. However, in the quantal formalism (see [30]) only the component in the radial direction is included. In Fig. 5.9, we have plotted the semi-classical cross section calculated without the coupling that comes from the gradient component perpendicular to the radial direction, which is identical to the quantal one. Therefore, trajectory and quantal effects can be neglected in the energy range of the experiment.

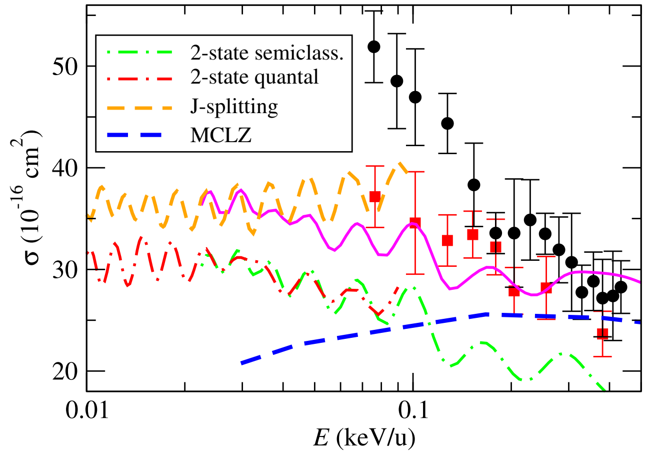

Figure 5.9: *Comparison of the isotropic seven-state semiclassical calculation with* $\theta = 60°$ *(solid pink line) with a two-state quantal calculation and a two-state semiclassical calculation without rotational couplings (dashed-dotted lines). The dashed lines are the estimates including the effect of the L-S coupling (labeled J-splitting) in a 4-state quantal calculation and in the Multi-Channel Landau-Zener (MCLZ) model. The experimental results are also included as in Fig. 5.8*

.

A second approximation of the semi-classical calculation is the neglect of the spin-orbit coupling. An estimate of the influence of this effect is obtained in both the quantal and the Multi-Channel Landau-Zener (MCLZ) calculations with the Hamiltonian matrix elements given by the formulae of Ref. [53] and adding the asymptotic splitting of the $Sn^{2+}(^3P^o)$ term [50] to the diagonal matrix elements. The ensuing cross section has similar values to the experimental ones for $E > 0.2$ keV/u, but it decreases at lower energies. To further check this model, we have carried out a similar estimate by performing a 4-state quantal calculation with the numerical H data previously employed in the 2-state calculation and adding the asymptotic L-S splitting at all ion-molecule separations. At low energies, the cross section is dominated by transitions at large R to the highest state with $J = 2$ and it is increased with respect to that from the 2-state calculation by up to 10%, because the avoided crossing is moved to a larger R as a consequence of the energy shift. For $E > 500$ eV/u (not shown in Fig. 5.9), the model cross section shows an increase that is due to transitions to the lowest level ($J = 0$) that take place at smaller R, where the approximation of keeping the 2-state interaction is not valid. We have also carried out a numerical experiment by integrating numerically the matrix elements of Ref. [53] with the asymptotic splitting, as in the MCLZ estimate. For the sake of clarity, the results are not included in Fig. 5.9; they are similar to those using the numerical data, but without the oscillations, because the matrix elements of Ref. [53] do not include the modeling of the inner avoided crossing.

Finally, the increasing difference between the experimental cross sections for collisions with H_2 and D_2, as energy decreases, can be due to vibrational effects. In this respect, a similar isotopic dependency was found in the experiment of Kusakabe *et al.* [33] for H^++(H_2, D_2). It is expected that the Franck-Condon calculation shows better agreement with D_2 data than with H_2 because it assumes that the target bond length remains fixed during the collision and this is a more realistic description for D_2 than for H_2, given that the larger reduced mass of the first is linked to a more localized initial vibrational wavefunction. Nevertheless, as the collision energy decreases, the vibrational effects will also start to be relevant for D_2 and we expect that the OA Franck-Condon calculation will not be valid for D_2 at energies below the experimental ones. Calculations of charge transfer beyond the Franck-Condon approximation [34] for H^++(H_2, D_2) found indeed good agreement with experiments for both isotopic targets.

5.5 Conclusion

In this work we have presented both an experimental determination and a theoretical calculation of the absolute single electron capture cross section for Sn^{3+} on H_2 in the energy range 1-100 keV. The experiments are based on measuring a reduction in ion beam current due to the charge exchange interaction. The calculations are done in a semi-classical way using molecular orbitals. At the higher energies, there is a fair agreement between the experimentally determined and the theoretically calculated values. However, the experimental cross sections show a considerable increase towards lower energies, whereas this effect is only weakly present in the calculated values. Exploratory full quantal calculations have been performed and these show good agreement with the semi-classical calculations. From this, we conclude that the discrepancy is not due to the invalidity of the semi-classical approach in our energy regime. The effect of spin-orbit coupling has been found to be small ($\approx 15\%$) and it does not explain the rise of the cross section for the collision with H_2 at $E < 200$ eV/u. The experiments have also been performed for the heavier isotopologue D_2 and show a less strong increase of cross section towards the lower energies and are in good agreement with the semiclassical Franck-Condon calculations. This leads us to conclude that the increase for H_2 is due to vibrations in the target molecule. This effect is weaker in D_2 because of the higher mass and it is not included in the calculations, which make use of the Franck-Condon approximation.

5.6 Acknowledgment

The experimental work was carried out at the ZERNIKELEIF facility in the Zernike Institute for Advanced Materials of the University of Groningen as part of the research portfolio of the Advanced Research Center for Nanolithography, a public-private partnership between the University of Amsterdam, the Vrije Universiteit Amsterdam, the Dutch Research Council (NWO), and the semiconductor equipment manufacturer ASML. The theoretical work of IR and LM was partially supported by Ministerio de Economía and Competitividad (Spain), project no. FIS2017-84684-R. The computational support by the Centro de Computación Científica of UAM is also acknowledged.

Bibliography

[1] R. Geller, Rev. Sci. Instrum. **69**, 1302 (1998).

[2] R. K. Janev and H. Winter, Phys. Rep. **117**, 265 (1985).

[3] M. Barat and P. Roncin, J. Phys. B: At. Mol. Opt. Phys **25**, 2205 (1992).

[4] W. Fritsch and C. D. Lin, Phys. Rep. **202**, 1 (1991).

[5] I. Čadež, J. B. Greenwood, J. Lozano, R. J. Mawhorter, M. Niimura, S. J. Smith, and A. Chutjian, J. Phys. B: At. Mol. Opt. Phys. **36**, 3303 (2003).

[6] J. Simcic, D. R. Schultz, R. J. Mawhorter, I. Čadež, J. B. Greenwood, A. Chutjian, C. M. Lisse, and S. J. Smith, Phys. Rev. A **81**, 062715 (2010).

[7] I. Y. Tolstikhina, M. S. Litsarev, D. Kato, M-Y. Song, J-S. Yoon, and V. P. Shevelko, J. Phys. B: At. Mol. Opt. Phys. **47** (2014).

[8] V. I. Azarov and Y. N. Joshi, J. Phys. B: At. Mol. Opt. Phys. **26**, 3495 (1993).

[9] R. D'Arcy, H. Ohashi, S. Suda, H. Tanuma, S. Fujioka, H. Nishimura, K. Nishihara, C. Suzuki, T. Kato, F. Koike, J. White, and G. O'Sullivan, Phys. Rev. A **79**, 042509 (2009).

[10] A. Windberger, F. Torretti, A. Borschevsky, A. Ryabtsev, S. Dobrodey, H. Bekker, E. Eliav, U. Kaldor, W. Ubachs, R. Hoekstra, J. R. Crespo López-Urrutia, and O. O. Versolato, Phys. Rev. A **94**, 012506 (2016).

[11] F. Torretti, A. Windberger, A. Ryabtsev, S. Dobrodey, H. Bekker, W. Ubachs, R. Hoekstra, E. V. Kahl, J. C. Berengut, J. R. C. López-Urrutia, and O. O. Versolato, Phys. Rev. A **95**, 042503 (2017).

[12] J. Scheers, C. Shah, A. Ryabtsev, H. Bekker, F. Torretti, J. Sheil, D. A. Czapski, J. C. Berengut, W. Ubachs, J. R. Crespo López-Urrutia, R. Hoekstra, and O. O. Versolato, Phys. Rev. A **101**, 062511 (2020).

[13] N. Badnell, A. Foster, D. Griffin, D. Kilbane, M. O'Mullane, and H. Summers, J. Phys. D: Appl. Phys. **44**, 135201 (2011).

[14] A. Borovik Jr, M. F. Gharaibeh, P. M. Hillenbrand, S. Schippers, and A. Müller, J. Phys. B: At. Mol. Opt. Phys. **46**, 175201 (2013).

[15] G. G. van Eden, T. W. Morgan, D. U. B. Aussems, M. A. van den Berg, K. Bystrov, and M. C. M. van de Sanden, Phys. Rev. Lett. **116**, 135002 (2016).

[16] R. E. Nygren and F. L. Tabarés, Nucl. Mater. Energy **9**, 6 (2016).

[17] G. G. Eden, V. Kvon, M. C. M. van de Sanden, and T. W. Morgan, Nat. Commun. **8**, 192 (2017).

[18] G. O'Sullivan, B. Li, R. D'Arcy, P. Dunne, P. Hayden, D. Kilbane, T. McCormack, H. Ohashi, F. O'Reilly, P. Sheridan, E. Sokell, C. Suzuki, and T. Higashiguchi, J. Phys. B: At. Mol. Opt. Phys. **48**, 144025 (2015).

[19] W. Svendsen and G. O'Sullivan, Phys. Rev. A **50**, 3710 (1994).

[20] V. Bakshi, ed., *EUV Lithography*, 2nd Edition ed. (SPIE Press, 2018).

[21] O. O. Versolato, Plasma Sources Sci. Technol. **28**, 083001 (2019).

[22] V. Y. Banine, K. N. Koshelev, and G. H. P. M. Swinkels, J. Phys. D: Appl. Phys. **44**, 253001 (2011).

[23] I. Fomenkov, D. Brandt, A. Ershov, A. Schafgans, Y. Tao, G. Vaschenko, S. Rokitski, M. Kats, M. Vargas, M. Purvis, R. Rafac, B. La Fontaine, S. De Dea, A. LaForge, J. Stewart, S. Chang, M. Graham, D. Riggs, T. Taylor, M. Abraham, and D. Brown, Adv. Opt. Technol. **6**, 173 (2017).

[24] F. Torretti, J. Sheil, R. Schupp, M. M. Basko, M. Bayraktar, R. A. Meijer, S. Witte, W. Ubachs, R. Hoekstra, O. O. Versolato, A. J. Neukirch, and J. Colgan, Nat. Commun. **11**, 2334 (2020).

[25] A. Bayerle, M. J. Deuzeman, S. van der Heijden, D. Kurilovich, T. de Faria Pinto, A. Stodolna, S. Witte, K. S. E. Eikema, W. Ubachs, R. Hoekstra, and O. O. Versolato, Plasma Sources Sci. Technol. **27**, 045001 (2018).

[26] D. J. Hemminga, L. Poirier, M. M. Basko, R. Hoekstra, W. Ubachs, O. O. Versolato, and J. Sheil, Plasma Sources Sci. Technol. **30**, 105006 (2021).

[27] L. Poirier, A. Bayerle, A. Lassise, F. Torretti, R. Schupp, L. Behnke, Y. Mostafa, W. Ubachs, O. O. Versolato, and R. Hoekstra, Appl. Phys. B **128**, 1 (2022).

[28] R. F. Welton, T. F. Moran, and E. W. Thomas, J. Phys. B: At. Mol. Opt. Phys. **24**, 3815 (1991).

[29] I. Rabadán and L. Méndez, J. Phys.: Conf. Series **875**, 012009 (2017).

[30] X. Urbain, N. de Ruette, V. M. Andrianarijaona, M. F. Martin, L. Fernández Menchero, L. F. Errea, L. Méndez, I. Rabadán, and B. Pons, Phys. Rev. Lett. **111**, 203201 (2013).

[31] G. W. McClure, Phys. Rev. **148**, 47 (1966).

[32] Y. Nakai, T. Shirai, T. Tabata, and R. Ito, At. Data Nucl. Data Tables **37**, 69 (1987).

[33] T. Kusakabe, L. Pichl, R. J. Buenker, M. Kimura, and H. Tawara, Phys. Rev. A **70**, 052710 (2004).

[34] L. F. Errea, L. Fernández, L. Méndez, B. Pons, I. Rabadán, and A. Riera, Phys. Rev. A **75**, 032703 (2007).

[35] S. Martínez, G. Bernardi, P. Focke, A. D. González, and S. Suárez, J. Phys. B: At. Mol. Opt. Phys. **36**, 4813 (2003).

[36] H. O. Folkerts, F. W. Bliek, M. C. de Jong, R. Hoekstra, and R. Morgenstern, J. Phys. B: At. Mol. Opt. Phys. **30**, 5833 (1997).

[37] D. H. Crandall, M. L. Mallory, and D. C. Kocher, Phys. Rev. A **15**, 61 (1977).

[38] D. Dijkkamp, D. Ciric, E. Vileg, A. de Boer, and F. J. de Heer, J. Phys. B: Atom. Mol. Phys. **18**, 4763 (1985).

[39] M. Mack and A. Niehaus, Nucl. Instr. and Meth. B **23**, 109 (1987).

[40] M. Mack, Nucl. Instr. and Meth. B **23**, 74 (1987).

[41] R. A. Phaneuf, I. Alvarez, F. W. Meyer, and D. H. Crandall, Phys. Rev. A **26**, 1892 (1982).

[42] G. Lubinski, Z. Juhász, R. Morgenstern, and R. Hoekstra, J. Phys. B: At. Mol. Opt. Phys. **33**, 5275 (2000).

[43] J. R. Machacek, D. P. Mahapatra, D. R. Schultz, Yu. Ralchenko, A. Chutjian, J. Simcic, and R. J. Mawhorter, Phys. Rev. A **90**, 052708 (2014).

[44] A. Bergner, M. Dolg, W. Küchle, H. Stoll, and H. Preuß, Mol. Phys. **80**, 1431 (1993).

[45] P.-O. Widmark, P.-Å. Malmqvist, and B. O. Roos, Theor. Chim. Acta **77**, 291 (1990).

[46] J. M. L. Martin and A. Sundermann, J. Chem. Phys. **114**, 3408 (2001).

[47] J. F. Castillo, L. F. Errea, A. Macías, L. Méndez, and A. Riera, J. Chem. Phys. **103**, 2113 (1995).

[48] L. F. Errea, L. Fernández, A. Macías, L. Méndez, I. Rabadán, and A. Riera, J. Chem. Phys. **121**, 1663 (2004).

[49] L. F. Errea, L. Méndez, and A. Riera, J. Phys. B: Atom. Mol. Phys. **15**, 101 (1982).

[50] A. Kramida, Yu. Ralchenko, J. Reader, and and NIST ASD Team, NIST Atomic Spectra Database (ver. 5.3), [Online]. Available: `http://physics.nist.gov/asd` [2016, February 2]. National Institute of Standards and Technology, Gaithersburg, MD. (2015).

[51] L. F. Errea, A. Macías, L. Méndez, I. Rabadán, and A. Riera, Int. J. Mol. Sci. **3**, 142 (2002).

[52] L. F. Errea, J. D. Gorfinkiel, A. Macías, L. Méndez, and A. Riera, J. Phys. B: At. Mol. Opt. Phys. **30**, 3855 (1997).

[53] M. Kimura, T. Iwai, Y. Kaneko, N. Kobayashi, A. Matsumoto, S. Ohtani, K. Okuno, S. Takagi, H. Tawara, and S. Tsurubuchi, J. Phys. Soc. Jpn **53**, 2224 (1984).

Chapter 6

Evidence of the production of keV Sn^{+} ions in the H_2 buffer gas surrounding an EUV source based on a laser-produced Sn plasma

Abstract

Charge-state-resolved kinetic energy spectra of Sn ions ejected from a laser-produced plasma (LPP) of Sn have been measured at different densities of the H_2 buffer gas surrounding a micro-droplet LPP. In the absence of H_2, energetic keV Sn ions with charge states ranging from 4+ to 8+ are measured. For the H_2 densities used in the experiments no appreciable stopping or energy loss of the ions is observed. However, electron capture by Sn ions from H_2 results in a rapid shift towards lower charge states. At the highest H_2 pressure of 6×10^{-4} mbar, only Sn^{2+} and Sn^{+} ions are measured. The occurrence of Sn^{+} ions is remarkable due to the endothermic nature of electron capture by Sn^{2+} ions from H_2. To explain the production of keV Sn^{+} ions, it is proposed that their generation is due to electron capture by metastable Sn^{2+*} ions. The gateway role of metastable Sn^{2+} is underpinned by model simulations using atomic collision cross sections to track the charge states of Sn ions while traversing the H_2 buffer gas.

6.1 Introduction

Sources of extreme ultraviolet (EUV) light are based on laser-produced plasma (LPP) of high temperatures (up to 50 eV) and free electron densities (10^{19-21} cm^{-3}) in which highly charged ions are produced that are the atomic sources of the EUV radiation [1, 2]. For nanolithographic tools, the EUV wavelength of choice is 13.5 nm,

---

This chapter forms the basis for the following manuscript: S. Rai, L. Poirier, K. I. Bijlsma, E. de Wit, L. Assink, A. Lasisse, I. Rabadán, L. Méndez, J. Sheil, O. O. Versolato, and R. Hoekstra, *Evidence of the production of keV Sn^{+} ions in the H_2 buffer gas surrounding an EUV source based on a laser-produced Sn plasma*, submitted to Plasma Source Sci. Techonol.

which is dictated by the existence of high reflectivity multilayer optics [3, 4]. The element of choice for plasma generation of 13.5 nm radiation is Sn. Over a broad range of charge states (9+ to 15+), singly, doubly, and triply excited electronic configurations emit around 13.5 nm [5].

Subsequent to the desired production of EUV radiation, the plasma expands and generates energetic Sn ions [6], which if impacting on the EUV collector optics may affect the lifetime of the optics. The energy and charge state distributions of Sn ions coming from the LPP contain information on the expansion dynamics of the plasma itself [7–11]. Moreover, accurate data on the energy distributions facilitate the determination of the fraction of the total energy that is carried by the plasma ions [12].

Typically, the energy spectrum of the emitted Sn ions peaks at a few keV with tails that may extend to tens of keV [11], except for Sn^+ and Sn^{2+} which are barely observed at higher energies above 0.5 keV. When the LPP is embedded in a stopping gas, only singly and doubly charged Sn ions are observed at much lower energies, which is a direct signature of charge exchange and collisional stopping, energy transfer from the Sn particles to the stopping gas. In this paper, we address the initial stage of the charge and energy redistribution in which charge exchange is active but the energy loss to the stopping gas is still negligible. This separation can be made if the cross sections for charge exchange are much larger than the ones for significant kinetic-energy transfer. For Sn^{q+} ions with $q \geq 3$ this assumption is not debated but in the case of 1+ and 2+ ions, the charge transfer cross sections for the reactions

$$\mathrm{Sn}^{2+} + \mathrm{H}_2 \rightarrow \mathrm{Sn}^{+} + \mathrm{H}_2^{+}, \tag{6.1}$$

and

$$\mathrm{Sn}^{+} + \mathrm{H}_2 \rightarrow \mathrm{Sn} + \mathrm{H}_2^{+}, \tag{6.2}$$

are conventionally expected to be negligible because of the low scaled kinetic energies of the Sn ions ($\ll$ 100 eV/u) and the considerable endothermicity of the reactions. The Franck Condon ionization potential of H_2 is 16.1 eV [13, 14], while the ionization potentials of Sn^+ and Sn are 14.6 eV and 7.4 eV [15], respectively. Thus, resonant electron capture by Sn^{2+} is endothermic by 1.5 eV and in the case of Sn^+ by no less than 8.7 eV.

Remarkable enough while indeed no appreciable signs of charge transfer by singly charged Sn ions (Eq. (6.2)) are found we will show efficient production of Sn^+ ions out of the population of doubly charged Sn ions. Based on all available data the case is made that the Sn^{+} ions are produced by electron capture by metastable Sn^{2+*} ions in the excited [Kr]$4d^{10}5s5p$ $^{3}P_{J}$ terms (the ground state of Sn^{2+} is [Kr]$4d^{10}s^{2}$ $^{1}S_{0}$).

From an EUV source perspective, the actual abundances of singly and doubly charged Sn ions and thus, whether Sn^{2+} ions get converted by electron capture into Sn^{+}, impacts the Sn ion mitigation because the penetration depth of the Sn ions into the H_2 buffer gas depends on the stopping cross sections and recent stopping measurements [16] hint at appreciably larger stopping powers for Sn^{+} than for Sn^{2+} ions.

This paper is organized as follows. First, the laser-produced plasma source installed at ARCNL is briefly introduced with emphasis on the methods used to measure the charge-state dependent energy distributions of Sn^{q+} ions coming from the expanding LPP plasma. Thereafter the energy distributions as a function of the H_2 buffer gas are presented with a focus on the Sn^{+} ions, which present the evidence of the occurrence of charge exchange by Sn^{2+} ions. Finally based on potential-energy curves and Landau-Zener type calculations it is discussed that electron capture from H_2 by metastable $Sn^{2+*}(^{3}P_{J})$ ions is exothermic and likely to happen given the production of metastable $Sn^{2+*}(^{3}P)$ in collisions of Sn^{3+} on H_2.

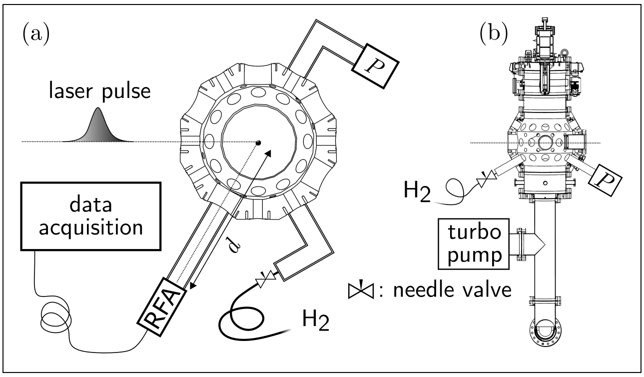

Figure 6.1: *Schematic view of the LPP experiment to measure charge-state-specific ion spectra as a function of the pressure of the H_2 buffer gas embedding the LPP plasma. The distance d from plasma to the RFA type ion detector is 68.5 cm.*

6.2 Experiment: methodology and data

The LPP EUV source used for the present set of experiments has been described in detail before [17]. The parts and features most relevant to this work are briefly recalled here.

A tin reservoir, which is kept at a temperature of 260°C, is mounted on top of a vacuum chamber with a background vacuum of 10^{-7} mbar. In the H_2 buffer gas runs, molecular hydrogen pressures covering the range from 6×10^{-5} to 6×10^{-4} mbar have been used. At a repetition rate of 25 kHz droplets of pure, molten tin are pushed through a nozzle into the vacuum chamber. The stream of microdroplets with a diameter of 27 μm, first traverse a light sheet generated by a He-Ne laser. After frequency down-conversion to 10 Hz, the light scattered off the Sn droplets is used to trigger a 10-Hz Nd:YAG laser which creates the Sn plasma. The Nd:YAG laser system is operated at a wavelength of 1064 nm and produced pulses of approximately 10 ns full-width at half-maximum (FWHM). The beam, having a Gaussian spatial profile, is focused to a spot of 100 μm FWHM onto the droplets in the center of the chamber. The laser pulse energy can be tuned without affecting the spatial beam profile by using a half-wave plate and a thin-film polarizer. A laser pulse energy of 200 mJ has been used unless stated otherwise.

The energy distributions of the Sn^{q+} ions from the LPP are measured with an RFA (retarding field analyzer), more specifically a 4-grid Kimball Physics FC-73 RFA. The RFA is positioned at a distance of 68.5 cm from the LPP and at an angle of 64° cf. figure 6.1. The RFA is absolutely calibrated against an open, grid-less Faraday cup [18] to establish the integral transmission of the four grids. The same "bottom-up" method as introduced by Poirier *et al.* [19] is used to extract the kinetic-energy distributions for each individual charge state of tin ions from their joint overlapping energy distributions.

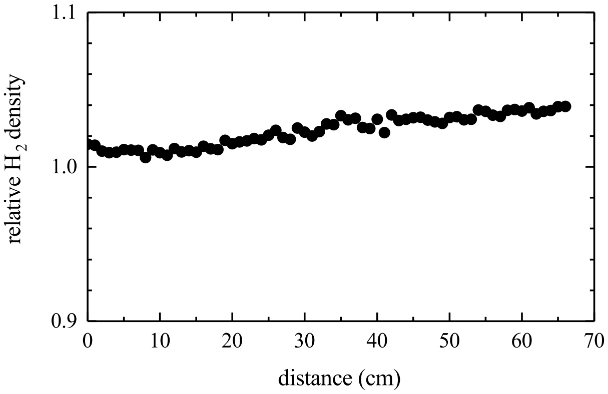

Figure 6.2: *MOLFLOW Monte Carlo simulation results of the relative H_2 density, with respect to the density at the position of the pressure gauge, along the ejected Sn^{q+} ions' path from the laser-produced plasma in the center of the vacuum chamber to the RFA detector, positioned at 68.5 cm from the center.*

To interpret the ion energy spectra as a function of the H_2 pressure, one needs to

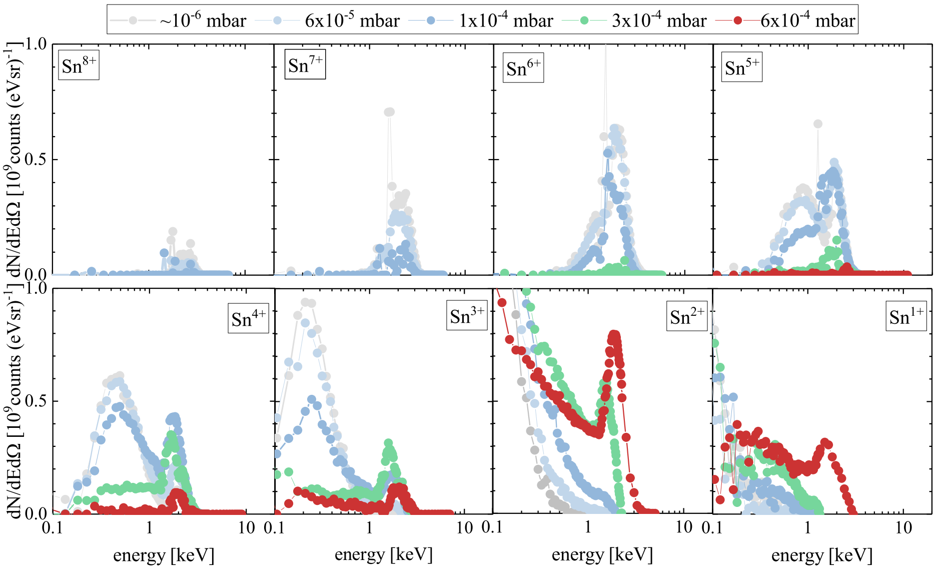

Figure 6.3: *The yield of Sn^{q+} ions as a function of their kinetic energy in case of no H_2 gas and for H_2 buffer gas pressures in the range $6{\times}10^{-5}$ to $6{\times}10^{-4}$ mbar. The ions' flight path through the buffer gas is 68.5 cm.*

know the relation between the pressure measured at the pressure gauge and the pressure (H_2 density) along the ions' trajectory from the laser-produced plasma to the ion detector. With the Monte-Carlo package MOLFLOW+ [20] developed at CERN, we have simulated the H_2 density within the entire LPP vacuum chamber and all its additional vacuum tubing and equipment. The simulated H_2 density along the ions' path from source to RFA detector is shown in figure 6.2. Along the ion path, the average relative H_2 density is seen to be almost 3% higher than the density at the position of the pressure gauge and to change by a few percent only over the full distance of 68.5 cm. Therefore, the largest uncertainty in the H_2 density does stem from the absolute calibration of the pressure gauge, which is given by the manufacturer as 30%.

Sn ions in charge states up to 8+ are observed in the RFA measurements. The energy distributions for all eight charge states are presented in figure 6.3 for 5 different H_2 pressures. Note that the results labeled $1\times\,10^{-6}$ mbar are the reference measurements with no H_2 gas surrounding the LPP plasma. The main points to be noted before entering the detailed discussion in the next section is that the spectra of Sn^{8+}, Sn^{7+}, and Sn^{6+} are rather narrow , peak at approximately 2 keV and disappear with increasing H_2 pressure. In the absence of H_2 gas the spectra of Sn^{3+}, Sn^{2+}, and

Sn^{1+}, extend upto energies of maximally 1 keV for Sn^{3+} and $\approx$ 0.7 keV for Sn^{2+} and Sn^{1+}. With increasing H_2 pressures a peak at 2 keV, similar to the 2-keV peak characterizing the Sn^{8+}, Sn^{7+}, and Sn^{6+} spectra, grows in into the Sn^{3+}, Sn^{2+}, and Sn^{1+} spectra. Therefore the keV ions of Sn^{3+}, Sn^{2+}, and Sn^{+} observed in the energy spectra taken with a H_2 stopping gas around the LPP plasma must originate from Sn^{q+} ions with $q \geq 4$ by means of consecutive electron capture reactions. Last but not least the occurrence of energetic ($E \leq 1$ keV) Sn^{1+} ions with increasing H_2 pressure is a clear sign that one-electron capture by Sn^{2+} eq. 6.1 is not blocked by the anticipated endothermicity of the reaction and moreover even has a significant cross section.

6.3 Discussion

Before addressing the above points, it is to be realized that the experiments are performed at pressures mimicking the earliest stages of the trajectories of Sn ions in the H_2 buffer gas after being ejected from the LPP plasma. In this first phase, charge-exchange processes bringing the average charge state of the ions rapidly down are active and play their part before the ions have undergone appreciable energy loss. The validity of this approximation is implicit in the charge-state dependent energy spectra shown in figure 6.3 in which the high energy peak that emerges with increasing H_2 pressure in the spectra of the low charge state Sn ions is found at the same energy as the peaks disappearing from the spectra of the high charge state Sn ions.

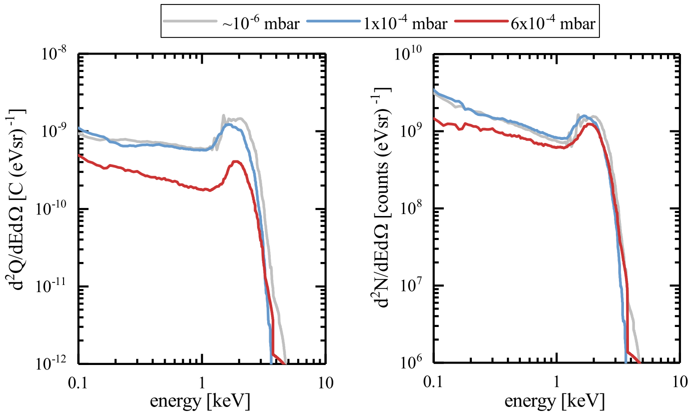

Figure 6.4: *Left panel: Total amount of charge per eV as a function of Sn ion energy. Right panel: Total number of ions per eV as a function of Sn ion energy. Results are presented for no H_2 buffer gas present (labeled 1×10^{-6} mbar) and buffer gas pressures of 1×10^{-4} and 6×10^{-4} mbar. The path length through the buffer gas is 68.5 cm.*

The reduction of average charge state without significant energy loss is demonstrated in figure 6.4. Figure 6.4 shows in its left panel the total charge as a function of energy, while the right panel presents the number of particles as a function of energy. In the peak range (1- 5 keV) the amount of charge measured at the RFA drops by approximately a factor of 4 when the H_2 pressure is raised to 1×10^{-3} mbar. In contrast to that the number of keV Sn ions detected has not changed appreciably. Therefore the assumption of charge transfer processes dominating the initial changes in the charge-state dependent energy distributions appears valid.

The pressure dependence of the particle-number distributions for all charge states from $q = 8$ down to $q = 1$ can be tracked by a set of 8 differential equations of the type:

$$dN^{q+} = n\sigma_{q+1\to q}N^{(q+1)+}dl - n\sigma_{q\to q-1}N^{q+}dl \tag{6.3}$$

with N^{q+} the number of Sn ions in charge state $q+$, n the H_2 target density, $\sigma_{q\to q-1}$ the cross section for charge exchange from charge state $q+$ to $(q-1)+$, and dl the integration step along the ion's trajectory. With the exception of Sn^{3+} [21], no charge exchange data is available for Sn^{q+} ions colliding on H_2. Therefore we decided to use the classical over-the-barrier model [22–24] to get estimates for $\sigma_{q\to q-1}$ cross sections for charge states of $q \geq 4$, i.e, 62, 76, 88, 100, and 112 ($\times10^{-16}$ cm^2) for 4+, 5+, 6+, 7+, and 8+ Sn ions, respectively. It is of note that the over-the-barrier model calculates a maximum cross section as it assumes that for impact parameters smaller than the capture distance capture happens with 100% probability, therefore the values represent maximum cross sections. The results of a particle-number simulation are shown in figure 6.5, for the endothermic charge-transfer reaction of Sn^{2+} ions a small non-zero cross section of 0.1×10^{-16} cm^2 has been used. In line with the experimental data for energetic Sn ions (E$\geq$ 1 keV) (see figure 6.3) the number-densities of energetic Sn ions swaps from $q \geq 4$ to $q < 3$ over the pressure range of 10^{-4} to 10^{-3} mbar. Although, in contrast to the LPP data barely any Sn^+ ions are predicted. The experiments show already a considerable (20%) fraction of 1+ ions at a pressure 6×10^{-4} mbar.

As mentioned before the experiments are performed in an integral density regime in which no appreciably stopping occurs and thus given that Sn^+ ions have larger stopping cross sections than Sn^{2+} ions [16] it is of importance for stopping modeling to understand how energetic Sn^{2+} get converted to Sn^+ ions (eq. 6.1). The necessary electron-capture reaction is an endothermic reaction, which has small cross sections, e.g. [25], while large cross sections are required to produce significant fractions of Sn^+ ions at pressures well below 10^{-3} mbar. For an electron-capture reaction to have a significant cross-section, the potential energy curves of the initial and final channels

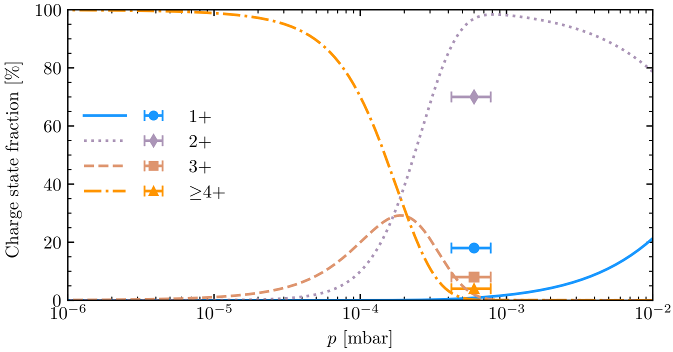

Figure 6.5: *Simulated charge state distributions of energetic* Sn^{q+} *ions detected at a distance of 68.5 cm from the LPP plasma as a function of* H_2 *buffer pressures. For* $q \geq 4$ *the actual* q *specific fractions as measured at* p*=*10^{-6} *mbar (see figure 6.3) were used as input in solving the set of differential equations.*

are required to cross one another at a specific internuclear distance between the ion and the target. A very simplified picture of the most relevant potential energy curves for Sn^{2+} - H_2 collisions is sketched in figure 6.6.

In figure 6.6, the electronic potential energy of ground state $Sn^{2+}(5s^2\ ^1S)$ and H_2 is taken as reference for all other channels. As mentioned in the introduction the electron-capture channel $Sn^{1+}(5s^25p\ ^2P)$ + H_2^+ is endothermic by 1.5 eV at infinite internuclear distance between the particles. At shorter distances, due to the Coulomb repulsion between Sn^+ and H_2^+ the difference between both curves increases, and thus both potential energy curves do not cross underpinning the original idea of electron capture being very unlikely. More explicitly, one-electron capture from H_2 by ground state $Sn^{2+}(5s^2\ ^1S)$ is very unlikely at low energies (E $\leq$ 1 keV/u).

For metastable Sn^{2+} $(5s5p\ ^3P)$ ions the situation is very different. The Sn^{2+} $(5s5p\ ^3P)$ term is excited by some 7 eV (weighted average of the excitation energies of the J = 0, 1, and 2 levels of 6.64, 6.84, 7.34 eV, respectively [15]) and thus lies about 7 eV above the ground state potential energy curve. Therefore at an internuclear distance R_c, there exists a curve crossing with the electron capture channel near 6 a.u., cf. figure 6.6. Using this distance, one might estimate using the "absorbing sphere" approximation [26, 27] a maximum cross section of 3×10^{-15} cm^2 $(0.45\,\pi\, R_c^2)$. This cross section is of similar size as the one for Sn^{3+} - H_2 collisions [21], which indicates that one-electron capture by metastable Sn^{2+} ions is a potential gateway to produce singly charged Sn^+ ions.

Metastable Sn^{2+*} ions as a source for the production of Sn^+ ions by means of electron

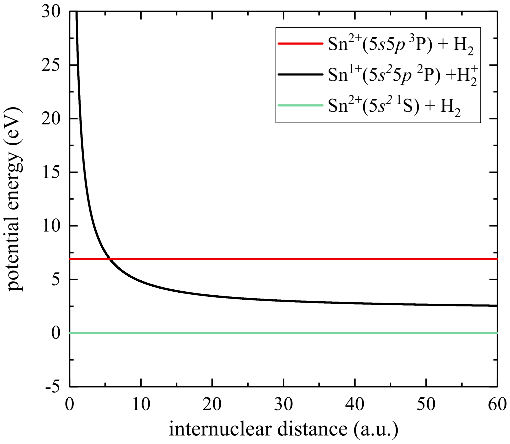

Figure 6.6: *Potential energy curves of relevant electronic channels in Sn*$^{2+}$ *- H*$_2$ *collisions as a function of internuclear distance.*

capture requires obviously a large abundance of metastable Sn^{2+*} ions. In keV collisions of Sn^{3+} ions on H$_2$ electron capture populates directly and almost solely the metastable Sn^{2+}($5s5p$ ^{3}P) term [21]. As shown above, all keV Sn ions of high charge state get rapidly converted to Sn^{3+} ions and which by subsequent charge transfer do create metastable Sn^{2+*} ions. Metastable Sn^{2+*} are therefore abundantly produced in the stopping gas.

Transitions from the populated metastable $5s5p$ ^{3}P$_{0,1,2}$ levels to the ground state $5s^2$ ^{1}S are spin forbidden, however, are their lifetimes long enough with respect to the time between subsequent collisions? For J=0 and 2, the transitions are also symmetry forbidden and thus the levels are expected to be very long-lived. While the J=0 to $J' = 0$ is truly forbidden, the $J = 2$ to $J' = 0$ transition might still have a small transition probability [28]. To get an order of magnitude estimate of the lifetime of the $J = 2$ level, we performed a basic FAC (Flexible Atomic Code [29]) calculation. The calculation predicts a lifetime of almost 100 s. This is very long compared to typical flight times in the experiment which are in the range of a few to a few tens of μs. For a heavy species as Sn where the spin-orbit coupling is very significant, the J=1 level is expected to have by far the shortest lifetime of the three levels of ^{3}P term as it requires a ΔJ=1 transition to the ground state. For the ^{3}P$_1$ theoretical lifetimes are reported of approximately 100 [30], 150 [31] and 200 ns [32]. In a beam foil experiment, [33] the decay was not observed indicating that the lifetime is much longer than 45 ns, consistent with the theoretical values.

During a period of one lifetime of 150 ns (average of the reported values), a 2 keV

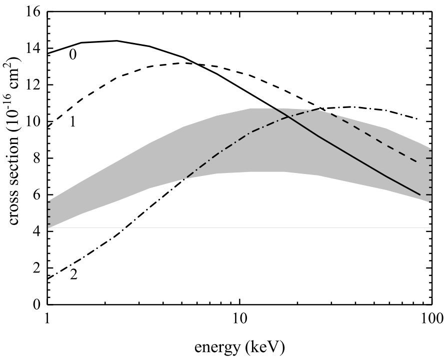

Figure 6.7: *Cross sections for one-electron capture in 1 to 100 keV* $Sn^{2+}(5s5p\ ^3P_J)$ *collisions with* H_2 *from Landau-Zener model calculations for each of the* ^3P *J levels. The grey band indicates the (2J+1) weighted average cross section, with the top of the band given by the full contribution of the J=1 level, and the bottom of the band is defined by no contribution from J=1.*

Sn particle travels a distance of approximately 0.8 cm. For a first estimation of the role of J=1 metastables, we take three times the lifetime, a period after which 95% of the J=1 metastables has decayed to the ground state. The associated flight path of the 2 keV Sn particle is 2 cm. This path length should be compared to the mean free path (λ_F) of the particles which is equal to $(n\sigma_{21})^{-1}$. For the highest pressure used here of 10^{-3} mbar (2.4×10^{13} H_2 molecules per cm^3) and an σ_{21} of 10×10^{-16} cm^2 (discussed in the next paragraphs) one finds $\lambda_F \approx 40$ cm. Therefore only about 5% of the originally J=1 metastables undergo a collision with a H_2 molecule before having decayed to the ground state. Thus, in the experiments presented here the J=1 metastables do not play an important role. For industrial sources with H_2 pressures of order 1 mbar and an associated λ_F of $\approx$ 0.04 cm, the situation is opposite barely any of the J=1 metastables have decayed.

For each of the three J levels we performed a basic 2-state Landau-Zener model calculation [34]. For the coupling matrix element the generic form of the expression derived for atomic hydrogen targets [26] was used. However instead of the forefactor of 9.41 we used a forefactor of 5.48 as proposed by Kimura *et al.* [27] after optimization of Landau-Zener model calculations to their low-energy electron capture experiments on He. The J-dependent cross sectional results are summarized in figure 6.7.

To solve the set of differential equations, eq. 6.3, the Sn^{2+} population was split in its three J level populations assuming a statistical population of the J in the electron capture reaction $Sn^{3+} \rightarrow Sn^{2+*}$. In addition for the $J = 1$ level it is assumed that

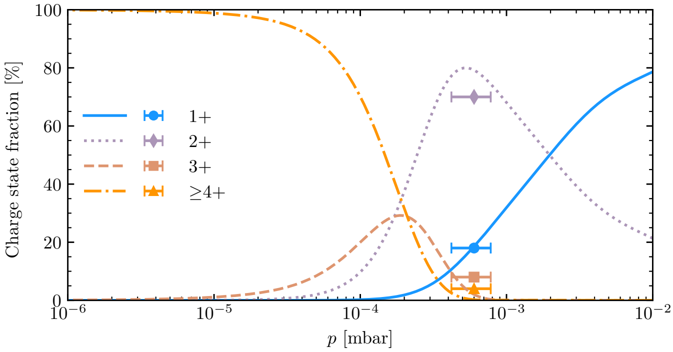

Figure 6.8: *Simulated charge state distributions of energetic* Sn^{q+} *ions detected at a distance of 68.5 cm from the LPP plasma as a function of* H_2 *buffer pressures, assuming that all* Sn^{2+} *ions are produced in the metastable 5s5p* ^3P *term with a statistical distribution over its* J *levels. For* $q \geq 4$ *the actual* q *specific fractions as measured at* $p=10^{-6}$ *mbar (see figure 6.3) were used as input in solving the set of differential equations.*

it decays to the ground state before a next charge-changing collision occurs, thus with this $J = 1$ level we associated the Sn^{2+} ground state capture cross section of 0.1×10^{-16} cm^2. For $J = 0$ and 2 the calculated cross sections depicted in figure 6.7. Figure 6.8 shows the results of the simulations which now explicitly include metastable Sn^{2+*} ions. As can be seen from the figure, the experimental data are well-reproduced by the simulations highlighting the key role of metastable Sn^{2+*} ions in the production of energetic keV Sn^{1+} ions by means of consecutive charge exchange starting from energetic highly charged Sn^{q+} ions with charge states of $q+ \geq 4+$ ejected from the laser-produced plasma into the surrounding H_2 buffer gas.

6.4 Conclusion

We have investigated the evolution of charge-state-resolved kinetic energy spectra of Sn ions ejected from a LPP of Sn as a function of the density of the H_2 buffer gas surrounding the plasma. Without H_2 being present, energetic 1 to 5 keV Sn ions in charge states of 4+ to 8+ are detected. Sn ions ion lower charge states are absent at energies above 1 keV. However, at the highest H_2 pressure of 6×10^{-4} mbar, no highly charged Sn ions are measured anymore at energies above 1 keV, only Sn^{2+} and Sn^{+} ions are observed. The low-charged energetic Sn ions are produced by a series of consecutive electron capture processes. Therefore, in particular, the presence of Sn^{+} ions is remarkable because electron capture by Sn^{2+} ions from H_2 is endothermic and thus very unlikely to happen at keV energies, which from a atomic collision perspective are very low-energies. To explain the production of keV Sn^+ ions, electron capture by metastable Sn^{2+*} ions is inferred. Previous work on Sn^{3+} - H_2 collisions [21] indicates that one-electron capture by Sn^{3+} ions populates primarily Sn^{2+} ions in metastable states. Using 2-state Landau Zener model cross sections for capture by the metastables, the key role of metastable Sn^{2+} is highlighted by model simulations using atomic collision cross sections to track the charge states of Sn ions while traversing the H_2 buffer gas.

The production of Sn^+ ions in the buffer gas is of relevance from an industrial EUV source perspective. It shifts the charge state balance away from Sn^{2+} towards Sn^+. As Sn^+ ions have a larger stopping cross section than Sn^{2+} ions [16], the production of Sn^+ ions is beneficial for the stopping of Sn ions escaping from LPP in a high charge state.

Acknowledgment

This work was carried out at the ZERNIKELEIF facility at the Zernike Institute for Advanced Materials of the University of Groningen as part of the research portfolio of the Advanced Research Center for Nanolithography (ARCNL), a public-private partnership between the University of Amsterdam (UvA), the Vrije Universiteit Amsterdam (VU), the University of Groningen (RuG - associate partner), the Netherlands Organization for Scientific Research (NWO), and the semiconductor equipment manufacturer ASML. The project is co-financed by Holland High Tech with PPS allowance for research and development in the top sector HTSM.

Bibliography

[1] G. O'Sullivan, B. Li, R. D'Arcy, P. Dunne, P. Hayden, D. Kilbane, T. McCormack, H. Ohashi, F. O'Reilly, P. Sheridan, E. Sokell, C. Suzuki, and T. Higashiguchi, J. Phys. B: At. Mol. Opt. Phys. **48**, 144025 (2015).

[2] O. O. Versolato, Plasma Sources Sci. Technol. **28**, 083001 (2019).

[3] S. Bajt, J. B. Alameda, T. W. Barbee Jr., W. M. Clift, J. A. Folta, B. Kaufmann, and E. A. Spiller, Opt. Eng. **41**, 1797 (2002).

[4] Q. Huang, V. Medvedev, R. van de Kruijs, A. Yakshin, E. Louis, and F. Bijkerk, Appl. Phys. Rev. **4**, 011104 (2017).

[5] F. Torretti, J. Sheil, R. Schupp, M. M. Basko, M. Bayraktar, R. A. Meijer, S. Witte,

W. Ubachs, R. Hoekstra, O. O. Versolato, A. J. Neukirch, and J. Colgan, Nat. Commun. **11**, 2334 (2020).

[6] D. J. Hemminga, L. Poirier, M. M. Basko, R. Hoekstra, W. Ubachs, O. O. Versolato, and J. Sheil, Plasma Sources Sci. Technol. **30**, 105006 (2021).

[7] S. Fujioka, H. Nishimura, K. Nishihara, M. Murakami, Y.-G. Kang, Q. Gu, K. Nagai, T. Norimatsu, N. Miyanaga, Y. Izawa, K. Mima, Y. Shimada, A. Sunahara, and H. Furukawa, Appl. Phys. Lett. **87**, 241503 (2005).

[8] M. Murakami, Y. Kang, K. Nishihara, S. Fujioka, and H. Nishimura, Phys. Plasmas **12**, 062706 (2005).

[9] A. Z. Giovannini, N. Gambino, B. Rollinger, and R. S. Abhari, J. Appl. Phys. **117**, 033302 (2015).

[10] M. J. Deuzeman, A. S. Stodolna, E. E. B. Leerssen, A. Antoncecchi, N. Spook, T. Kleijntjens, J. Versluis, S. Witte, K. S. E. Eikema, W. Ubachs, R. Hoekstra, and O. O. Versolato, J. Appl. Phys. **121**, 103301 (2017).

[11] A. Bayerle, M. J. Deuzeman, S. van der Heijden, D. Kurilovich, T. de Faria Pinto, A. Stodolna, S. Witte, K. S. E. Eikema, W. Ubachs, R. Hoekstra, and O. O. Versolato, Plasma Sources Sci. Technol. **27**, 045001 (2018).

[12] V. Bakshi, ed., *EUV Lithography*, 2nd Edition ed. (SPIE Press, 2018).

[13] T. E. Sharp, At. Data Nucl. Data Tables **2**, 119 (1971).

[14] G. H. Dunn, J. Chem. Phys. **44**, 2592 (1966).

[15] A. Kramida, Yu. Ralchenko, J. Reader, and and NIST ASD Team, NIST Atomic Spectra Database (ver. 5.3), [Online]. Available: `http://physics.nist.gov/asd` [2016, February 2]. National Institute of Standards and Technology, Gaithersburg, MD. (2015).

[16] D. Abramenko, M. Spiridonov, P. Krainov, V. Krivtsun, D. Astakhov, V. Medvedev, M. van Kampen, D. Smeets, and K. Koshelev, Appl. Phys. Lett. **112**, 164102 (2018).

[17] D. Kurilovich, A. L. Klein, F. Torretti, A. Lassise, R. Hoekstra, W. Ubachs, H. Gelderblom, and O. O. Versolato, Phys. Rev. Appl. **6**, 014018 (2016).

[18] L. Poirier, A. Bayerle, A. Lassise, F. Torretti, R. Schupp, L. Behnke, Y. Mostafa, W. Ubachs, O. O. Versolato, and R. Hoekstra, Appl. Phys. B **128**, 39 (2022).

[19] L. Poirier, A. Lassise, Y. Mostafa, L. Behnke, N. Braaksma, L. Assink, R. Hoekstra, and O. O. Versolato, Appl. Phys. B **128**, 135 (2022).

[20] R. Kersevan and M. Ady, in *Proc. 10th Int. Particle Accelerator Conf.* (2019).

[21] S. Rai, K. I. Bijlsma, I. Rabadán, L. Méndez, P. A. J. Wolff, M. Salverda, O. O. Versolato, and R. Hoekstra, Phys. Rev. A **106**, 012804 (2022).

[22] R. Mann, F. Folkmann, and H. F. Beyer, J. Phys. B: At. Mol. Phys. **14**, 1161 (1981).

[23] H. Ryufuku, K. Sasaki, and T. Watanabe, Phys. Rev. A **21**, 745 (1980).

[24] A. Niehaus, J. Phys. B: At. Mol. Phys. , 2925 (1986).

[25] M. Imai, Y. Iriki, and A. Itoh, Fusion. Sci. Tech. **63**, 392 (2013).

[26] R. E. Olson and A. Salop, Phys. Rev. A **14**, 579 (1976).

[27] M. Kimura, T. Iwai, Y. Kaneko, N. Kobayashi, A. Matsumoto, S. Ohtani, K. Okuno, S. Takagi, H. Tawara, and S. Tsurubuchi, J. Phys. Soc. Jpn **53**, 2224 (1984).

[28] I. I. Sobelman, *Atomic spectra and radiative transitions* (Springer-Verlag, Berlin Heidelberg New York, 1979).

[29] M. F. Gu, Can. J. Phys. **68**, 675 (2008).

[30] K. Haris and A. Tauheed, Phys. Scr. **85**, 055301 (2012).

[31] L. J. Curtis, R. Matulioniene, G. Ellis, and C. Froese Fischer, Phys. Rev. A **62**, 052513 (2000).

[32] C. Colón and A. Alonso-Medina, J. Phys. B: At. Mol. Opt. Phys. **43**, 165001 (2010).

[33] J. A. Kernahan, E. H. Pinnington, W. Ansbacher, and J. L. Bahr, Nucl. Instr. Meth. Phys. Res. B **9**, 616 (1985).

[34] R. K. Janev and H. Winter, Phys. Rep. **117**, 265 (1985).

Summary

State-of-the-art nanolithography machines use extreme ultraviolet (EUV) light to print integrated circuits on silicon wafers. The EUV light in such machines is generated by irradiating mass-limited Sn microdroplets with high power pulsed laser which generates the EUV-emitting hot and dense laser-produced plasma (LPP). However, in addition to the desired EUV light, the LPP also generates undesired products such as energetic Sn ions and other debris that fly towards the plasma-facing components and may damage the special Mo/Si multilayer optics inside the machine, especially the plasma-facing EUV collector mirror. In order to mitigate the debris, and specifically to stop the energetic ions from damaging the collector mirror, the plasma is embedded in H_2 gas. Since H_2 stops the debris without considerably absorbing the EUV light, it is chosen as the stopping gas. In the H_2 environment, the Sn ions collide with the gas molecules, leading to energy loss or stopping. An important process coupled to the ion stopping is charge exchange, where the Sn ions from the LPP capture one or more electrons from the gas molecules. This process is known to be highly resonant in the LPP ion energy range, which means that depending on the availability of the states, charge-exchange cross sections can be either significantly large or very small. However, the public literature lacks the key information about this important process taking place in the EUV source. For the purpose of developing accurate ion-stopping models, quantitative knowledge of the charge exchange process is crucial, as charge exchange also influences stopping. Furthermore, determining the appropriate concentration of H_2 gas also requires understanding of the interactions and tolerances of multilayer mirror materials such as Mo and Ru to the impact of relatively heavy Sn ions.

This thesis details research on how Sn ions interact with solid surfaces and the H_2 gas. The primary aspect investigated in ion-surface collisions is ion backscattering, while charge exchange mechanisms were explored in relation to ion-gas interaction.

In chapter 2, the scattering of Sn ions off Mo and Ru is investigated. Mo is the element of one of the layers that make up the multilayer mirrors, while Ru is regularly used as a capping layer to the multilayer mirrors. The results of the experimental studies demonstrate that multiple collision scattering, which results in a broad energy spectrum, dominates the energy distributions of scattered ions. The experimental findings are compared with the predictions of the widely used simulation package SRIM. Barring the striking, complete absence of the single-collision peak in the experimental data, these predictions are largely consistent with the experiments. The energy of the incoming Sn ions is varied from 7 to 28 keV. Additionally, time-of-flight spectroscopic measurements are taken to find the energy of neutral particles too. The strong single-collision peak observed in the simulations but absent in the experiments may be due to SRIM-related factors, such as the failure to account for pre-scattering interactions in front of the surface or the use of a fixed distance between successive collisions. It might also be due to the use of a generic potential that might not be optimal for Sn-Mo and Sn-Ru scattering.

Chapter 3 follows up on the results of Chapter 2, and in this chapter the scattering of Kr ions from a Cu sample is investigated in the keV energy range. The energy distributions of the backscattered ions show notable peaks at energies where single-collision (SC) scattering peaks are anticipated, in addition to the broad energy spectrum resulting from multiple-collision scattering. Such SC peaks are demonstrated to be absent in systems with a similar mass ratio and kinetics, Sn - Mo/Ru scattering. The current Kr-Cu results enable a comparison of experiments with those of SRIM. Although much weaker than in the SRIM simulations, the strength of the experimental SC peaks could be utilized as a benchmark to help SRIM better describe low-energy heavy particle scattering off surfaces.

The research focus is changed from ion-surface collisions to ion-gas collisions after the chapter 3. The gas target setup CHEOPS (CHarge Exchange Observed by Particle Spectroscopy) is described in chapter 4. In this setup, crossed-beam type experiments are performed to study the collision of charge, energy, and isotope-selected Sn ions with H_2.

Chapter 5 reports the experimentally measured total single electron capture cross sections in the energy range of 1 - 100 keV for Sn^{3+} colliding with H_2 and D_2. A remarkable isotope effect is observed in the measured data. The experimental results for D_2 are in good agreement with the semi-classical calculations, both of which show a slight increase in lower energies. However, the experimental data for H_2

show a much stronger increase as ion energy decreases. The cause of this discrepancy is proposed to be the vibrational effects that are neglected in the calculations and that result in the breakdown of the Franck-Condon approximation.

Chapter 6 reports the charge-state resolved kinetic energy spectra of Sn ions ejected from the LPP of Sn, at different densities of H_2 buffer gas. The experiments reported in this chapter are performed at ARCNL. Using a retarding field analyzer, energetic keV Sn ions with charge states ranging from 4+ to 8+ are measured in the absence of H_2. When the LPP is embedded in H_2, electron capture by Sn ions from H_2 results in a shift of charge state distribution towards lower charge states. At the highest experimental H_2 pressure of 6×10^{-4} mbar, only Sn^{2+} and Sn^{+} ions are measured while no appreciable kinetic energy loss or stopping is observed. The endothermic nature of the electron capture by ground state Sn^{2+} ions from H_2 renders the production Sn^{+} ions noteworthy and this production is hypothesized to be due to electron capture by metastable Sn^{2+*} ions.

To conclude, the research works reported in this thesis have added new data and insights into the collisions of Sn ions with surface and gas targets relevant to EUV nanolithography. Existing simulation codes for modeling ion stopping have been benchmarked for heavy projectiles such as Sn ions, and novel data on charge exchange in Sn -H_2 collisions, have been generated. These fundamental results, while enhancing the quantitative understanding of collisions involving Sn, have also opened up many new questions and topics that call for further investigation. For instance, it would be worthwhile to extend both the experiments and calculations of σ_{32} for Sn^{3+} + H_2 collisions (reported in Chapter 5) to even lower ion energies. This would allow for the quantification of σ_{32} and the investigation of the isotope effect observed, in the entire LPP ion energy regime. At very low energies, target polarization may lead to mass-dependent trajectory effects resulting in an increase in cross sections, commonly referred to as Langevin cross sections. It would be interesting to verify if this is the case for lower energy Sn^{3+} ions as well. In chapter 5, the theoretically calculated σ_{32} shows oscillatory behavior due to the interference between transitions in the avoided crossing at $R \approx 8.5$ a.u. and those at $R \approx 3.6$ a.u. The current measurement data can be extended (taking finer energy scans) to experimentally investigate this oscillatory behavior. In Chapter 6, it is hypothesized that the production of Sn^{+} as observed in the experiments is due to electron capture by metastable Sn^{2+*} ions. However, the available literature on the lifetimes of metastable Sn^{2+*} $(5s5p\ ^3\mathrm{P}_{0,1,2})$ is scarce. Therefore, the measurement and calculation of these lifetimes, along with the quantification of metastable fractions in the Sn^{2+} population, will be useful for extending the results of chapter 6.

Samenvatting

De nieuwste en meest geavanceerde nanolithografiemachines gebruiken extreem ultraviolet (EUV) licht om geïntegreerde schakelingen te printen op silicium schijven, zogenoemde wafers. Het EUV licht in zulke machines wordt gegenereerd door massabeperkte Sn microdruppels te bestralen met een gepulseerde laser van hoog vermogen. Een druppel verandert zodoende in een EUV-uitzendend, heet en dicht lasergeproduceerd plasma (LPP). Echter, naast het gewenste EUV licht genereert het LPP ook ongewenste producten, zoals energetische Sn-ionen en andere brokstukken, welke richting de componenten vliegen die het plasma omringen. Deze ongewenste producten kunnen mogelijk de speciale Mo/Si meerlaagse optica binnenin de machine beschadigen, vooral de EUV verzamelspiegel (de zogenoemde collector mirror) welke naar het plasma gericht is. Om de brokstukken tegen te gaan, en specifiek om de energetische ionen ervan te weerhouden om de verzamelspiegel te beschadigen, wordt het plasma omringd door H_2 gas. Omdat H_2 de brokstukken stopt zonder het EUV-licht noemenswaardig te absorberen is het gekozen als het stoppende gas. In de H_2 omgeving botsen de Sn-ionen met gasmoleculen. Dit leidt tot energieverlies, ook wel 'stopping' genoemd. Een belangrijk proces wat gekoppeld is aan stopping van ionen is ladingsuitwisseling (charge exchange), waar de Sn-ionen van het LPP één of meer elektronen van de gasmoleculen invangen. Het is bekend dat dit proces zeer resonant is in het energiebereik behorend bij het LPP, wat betekent dat afhankelijk van de beschikbaarheid van staten, de werkzame doorsnede (cross section) voor ladingsuitwisseling ofwel aanzienlijk groot ofwel erg klein is. In de openbare literatuur ontbreekt echter de vitale informatie over dit belangrijke proces dat plaatsvindt in de EUV-bron. Omdat ladingsuitwisseling ook stopping beïnvloedt, is kwantitatieve kennis van het ladingsuitwisselingsproces cruciaal voor het ontwikkelen van accurate ionenstoppingmodellen. Daarnaast vereist het bepalen van de geschikte concentratie van H_2-gas ook begrip van de interacties en toleranties van meerlaagse spiegelmaterialen, zoals Mo en Ru, die geraakt worden door relatief zware Sn-ionen. Dit proefschrift beschrijft onderzoek naar de interactie van Sn ionen met vaste oppervlakken en met het H_2 gas. Het primaire aspect wat onderzocht is in ion-oppervlaktebotsingen is ion-terugverstrooiing en in het geval van ion-gasinteracties zijn ladingsuitwisselingsmechanismen verkend. In hoofdstuk 2 wordt de verstrooiing van Sn-ionen vanaf Mo en Ru onderzocht. Mo is het element van één van de lagen welke de meerlaagse spiegel vormen, terwijl Ru regelmatig gebruikt wordt als afdeklaag van de meerlaagse spiegels. De resultaten van de experimentele studies laten zien dat meerdere-botsing-verstrooiing, wat resulteert in een breed energiespectrum, de energieverdelingen van verstrooide ionen domineert. De experimentele bevindingen worden vergeleken met de voorspellingen van het alom gebruikte simulatiepakket SRIM. Behalve de opvallende, volledige afwezigheid van de enkele-botsing-piek in de experimentele data zijn deze voorspellingen grotendeels consistent met de experimenten. De energie van de inkomende Sn-ionen is gevarieerd van 7 tot 28 keV. Daarnaast zijn spectroscopische vluchttijdsmetingen gedaan om ook de energie van neutrale deeltjes te vinden. De sterke enkele-botsing-piek welke gezien wordt in de simulaties maar niet in de experimenten zou te wijten kunnen zijn aan SRIM-gerelateerde factoren, zoals het niet in beschouwing nemen van pre-verstrooiingsinteracties voor het oppervlak of het gebruik van een bepaalde vaste afstand tussen opeenvolgende botsingen. Het zou ook te wijten kunnen zijn aan het gebruik van een generiek potentiaal welke mogelijk niet optimaal is voor Sn-Mo en Sn-Ru verstrooiing. Hoofdstuk 3 gaat door op de resultaten van hoofdstuk 2. In dit hoofdstuk wordt de verstrooiing van Kr-ionen vanaf een Cu-monster onderzocht in het keV-energiebereik. De energieverdelingen van de terugverstrooide ionen laten duidelijke pieken zien op energieën waar enkele-botsing-verstrooiingspieken (SC-piek (single-collision peak)) verwacht worden, naast het brede energiespectrum veroorzaakt door meerdere-botsing-verstrooiing. Het wordt gedemonstreerd dat dergelijke SC-pieken afwezig zijn in systemen met een vergelijkbaar massa-ratio en kinetica, in Sn – Mo/Ru verstrooiing. De huidige Kr-Cu-resultaten maken een vergelijking mogelijk van experimenten met die van SRIM. De sterkte van de experimentele SC-pieken, hoewel veel zwakker dan in de SRIM-simulaties, zou gebruikt kunnen worden als een maatstaf om SRIM te helpen om de verstrooiing van zware en laag-energetische deeltjes vanaf oppervlakken beter te beschrijven. De focus van het onderzoek is verlegd van ion-oppervlak botsingen naar ion-gas botsingen na hoofdstuk 3. In hoofdstuk 4 wordt de opstelling met gas als doelwit, CHEOPS (CHarge Exchange Observed by Particle Spectroscopy), beschreven. In deze opstelling worden experimenten uitgevoerd van het type gekruisde-bundel, om de botsingen van Sn-ionen, geselecteerd op lading, energie, en isotoop, met H_2 te bestuderen. Hoofdstuk 5 rapporteert de experimenteel gemeten totale werkzame doorsneden voor de invangst van één elektron in het energiebereik van 1 – 100 keV voor botsingen van Sn^{3+} met H_2 en D_2. Een opmerkelijk isotoopeffect wordt waargenomen in de metingen. De experimentele resultaten voor D_2 komen goed overeen met de semi-klassieke berekeningen, beide laten een lichte toename zien op lagere energieën. Echter, de experimentele gegevens voor H_2 laten een veel sterkere toename zien naarmate de energie van de ionen afneemt. Als oorzaak van deze discrepantie worden trillingseffecten voorgesteld welke verwaarloosd worden in de berekeningen en welke ervoor zorgen dat de Franck-Condon-aanname niet langer geldig is. Hoofdstuk 6 rapporteert de verdelingen van kinetische energie, gescheiden per ladingstoestand, van Sn ionen die uit het LPP gestoten worden, voor verschillende dichtheden van H_2 buffergas. De experimenten welke gerapporteerd worden in dit hoofdstuk zijn uitgevoerd op ARCNL. Sn ionen met keV-energieën en ladingstoestanden variërend van 4+ tot 8+ zijn gemeten in de afwezigheid van H_2 met behulp van een analysator die gebruik maakt van een afremmend veld, een zogenoemde retarding field analyzer. Wanneer het LPP door H_2 wordt omringd, resulteert elektroninvangst door Sn ionen vanuit H_2 in een verschuiving van de verdeling van ladingstoestand naar lagere ladingstoestanden. Bij de hoogste experimentele H_2 druk van 6×10^{-4} mbar, worden enkel Sn^{2+} en Sn^{+} ionen gemeten waarbij geen noemenswaardig verlies van kinetische energie of stopping wordt geobserveerd. De endotherme natuur van elektroninvangst door grondtoestand Sn^{2+} ionen vanuit H_2 leidt ertoe dat de productie van Sn+ ionen noemenswaardig is en er wordt verondersteld dat deze productie te wijten is aan elektroninvangst door metastabiele Sn^{2+*} ionen.

Concluderend, de onderzoekswerken in dit proefschrift hebben nieuwe gegevens en inzichten opgeleverd over de botsingen van Sn ionen met oppervlakken en gassen die relevant zijn voor EUV nanolithografie. Voor bestaande simulatiecodes voor het modelleren van ionenstopping is een maatstaf gecreëerd voor zware projectielen zoals Sn ionen en er zijn nieuwe gegevens over ladingsuitwisseling in Sn-H_2 botsingen gegenereerd. Deze fundamentele resultaten hebben het kwantitatieve begrip van botsingen van Sn versterkt en hebben ook geleid tot nieuwe vragen en onderwerpen waar meer onderzoek naar nodig is. Het zou bijvoorbeeld de moeite waard zijn om zowel de experimenten als de berekeningen van σ_{32} voor Sn^{3+} + H_2 botsingen (gerapporteerd in hoofdstuk 5) uit te breiden naar nog lagere energieën van de ionen. Dit zou het mogelijk maken om σ_{32} te kwantificeren en het geziene isotoopeffect te onderzoeken over het gehele energiebereik van het LPP. Op heel lage energieën zou polarisatie van het doelwit tot massa-afhankelijke baaneffecten kunnen leiden welke resulteren in een verhoging van de werkzame doorsnede, welke dan ook wel Langevin werkzame doorsneden worden genoemd. De in hoofdstuk 5 theoretisch berekende σ_{32} vertoont oscillerend gedrag wegens de interferentie tussen overgangen in de ontweken kruising op R $\approx$ 8.5 a.u. en die op R $\approx$ 3.6 a.u. De huidige meetgegevens kunnen uitgebreid worden (met gebruik van fijnere stappen in energie) om dit oscillerend gedrag experimenteel te onderzoeken. In hoofdstuk 6 wordt gepostuleerd dat de productie van Sn^{+} ionen, zoals gezien in de experimenten, wordt veroorzaakt door elektroninvangst door metasabiele Sn^{2+*} ionen. Echter, de beschikbare literatuur over de levensduur van metastabiele Sn^{2+*} (5s5p $^3\mathrm{P}_{0,1,2}$) ionen is schaars. Het meten en berekenen van deze levensduur, samen met de kwantificatie van de fractie metastabielen in de Sn^{2+} populatie, zal daarom nuttig zijn om de resultaten van hoofdstuk 6 uit te breiden.

Acknowledgments

I would like to take this opportunity to express my deepest gratitude to all the individuals who have supported me throughout my PhD.

First and foremost, I am deeply grateful to my supervisor, Ronnie Hoekstra, for his guidance, support, and encouragement throughout my PhD journey. His expertise and insights have been invaluable in shaping my research. I am also grateful for the guidance and regular feedback provided by my co-supervisor, Oscar Versolato.

I would also like to thank professors Stefan Schippers, Rob Timmermans and Wim Ubachs for accepting to be a part of the assessment committee.

For all the good times in and out of lab, I would like to thank my colleagues/friends at RUG - Mart Salverda, Klaas Bijlsma, Luc Assink, Alex Kleinsmit, Emiel de Wit, Xin Wang, Wen Li, Thomas Schlathölter, Yining Huo, Denisse Cruz Pérez, Mart Johan Deuzeman, Linda Balkema, Harry Jonkman and Marcelo Goulart. Also many thanks to Emiel Brinkhuis, Otte Tjepkema, Sybren Koeleman, Walewein Noordam, Wouter van Tellingen, Roeland Kamp, Pieter Wolff, Erik Berends, Ernst Lalkens, Thomas Veringa, Eva Holleman, Bas Schoonbeek and Lukas Wijma.

Special thanks to Klaas for all his time and support, and for agreeing to be my paranymph. Many thanks to Mart for all the insightful discussions and technical assistance, and to Thomas for the many quick-fix solutions in the lab. Also many thanks to Xin for all the help with formatting etc.

Many thanks to the entire ARCNL family especially my colleagues - Adam Lassise, Alex Bayerle, Bo Liu, Diko Hemminga, Dion Engels, Dmitry Kurilovich, Francesco Torretti, John Sheil, Joris Scheers, Karl Schubert, Lars Behnke, Lauren van Buuren, Lucas Poirier, Randy Meijer, Ruben Schupp, Stan de Lange, Yahia Mostafa and Zoi

Bouza. I am thankful to Joost Frenken and Marjan Fretz for their help and support. I would also like to acknowledge the assistance provided by Rutger Schoone, Rosa Andrea, Cathelijne Meijer and Romy Metz.

I am also thankful to all my collaborators especially Luis Méndez and Ismanuel Rabadán from Universidad Autónoma de Madrid for sharing their theoretical expertise.

I would also like to acknowledge the support and encouragement of all my friends from Groningen, Puttaparti and Darjeeling, who have been my support system in this journey. Special thanks to Klaas and Eline for their help with the Dutch translation. Heartfelt gratitude to Rama anna and Aarti akaa for their support during my stay in Groningen. Many thanks to Shubham for agreeing to be my paranymph. Heartfelt gratitude to Pranitha Sankar and Prof. Reji Philip from RRI, India for their assistance during the initial days of my PhD.

Many thanks to didi for taking care of everything back home and, to my entire family for their love and support.

I would like to end it by thanking you Shinji for everything. I could not have done it without you.

Subam Rai
Eindhoven
January 22, 2023